Damage Evolution in Composite Materials and Sandwich Structures Under Impulse Loading

Thesis by

Michael Lee Silva

in Partial Fulfillment of the Requirements

for the Degree of

Doctor of Philosophy

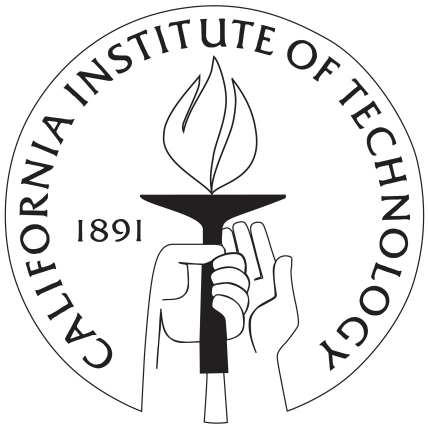

California Institute of Technology

Pasadena, California

2011

(Defended January 27, 2011)

Dedicated to my wonderful family.

Acknowledgements

I would like to acknowledge my advisor Guruswami (Ravi) Ravichandran for his continued support during my time at Caltech. I appreciate his advice, encouragement, and gentle prodding that has helped guide my studies and thesis research. I truly appreciate the trust and freedom he allowed me to work through problems while not losing sight of the bigger picture. I would also like to thank my fellow research group members for their valuable insights, comments, and spirited discussions. I am grateful for my Caltech experience as it has allowed me to mature as a scientist, husband, and father.

I must also acknowledge the support and encouragement of my family. In particular, my loving wife during our entire time at Caltech, from problem sets to thesis writing; we have helped and supported each other. I can not say in words how much richer my life has become with her by my side and if I gained nothing else during my experiences at Caltech, would still be eternally grateful.

This work was supported by the DoD MURI at the California Institute of Technology on Mechanics and Mechanisms of Impulse Loading, Damage and Failure of Marine Structures and Materials through the Office of Naval Research (Grant#N00014-06-1-0730; Dr. Y. D. S Rajapakse, Program Manager).

Abstract

Damage evolution in composite materials is a rather complex phenomenon. There are numerous failure modes in composite materials stemming from the interaction of the various constituent materials and the particular loading conditions. This thesis is concerned with investigating damage evolution in sandwich structures under repeated transient loading conditions associated with impulse loading due to hull slamming of high-speed marine craft. To fully understand the complex stress interactions, a full field technique to reveal stress or strain is required. Several full field techniques exist but are limited to materials with particular optical properties. A full field technique applicable to most materials is known as thermoelastic stress analysis (TSA) and reveals the variation in sum of principal stresses of a cyclically loaded sample by correlating the stresses to a small temperature change occurring at the loading frequency. Digital image correlation (DIC) is another noncontact full field technique that reveals the deformation field by tracking the motion of subsets of a random speckle pattern during the loading cycles.

A novel experimental technique to aid in the study of damage progression that combines TSA and DIC simultaneously utilizing a single infrared camera is presented in this thesis. A technique to reliably perform DIC with an infrared (IR) camera is developed utilizing variable emissivity paint. The thermal data can then be corrected for rigid-body motion and deformation such that each pixel represents the same material point in all frames. TSA is then performed on this corrected data, reducing motion blur and increasing accuracy. This combined method with a single infrared camera has several advantages, including a straightforward experimental setup without the need to correct for geometric effects of two spatially separate cameras. Additionally, there is no need for

external lighting in TSA as the measured electromagnetic radiation is emitted by the sample's thermal fields.

The particular stress resolution of TSA will depend on properties of the material of interest but the noise floor for the temperature variation is universal to the camera utilized. For the camera system in this thesis, the noise floor was found to be fairly frequency independent with a magnitude of 0.01 ^{o}C, giving the minimum measurable stress for 2024 aluminum alloy of 3.6 MPa and for Nylon of 0.84 MPa. The average displacement range found during a static DIC test with IR images was 0.1 pixels. The maximum displacement variation at 1 Hz was 0.018 pixels. The average variation in strain at 1 Hz was 25 microstrain comparable to traditional DIC measurements in the visible optical regime.

The combined TSA-DIC method in IR was validated with several benchmark example problems including plate structures with holes, cracks, and bimaterials. The validated technique was applied to foam-core sandwich composite beams under repeated simulated wave slamming loading. There are numerous failure modes in sandwich composite materials and the full field stress and strain from TSA and DIC, respectively, allow for improved failure analysis and prediction. Understanding damage in sandwich structures under impulse loading is a complex open area of research and the combined TSA-DIC method provides further insight into the failure process.

Table of Contents

List of Figures

List of Tables

Chapter 1: Introduction

1.1 Motivation

The development of recent Navy marine craft has seen the emergence of lightweight designs for high-speed, multi-mission seaborne structures such as the M80 Stiletto of M Ship Co. and the ONR Sea Fighter experimental littoral combat ship. With novel concepts such as hybrid hulls and catamarans for high speed and long distance missions, modern designs for ships are increasingly utilizing sandwich composites to build lighter weight craft, obtain higher speeds, and have low radar, infrared, and magnetic signatures making them stealthy. Composite super structures and foredecks have been mated to traditional steel hulls such as the French La Fayette frigate resulting in weight savings and reduced maintenance cost over steel. Some of the longest naval ships to be constructed entirely of composite materials are the 72 meter Visby class corvettes in the Royal Swedish Navy [1]. The Visby is designed as a multi-purpose vessel with the capability to perform surveillance, combat, mine laying, mine countermeasures, and anti-submarine warfare. Being constructed entirely of carbon and glass fiber laminate skins bonded to closed-cell poly vinyl chloride (PVC) foam core, the Visby's sandwich construction allows the vessel to be lightweight, have low radar and magnetic signatures, and be strong enough to handle underwater shock loads. These benefits do not come without a cost; these structures are more complex to design and manufacture and have more failure modes than a metal hull. In addition to the standard failure modes for a classic metal ship, the material structure itself can introduce failure modes such as delamination and core shear, for example.

Wave impact loads are a major concern in the structural design of a marine vessel and are reason enough for a shipmaster to reduce the ship's speed if the impacts are too large or frequent [2]. As a marine craft pierces a wave at high speed and slams on the water surface or is impacted by a wave, a characteristic pressure pulse is generated that travels along the hull (to be described in more detail in the next section). Depending on the hull type and impact angle, there can be different responses to wave/hull slamming events. When the impact angle is quite small, on the order of a few degrees, very high pressures are created and hydroelasticity becomes important [3] meaning the deformation of the structure is significant and the fluid structure interaction has a pronounced effect on peak loads and pressure pulse profile. Very large waves, often called "freak waves", are also a concern due to the extreme forces and catastrophic damage a ship could sustain. These extremely large waves have been documented to submerge the decks of large ships, causing damage to large vessels and even cleaving one in half [4]. There are a few possible causes for these extremely large waves; one possibility is caustic focusing of gravity waves [4], where caustic regions act like a lens and make these waves more likely to form. Freak waves need not be so extreme, they can simply be surprisingly large for the given sea state. These waves can be defined as having amplitude twice as large as the significant wave height [5]. It is these, more common, freak waves which have high amplitude and low frequency that can be justifiably used as a design load for a vessel.

In addition to these freak waves, high-speed marine craft are also subject to a significant number of lower amplitude hull slamming events over their operating lifetime, which raises concern for how these complex composite structures handle repeated slamming loading. These frequent wave or hull slamming events can still produce

significantly high pressure loads and may occur with a frequency on the order of a hertz as the craft impacts waves at high speed. The issue of wave slamming poses concern for any ocean-going vessel or structure subjected to wave impact. During these hull slamming and wave impact events, the structure can be subject to very high pressures and result in substantial, if not catastrophic, damage over time. High speed boats, in particular, are subject to these loads on a more frequent basis. Understanding the structural response, damage evolution, and failure modes in sandwich structures resulting from repeated slamming loads are important in estimating a vehicles' useable lifetime and can result in improved future designs.

This thesis investigates the damage evolution in sandwich structures under simulated hull slamming conditions under controlled laboratory conditions. A technique utilizing a single infrared camera to simultaneously perform thermoelastic stress analysis (TSA) and digital image correlation (DIC) is developed for cases with relatively large displacements. TSA allows for the determination of the sum of principal stresses by measuring the magnitude of thermal variations under cyclic loading under the assumption of elastic and adiabatic loading on an isotropic homogenous medium. DIC allows for the determination of deformation under loading by tracking motion of numerous subsets of a random speckle pattern. This combined method is particularly germane to hull slamming loading on sandwich composite beams due to the large deflections expected in the center span. If these deflections are not unaccounted for, a spurious TSA result is likely to be encountered.

A unique challenge for DIC in infrared (IR) requires creating an apparent thermal contrast to provide tracking information, which was overcome through the application of

lower emissivity paint speckles on a high emissivity base coat. Combining the IR-DIC results and TSA allows for deformation correction during the loading cycles such that each pixel represents the same material point during the entire thermal recording. The combined TSA-DIC method was verified with on several benchmark problems by comparing the measured sum of principal stresses to theoretical or numerical results. Plates with holes, cracks, and bimaterial interfaces were cyclically loaded and the resulting thermal variation maps were determined after motion correction. The verified method was then applied to sandwich composite beams under high cycle simulated hull slamming loading. The resulting damage modes and propagation as well as the complex stress field, were measured during the actual loading.

1.2 Hull and Wave Slamming

High impulsive loading on boat hulls during wave impact remains a major area of concern in high-speed ship design. As an approximation of the slamming event, most previous experimental and numerical studies have focused on the so-called wedge entry problem [6], where panels or wedges are dropped into water [7]. The wedge water entry problem has been studied for many years, starting with von Karman's pioneering work in 1929 and continuing through Faltinsen's work in the new millennium. Though such studies have provided insights concerning scaling laws for local slamming pressures, the mechanisms of load transfer to the structure from slamming and subsequent damage continue to be active areas for research. In most cases, the structure is considered rigid and only limited studies have explored the deformability of the structure during slamming. Due to the unpredictability of hull slamming, designing bows to handle impact loading without sacrificing the functionality of the vessel remains difficult. Since hull

slamming can lead to catastrophic damage, such as complete collapse of the bow structure or fatigue failure of the hull, the present work seeks to understand the deformation and failure of sandwich composites due to this type of impulsive loading.

1.2.1 Theoretical pressure profiles

The majority of previous investigation into slamming utilized a wedge model as an approximation for a boat hull. A schematic of a wedge entering water and the resulting wetting profile is shown in Figure 1.1. A particular slamming event occurs when a wedge enters an initially calm body of water at some velocity (V) and deadrise angle (β), the angle the wedge makes with initial free surface. The first analysis of the wedge entry problem was performed by von Karman [8] who derived an expression for pressure and force experienced by seaplane pontoons during landing. Von Karman's analysis determined the expected pressure for an assumed infinitely large rigid wedge entering an infinitely expansive calm body of water at a constant velocity and impact angle. A major improvement to von Karman's work made by Wagner [9] included the wetting of the wedge and the formation of a water jet at the spray roots on the wedge. Dobrovol'skaya [10] simplified the problem of needing to solve a complex potential for the symmetric water entry of a rigid wedge with constant entry velocity by providing a similarity solution where a nonlinear singular integral equation could be solved in an approximate fashion. Solving this integral equation presents numerical difficulties, especially at small deadrise angles. Zhao and Faltinsen [11] presented numerical results to the similarity solution for a broad range of deadrise angles from 4 to 81 degrees using a boundary element method. An approximate and robust numerical method, referred to as the

'generalized Wagner method', was presented by Zhao et al. [12] and is numerically more stable and faster than the more exact boundary element method.

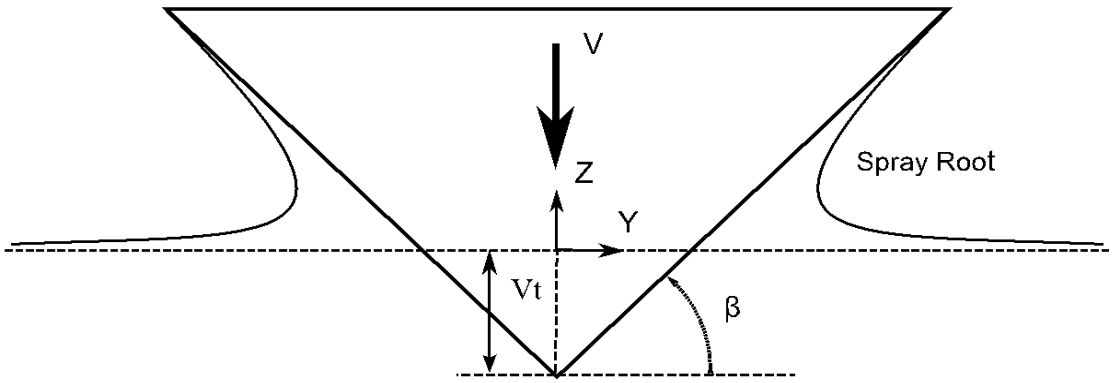

Figure 1.1: Schematic of a rigid wedge at velocity V entering initially calm water and the resulting water surface [2]. The deadrise angle is denoted by the angle β

An asymptotic solution [11] for the rigid wedge entry problem was used to generate the pressure distribution on the wedge from vertex to spray root for several deadrise angles presented in Figure 1.2. The nondimensional surface position is such that an abscissa of -1 represents the vertex and 0 represents original water level. The peak pressure occurs above this level, at the newly formed spray root. It should be noted that a significant residual pressure continues to load the panel after the peak pulse passes as long as the entry velocity is maintained. Significant peak pressures can be obtained during slamming resulting in coefficient of pressures, $(p-p_o)/(0.5\ \rho V^2)$, in the hundreds when the deadrise angle is only a few degrees [11]. The coefficient of pressure is a nondimensional measure of the pressure on the wedge surface, subtracting the free surface pressure $(p-p_o)$ and divided by the dynamic pressure $(0.5\ \rho V^2)$, where ρ is the water density and V is the velocity of the wedge. As the impact angle decreases, the peak pressure experienced by the wedge increases dramatically, and at a certain point the

assumption of a rigid wedge and attached flow become violated. Below a deadrise angle of about 5 degrees, the analytical solution is no longer valid as there are likely pockets of air trapped under the panel and hydroelastic effects become important [13], meaning the maximum stresses in a deformable panel are strongly dependent on the vibrating motion of the panel surface and interaction with the impacted water.

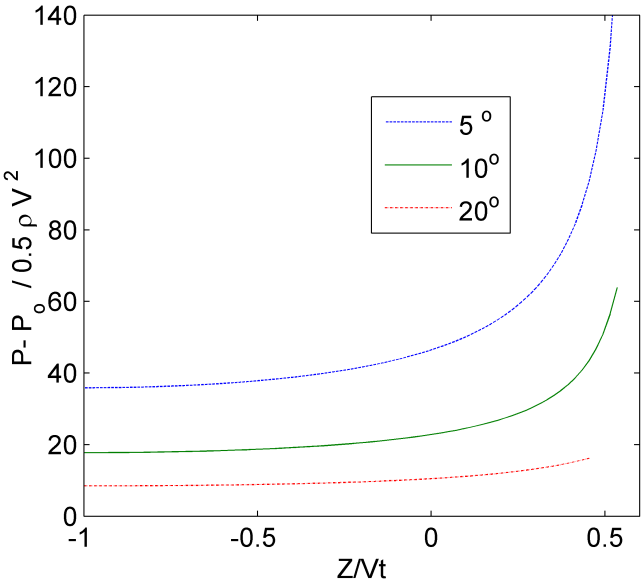

Figure 1.2: Theoretical non-dimensional pressure distributions along a rigid wedge entering water at a constant velocity, calculated from a similarity solution [11] for various wedge angles β where an abscissa -1 represents the vertex and 0 represents original water level

1.2.2 Pressure profiles from water impact experiments

There are several types of slamming on ships that are of concern: bottom, bow flare, bow stem, and wet-deck slamming [14]. In order to measure the pressure during a slam event, previous researchers [7, 15] have performed 'drop' tests with weighted flat panels or wedges into a body of water. In these tests, a weighted panel or wedge is dropped into a body of water and the resulting pressure on the panel is measured by a few embedded

pressure sensors. Wet deck slamming is usually characterized by a small slamming angle between the panel and water. Due to this small angle, the water motion is restricted and reaches very high pressures, thus increasing the effect of hydroelasticity. When hydroelasticity becomes dominant, the deformation and vibrating motion of the panel itself becomes integral to determining the true forces and strains on the panel. The impact velocity and highest natural period of the local structure also influence the effect of hydroelasticity. The peak slamming pressure occurs during the structural inertia phase, [13] with a time scale shorter than that associated with the lowest natural frequency of the impacted structure. The impact forces are balanced by the inertia of the panel, which implies structural elasticity is unimportant during this stage. After the initial impact, the motion of the plate is such that the vibration velocity completely counteracts the rigid body drop velocity. Also, the maximum strains occur after the structural inertia phase during the free vibration phase. There are additional complexities in the pressure response due to the possibility of cavitations from negative pressure and venting during the free vibration phase. Hydroelasticity needs to be considered when the angle between the body and free surface is small. For example, a 14 degree wedge shaped hull was found to have insignificant hydroelastic effects, but these effects are generally considered to be significant below 5 degrees [13]. The most important error source in the theoretical analysis is the impact velocity, which is assumed constant. Since velocity is not measured directly in experiments (only the gross craft motion); there are also non-linear hull and free-surface effects that influence the true impact velocity.

The effect of hydroelasticity causes deviations from the rigid/quasi-static slamming theory of Wagner [9]. The ratio of loading period to the first natural period has been

demonstrated by Stenius in 2009 [16] and provides a convenient measure characterizing the importance of the hydroelastic effect in the response of a panel during a slamming event. The loading period is defined as twice the wetting time, which can be approximated using Wagner theory, where the wetting time for the half width of a rigid wedge is given by,

$$c(t) = \frac{\pi V t}{2 \tan \beta} \tag{1.1}$$

where V is the velocity of the wedge, β is the slamming angle, t is time, and c is the horizontal distance from the center line to the spray root. The total length of the wedge from keel to chine is given by b and thus twice the time to wet the entire wedge length, which is the loading period (T_{LP}), is given by the following relation

$$T_{LP} = \frac{4b \sin \beta}{\pi V} \quad . \tag{1.2}$$

The first natural period (T_{NP}) can be approximated using engineering beam theory by assuming an idealized two-dimensional beam where D is the bending stiffness, m represents the structural mass, and m_a the added mass due to the water (fluid-structure) interaction. The boundary condition factor μ_{NP} equals π under simply supported conditions and 4.73 when the boundaries are clamped.

$$T_{NP} = \frac{2\pi}{{\mu_{NP}}^2} \sqrt{\frac{(m + m_a) b^3}{D}} \tag{1.3}$$

The added mass for a rigid panel impacting water at high velocity can be expressed as follows [17], where ρ_w is the density of water,

$$m_a = \frac{\pi}{4}\rho_w (b\cos\beta)^2 \quad . \tag{1.4}$$

The ratio (R) between loading period and natural period can then be given as follows while neglecting the structural mass as the added mass is substantially larger,

$$R = \frac{T_{LP}}{T_{NP}} = 4\left(\frac{\mu_{NP}}{\pi}\right)^2 \frac{\tan\beta}{V}\sqrt{\frac{D}{\pi\rho_w b^3}} \quad . \tag{1.5}$$

A large R ratio can intuitively be thought of as a having a very stiff or rigid beam such that the natural period is quite small. Conversely, a small R ratio can be thought of as having a relatively flexible beam.

Stenius [16] determined panel responses for varying R ratio conditions. He demonstrated that maximum deflections and strains remained relatively constant as the R ratio increases above 5, indicating that the panels were behaving in a rigid/quasi-static manner. Deviations began to occur when the R ratio was below 5, indicating hydroelastic and membrane effects were beginning to influence the response of the panel to water impact.

High speed water impacts of sandwich composite panels have been performed by Battley [17] using slamming tests using a specially designed servo-hydraulic slam testing system (SSTS). The SSTS setup used a hydraulic piston to perform slamming events into a water tank; similar to a drop test, but with the advantage of having some control over the specimen motion after impacting the water and improved repeatability. Characteristic pressure traces from a slamming event with the SSTS are shown in Figure 1.3 and demonstrate the traveling nature of the pressure pulse and residual pressure after the peak as the panel is continually submerged. Slamming velocities up to 10 m/s were obtained

with the SSTS. The maximum strain rate in the skin (face plate) was found to be approximately 1 to 4 per/second while the maximum shear stress rate in the foam core varied with velocity from 200 MPa/s to 4000 MPa/s. Hence it is important to account for the high strain rate properties of the materials in the sandwich structures, particularly that of the cores.

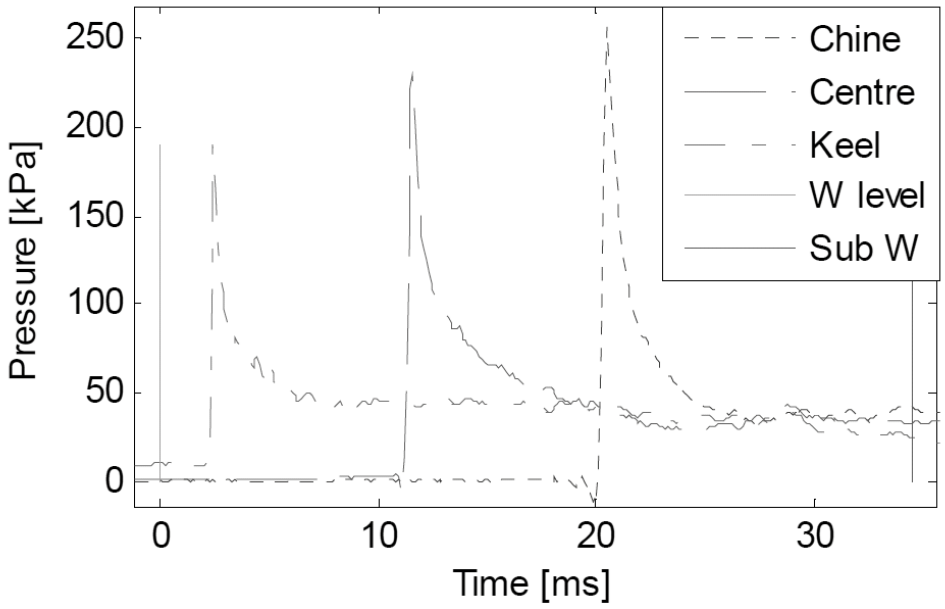

Figure 1.3: Typical pressure profiles at several panel locations during slamming event on an inclined 10^{o} rigid panel plunged into water at 3m/s, from [17]

Battley and Lake [18] describe additional work using the SSTS machine examining the differences in strain at various locations on a sandwich panels between static and dynamic loading. Under dynamic loading, the moving pressure pulse was observed to cause a large rise in strain at the chine or top edge of a panel. This corresponds to larger shear loads and deflections than experienced under static loading conditions. The current design methodologies [19] for high speed craft are based on static uniform pressure distributions and Battley's results indicate high speed craft currently may be designed with inadequate shear strength. The SSTS device has also been used to test panels of

varying stiffness under slamming loads [17]. It was found that the more flexible panels experienced lower peak pressures at the center of the panel but high pressures near the chine likely a result of local reduction in slamming angle due to panel deformation. The effects were particularly noticeable when the loading rates were comparable to the first natural frequency of the panels (R value approximately 1). Deformation due to the hydroelasticy at this low R value can result in a number of effects influencing the pressure on the panel. Panel deflection can reduce the effective slamming angle near the chine when the pressure pulse loads and deforms the panel. As the panel impacts the water and deforms, the velocity of the panel may also be decreased during portions of the slamming event due to hydroelastic effects.

1.2.3 Slamming simulations

A number of previous investigations used finite element analysis (FEA) and boundary element analysis to investigate the fluid structure interaction during slamming events and to obtain the pressure and 'hull' response for various hull designs and slamming configurations. Stenius and Rosen [19] applied FEA modeling on hull-water impacts to explicitly determine the resulting pressure profile and, through carefully chosen parameters, found it feasible to achieve non-leaking solutions (where the fluid does not inadvertently pass through the solid) that were stable, but the technique is far from trivial and can be quite numerically intensive. They found the numerical solution to be significantly dependent on the contact stiffness between the water and wedge as well as the mesh refinement. Stenius [20] investigated the effect of hydroelasticity and fluid structure interaction using FEA. A relationship between panel stiffness and loading time known as the R ratio (Eq. 1.5) was found to distinguish regions where the impact can be

assumed to be rigid/quasi-static from those where the full hydroelastic fluid structure interaction needs to be considered.

Qin and Batra [21] describe the development of a comprehensive analytical model for studying the fluid-structure interaction of a sandwich structure during impact with a calm water surface. The model was also validated using the ABAQUS finite element program and with analytical solutions. They calculated the slamming loads and response of the sandwich structure (Figure 1.4) during a shallow water impact of 5 degrees using a numerical procedure and a method for solving the coupled nonlinear governing equations. Under these slamming conditions the effect of hydroelasticity was significant and the panel deformed, leading to discrepancies in pressure when compared to that of a rigid panel. It is important to note that when the slamming angle is not this small, the effect of hydroelasticity becomes insignificant.

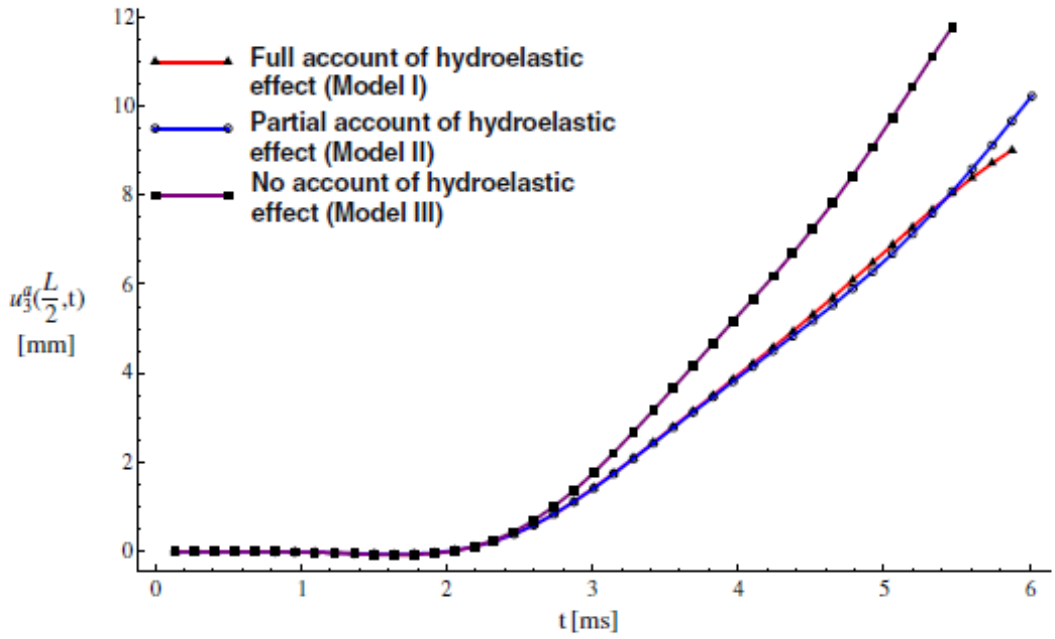

Fig. 6. Time history of the mid-span deflection during the slamming impact (V = 10 m/s).

Figure 1.4: Example of hydroelastic effect on sandwich panel deflection, from [21]. Accounting for hydroelastic effects resulted in decreased panel deflections

1.2.4 Summary

The concept of hull and wave slamming was introduced and a review of various analysis methods was explored regarding slamming pressure determination. A short history of slamming analysis from von Karman's work on seaplane floats to modern finite element analysis was presented. Several results from experimental investigations were also presented in order to compare the accuracy of the theoretical predictions. These experimental works measured the pressure and strain at several points on the panels for various impact conditions. The effect of hydroelasticity was also presented and found to be minimal when the slamming angle is greater than about 5 degrees. When the slamming angle is quite small, the hydroelastic effect can play a large role in the deflection and strains experienced by the panel. Future studies of the slamming problem can enlighten possible damage mechanisms in composite hulls undergoing repeated slamming events. With continued observation of damage initiation and progression, it is anticipated that mitigation strategies or improved design rules could be developed to produce safer, more robust structures in the next generation of lightweight, high-speed marine craft.

1.3 Composite Materials

In the most general sense, a composite material can be considered any heterogeneous medium where two or more materials are joined, forming a new structure. These structures can range from natural material combinations such as hay-reinforced mud bricks, laminated wood, and reinforced concrete to modern engineering systems such as carbon fiber epoxy composite laminates and sandwich structures [22]. The essential

benefit of composite materials is in producing a new enhanced material by combining desirable traits from the individual components. The richness of composite materials comes from the ability to tailor the properties and 'enhance' desired measure of performance including weight, strength, cost, durability, ductility, toughness, etc. A desired property can be improved in a composite material but there will usually be a trade off in another area. For example, the tensile strength of cement is improved with the addition of aggregate and steel reinforcement, but the total weight increases, thus it is not possible to improve every measure of performance.

Nature is full of examples of composite materials where evolution has combined materials to produce stronger, lighter, more durable structures such as trees, bones, teeth, and seashells. Trees have many layers or rings which combine a lighter resin-dense wood with a heaver, stronger fiber-dense wood layer [23]. This structure combines flexible and strong components allowing trees to reduce mass and grow against gravity while not snapping under normal wind loads. The human body is also full of examples of composites such as teeth and bones where the combined properties of materials produce an improved structure. Bones are made of collagen fibers and crystalline salts [24] that provide great tensile and compressive strength, respectively, very similar to reinforced concrete. Sea shells, such as nacre, are also composite materials consisting of one or more ceramic phases embedded in a polymeric matrix [25] that improves the fracture toughness by virtue of a specialized microstructure.

There is a long history of utilizing composite materials in the construction industry. From straw-reinforced mud bricks in the ancient world to the ubiquitous steel-reinforced concrete in the modern world [22]. In modern engineering, fiber- reinforced composites

have become an attractive method to produce high-performance structures due to their high strength-to-weight ratios and controlled anisotropy [26]. Fiber composites are constructed by combining high tensile strength fibers with a polymer matrix, which transfers loads to the fibers, keeps them together in the proper orientation, and protects them from environmental damage. The high specific strength of fiber-reinforced composites is due to the high strength fibers and low density matrix. The anisotropy or directional properties can be controlled in a number of ways; by adjusting the volume fractions of fiber and matrix, or by combining several layers of fiber-reinforced laminates in different orientations. The first major use of fiberglass/epoxy composites occurred during WWII when composite aircraft radar domes replaced the heavier, less electromagnetically transparent, canvas-plywood domes [27]. The first mass production of sandwich panels also occurred during WWII, with the English Mosquito aircraft utilizing veneer faces with a balsa wood core [28]. Soon after WWII, the marine industry created the first glass fiber composite boat for the U.S. Navy. Composite material use has increased steadily, growing at 6.5% since the 1960s [29] as costs have decreased and the weight savings and reduced maintenance costs have been realized.

A material's true strength is several orders of magnitude lower than ideal atomistic predictions; this is driven by the size and distribution of flaws within all real materials. Advanced fibers attain their dramatic strength increase over the bulk material due to small fiber diameters; as the cross sections decreases the probability of the presence of flaws is reduced, and thus the material is able to sustain larger stresses before failure. The long fibers combined with a matrix to transfer load between fibers allow the structure to take advantage of the high tensile properties. The most common engineering composite

fiber is made of glass, due to both the low cost and high strength [29]. The production of glass fibers begins by melting the raw ingredients such as sand, limestone, and alumina, in a furnace. The molten glass then flows either into a marble making machine for later remelting and drawing or into a fiber-drawing machine directly. The molten glass is gravity fed into a platinum bushing with many small holes. The molten glass from the orifices is gathered into fibers of the proper dimension, quenched with water spray and treated with binders to protect and lubricate the individual fibers. Several fibers are then gathered to form a fiberglass strand that is wound onto a spindle for later textile processing to woven sheets. Carbon and graphite fibers are the material of choice in high performance polymer matrix composites [29], with wide-spread use resulting from significant price reduction in the 1990s. A common method for producing carbon fiber is to stretch a precursor fiber made of PAN (polyacrylonitrile) molecules that have a carbon backbone. These stretched fibers are then carbonized in a furnace at 1500^{o}C in an inert atmosphere burning off the non-carbon elements leaving a pure carbon strand. These stretched carbon fibers are then surface treated (sizing) to improve bonding with epoxy resins and wound onto spools. Common matrix materials in polymeric fiber composites are thermosetting epoxy, giving easy processing ability (being a liquid) and good chemical resistance to the finished product, or thermoplastic polymers, which add the ability to be reformed under heat and pressure.

A number of manufacturing processes exist for fiber composite construction depending on the application and performance requirements. All the methods utilize either male and/or female molds which are first prepared with the desired surface finish, and then coated with mold release agents to prevent the part adhering to the mold. A

main process distinction is between wet and pre-impregnated (pre-preg) construction. Pre-preg construction utilizes fabric rolls where the fibers are already in an epoxy matrix and the structure is assembled of this fabric while the epoxy is tacky and gel like. In wet construction, the polymer matrix is applied, in liquid form, to the dry fibers during final construction. There are a number of variations of wet construction, from automated pultrusion to fairly labor-intensive hand layups. In pultrusion, fiber bundles or tows are pulled through an epoxy reservoir, shaped though a die, and then cured; forming unidirectional rods and beams. A relatively simple hand layup construction method uses an open mold where either chopped fiber or woven mats are placed into the mold and freshly mixed epoxy is applied in liquid form. The epoxy is worked into the dry fibers with rollers to wet all the fibers and squeeze out excess epoxy. This process yields low uniformity between parts with the quality depending on the skill of the operator.

Higher performance parts can be created with the introduction of a vacuum bag to cover the entire composite part so that uniform negative pressure can be applied to the part thus reducing voids by pulling out air and volatiles formed during the curing process. The composite laminate can be constructed of numerous layers of woven composite fiber cloth with freshly applied wet epoxy or pre-preg sheets. This method introduces additional waste and construction time as several layers of peel plies, bleeder plies, breather plies, vacuum bag, and sealant tape are included with the composite laminate. Each material serves a specific purpose within the laying up and bagging procedure, which are critical steps influencing the quality of the finished part. The first step is to apply a release coat on the mold for easy part removal. Peel plies help prevent surface contamination of the composite, bleeder plies and breather plies are porous materials

allowing air and volatiles a path to the vacuum ports as well as absorption of excess epoxy. The vacuum bag and sealant tape create an airtight surface around the lay-up that compresses the composite with atmospheric pressure when a vacuum is sustained in the bag. The part can then be cured at room temperature or in an autoclave oven with additional pressure applied to produce even higher fiber volume fractions, with additional pressure forcing out more epoxy and gas.

Another common method of composite manufacture is known as resin transfer molding (RTM) which is a wet impregnation process where resin and fiber layups are introduced separately. The dry fiber reinforcement layers are placed in a two-sided mold and epoxy resin is injected. The mold is filled with resin, forcing out air until the part is completely wetted. The air exhaust and resin injection ports are sealed and heat is applied to finish curing the part. The RTM method provides improved control over fiber orientation over a wet hand layup, resulting in improved mechanical properties. A modification of this method is known as vacuum assisted resin transfer molding (VARTM), where the resin is pulled into the part via an applied vacuum. Since vacuum is the driving force, one side of the mold can be replaced with a vacuum bag. Also, the pressure differential on the mold is much smaller so the mold itself can be less substantial. In wet lay-ups, VARTM, and pre-preg processes the composite material can be constructed of chopped strand mats of short fibers or complex structures created by stacking multiple layers of cloth like woven reinforcing fibers. Each individual layer can be considered a lamina sheet with approximately 0.25 mm thickness. These lamina can be unidirectional, where all the fibers are oriented in the same direction, or woven into a

single fabric with two or more fiber directions. A stack of lamina forms a laminate with the particular structural and material properties dependent on the orientation of each layer

In addition to solid laminates, the previous methods can also produce sandwich composites where the laminate skins (face plates) are separated by a low density core material. The main advantage in sandwich composite materials is to obtain a low-weight high-stiffness structure. The bending stiffness is the product of the elastic modulus (E) and bending moment of inertia (I). For a rectangular cross section of width b and height h, the moment of inertia about the axis parallel to the width through the mid-thickness is given by $bh^3/12$. The elastic modulus could be increased, resulting in a linear increase in stiffness. A more efficient method to increase stiffness takes advantage of the parallel axis theorem, where the centroid of the cross section is separated from the bending axis by a distance d resulting in an additional inertia term. This additional term is the product of the cross sectional area and the distance from the neutral axis squared. This is accomplished by separating strong but dense laminates from the neutral axis, which dramatically increases the moment of inertia with relatively little added mass of the foam. The bending stiffness and structure of an example sandwich structure with identical face sheets is shown in Figure 1.5 with core stiffness, E_c, and face stiffness, E_f. The drawback is that the compressive and tensile stress in the face sheets increases under bending as the distance from the neutral axis increases. Thus, provided the skin separation and attachment to core is maintained, the sandwich structure is stiffer and takes greater advantage of the high strength fibers than an equivalent solid laminate. A number of low-density core materials can be utilized, such as balsa wood, polymeric foam or polymeric or metallic honeycomb.

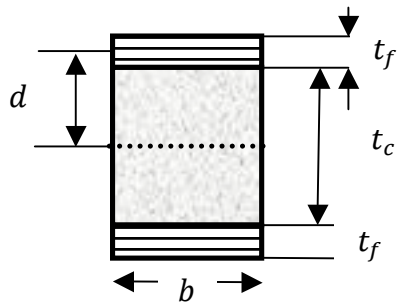

$$D = EI_{sand} = 2E_f\left(\frac{bt_f^3}{12} + \frac{t_f bd^2}{4}\right) + E_c\frac{bt_c^3}{12}$$

Figure 1.5: Schematic of sandwich structure and bending stiffness. Face sheet thickness t_f separated by distance d attached to a core of thickness t_c

Sandwich composites are found in a range of industries, including transportation, automobile, locomotive, naval, aircraft, and spacecraft. In using sandwich composites, these industries are able to reduce weight and improve various traits, such as sound transmission, fire suppression, or low magnetic signature. In locomotive applications, sandwich composite structures are able to reduce weight by 44% per seat [30] compared to the previous generation of conventional trains. There are also foams specifically designed for locomotive transportation meeting stringent fire, smoke, and toxicity requirements [31].

The aerospace industry has a relatively long experience with composite materials. Improving the performance of aircraft and spacecraft often requires mass reduction while retaining strength and stiffness, for which, sandwich composites are ideally suited. For example, the control surfaces of large passenger aircraft such as Boeing's 787 and Airbus' A380 are constructed of sandwich composites because they need to be stiff to maintain their shape under wind load but light enough to be easily moved during flight. Sandwich composites constructed of honeycomb core have been in use since the 1950s and are a major component of modern aircraft and spacecraft. The heat shield of the Apollo Crew Exploration Vehicle had to be light yet strong enough to withstand reentry

loads and, to satisfy these requirements, was constructed of graphite-epoxy honeycomb core sandwich composites. Major portions of the Space Shuttle Orbiter, such as the cargo bay doors, are also constructed of honeycomb sandwich composites [32]. Composite use in air and space vehicles is mainly driven by performance requirements. Most aerospace components are constructed with the autoclave process to obtain the highest performance parts. The additional pressure and heat in an autoclave increases the fiber volume fraction of the finished parts and reduces void content, resulting in stronger, lighter components.

In naval ships, composites have been utilized extensively to reduce weight above the waterline in bulkheads, deck houses, and helicopter hangers. Entire ship hulls are now being created from composite materials such as the Visby class Corvettes in the Royal Swedish Navy. Composite materials can also serve multifunctional roles by reducing radar, magnetic, or thermal signatures. Additionally, there are cost savings as the total life cycle cost of a composite ship is lower that an equivalent steel ship (since corrosion does not affect composite ships, reducing maintenance costs over the life of the vessel). The composites can be single skin laminates or sandwich structures, either honeycomb or foam core, with glass, carbon, or Kevlar fibers. The manufacturing techniques in boat construction include hand layup, sprayup, RTM, and VARTM [22]. When performance is not the driving factor, the composite construction can be hand layup or sprayup onto an open mold. For higher performance naval vessels, VARTM is the process of choice for large components [33] with the parts cured at room temperature. The autoclave method is not commonly utilized due to the large size of ship parts, but the fiber volume fraction with modern VARTM techniques can approach that of autoclaved parts.

1.3.1 Failure modes and damage in composites

The superior mechanical properties possible with composites over homogenous materials often justify the increased complexity in construction and design. The general structure of fiber composites consists of strong reinforcing fibers held together within a weaker matrix, with all the fibers in the same direction or woven together in multiple directions. Usually, the fibers are strong but brittle compared to the surrounding ductile matrix. Each fabric of unidirectional or woven fibers within a matrix is called a lamina. When several laminas are stacked together it is called a laminate. The directional properties of laminates can be tailored by adjusting the fiber directions in the layup sequence of the various laminas.

Numerous experimental investigations attempting to characterize failure in composite laminate structures have been performed over the years. Sun investigated failure of quasi-isotropic laminates experimentally and analytically [34]. It was found that even though the laminates were isotropic in stiffness they were quite anisotropic in strength, and that conventional failure theories were inadequate, resulting in the need for new failure criteria. Various failure modes were observed by Sun [35-37], including transverse matrix cracking and delamination through the laminate thickness, and also predicted strength and failure envelopes using Tsai-Hill failure models. Experimental failure characterizations of laminates under compression have been well investigated by Waas [38-42] where mechanisms of failure were characterized and used to illustrate the role of various micromechanical parameters. Carlsson [43-45] investigated crack propagation in laminates in both Mode I and Mode II starting with the design of test specimens and measurement of fracture toughness and delamination growth. Due to the complexity of

composite laminates, numerical investigations are quite common. One example is the work by Whitcomb [46] on delamination in compressed composite coupons using FEA and fatigue testing to obtain delamination growth data. He found that the strain energy release rate (G_c) dominates the growth process for the through thickness delamination coupons he tested. Other numerical work by Whitcomb covers buckling of a sublaminate [47] and debond growth under complex loading conditions [48].

Several models have been proposed to incorporate the experimental findings. Various internal failure modes can be predicted within a composite laminate from a micromechanics perspective. Micromechanics models are useful for predicting initial failure and in providing insight into possible underlying failure mechanics of composite materials. These models are usually limited to unidirectional composites, because adding multiple fiber orientations results in less tractable problems. Focusing on modern engineering fiber composites, a number of particular failure modes are possible including fiber breakage, microcracking in matrix, debonding of fibers from matrix, fiber pullout, and delamination of individual lamina [29]. Particular failure modes are expected under different loading conditions. Under longitudinal tensile loading along the fiber direction, failure modes include fiber breakage when the brittle fibers are stretched beyond the failure strain, fiber pullout when the matrix debonds from the fibers (initiated at a stress concentration), and shear failure along the fibers or through the matrix (often a result of multiple cracks joining). Under compressive loading along the fiber direction, the failure modes include transverse tensile fracture (when the transverse strain exceeds the strain capability of the composite), microbuckling of the long slender fibers, and shear across the fibers. When the composite is loaded in the transverse direction, which is

perpendicular to the fiber orientation, the failure modes are dominated by the weaker matrix material, as the fibers are not directly loaded. In transverse tension, the failure mode is through thickness matrix fractures which initiate at the stress concentrations along each fiber. Under transverse compression, the usual failure mode is matrix shear failure. Under in-plane shear loads, the usual failure modes are matrix shear or debonding of the fibers from the matrix. Daniel [49] developed damage evolution predictions for unidirectional composites based on experimental observation of the formation of equi-distributed microcracks in the matrix. The analytical model derivation takes advantage of the repeating structure within unidirectional composites. A unit cell of composite was envisioned and the corresponding stress field in the fiber, matrix, and interface was derived. Applying similar observations to cross ply (0/90) laminates produced analytical models for stress in the two fiber directions as a function of crack spacing. For a given applied stress, the expected crack spacing was predicted and agreed well with experimentally observed crack densities in both the 0 and 90 directions.

Predicting failure using micromechanical models in composites can be accurate at the local level in describing failure initiation at critical points. Extending these failure models in a global sense provides only approximate predictions of failure progression in lamina and laminates. Failure theories from a macromechanical point of view treat the lamina as an anisotropic homogenous medium and are often more useful in predicting failure on a larger scale. The failure behavior of a composite lamina is characterized by nine material strengths: tension and compression strength in the warp (1) and fill (2) directions ($F_{1t,}$ $F_{2t,}$ $F_{1c,}$ F_{2c}), through thickness tensile and compressive strengths ($F_{3t,}$ F_{3c}), in-plane shear strength (F_{12} or F_6), and through thickness shear strength (F_{23} or F_4 and F_{13} or F_5).

The sheer number of failure theories and lack of suitable and reliable experimental data makes it difficult to state which theory is the 'best'. In an attempt to test the various models fairly Hinton, Soden, and Kaddour [50] conducted a collaborative study over 12 years known as the 'Worldwide Failure Exercise' for composite materials where various theories were compared and validated. In the first part of this exercise, the creators or proponents of the various different theories produced failure envelopes and stress-strain curves for particular composite systems given only the basic lamina properties. This round robin effort encompassed 12 theories and 14 different loading conditions. In the second part, Hinton, Soden, and Kaddour [51] produced experimental results for the particular composite systems and biaxial loading conditions which were then used to evaluate the failure predictions from each theory.

There are a number of common failure theories proposed over the years and can generally be classified into three groups [52]. The first group is known as limit or non-interactive theories, where stresses in different directions do not influence the failure load, such as maximum stress or maximum strain. The failure criteria for the maximum stress model are constants: essentially the material strengths. The failure envelopes are composed of straight line segments, forming either rectangular or parallelogram shapes.

Table 1.1: Maximum stress and strain failure criteria

Normal stresses	Shear stresses
$\sigma_{1t} = F_{1t}; \sigma_{1c} = F_{1c}$	$\tau_{12} = F_{12} = F_6$
$\sigma_{2t} = F_{2t}; \sigma_{2c} = F_{2c}$	$\tau_{23} = F_{23} = F_4$
$\sigma_{3t} = F_{3t}; \sigma_{3c} = F_{3c}$	$\tau_{13} = F_{13} = F_5$

The second group contains interactive theories such as Tsai-Hill and Tsai-Wu which are essentially modified yielding theories from Hill's 1948 model in metal plasticity [53] accounting for material anisotropy and sign-dependent material properties [50]. A

potentially improved model for fiber composite yielding and failure by Christensen [54] is stress based and attempts to derive the governing form from basic physical postulations. Christensen's model derives expressions for fiber- and matrix-dominated failure in both Mode I and Mode II while also maintaining hydrostatic independence. The combination of the two fracture modes produces a failure envelope with sharp corners which is not captured in the Tsai-Wu model that does not make any failure mode distinction. A recent micromechanical model by Oguni and Ravichandran [55] produces failure envelopes that match quite well with Christensen's model. Oguni's model produces sharp corners in the failure envelope due to predicted changes in failure mode made possible because of the micromechanical foundation. Christensen's model does not provide information about particular failure modes but the failure envelope produces similar sharp corners because the yield functions are based on micromechanical consideration of dominant character of failure under different loading conditions. The third group contains partially interactive or mode-based failure theories such as the Hashin-Rotem or Puck theories [52]. In these types of failure theories, each failure mode has its own failure criteria and the collection of failure criteria produces a single failure envelope. The Hashin-Rotem failure criteria for various failure modes, adapted to textile composites has the following form [56] in Table 1.3.

Table 1.2: Yield functions for various interactive failure models

Tsai-Hill

$$\frac{\sigma_1^2+\sigma_2^2}{F_1^2}+\left(\frac{\sigma_3^2}{F_3}\right)^2+\frac{(\tau_4^2+\tau_5^2)}{F_4^2}+\left(\frac{\tau_6^2}{F_6^2}\right)-\frac{1}{F_1^2}(\sigma_1\sigma_2+\sigma_2\sigma_3+\sigma_3\sigma_1)=1$$

Tsai-Wu

$$f_1\sigma_1+f_2\sigma_2+f_3\sigma_3+f_{11}\sigma_1^2+f_{22}\sigma_2^2+f_{33}\sigma_3^2+f_{44}\tau_4^2+f_{55}\tau_5^2+f_{66}\tau_6^2+2f_{12}\sigma_1\sigma_2 \\ +2f_{13}\sigma_1\sigma_3+2f_{23}\sigma_2\sigma_3=1$$

Where

$f_i=\frac{1}{F_{it}}-\frac{1}{F_{ic}}$; $f_{ii}=\frac{1}{F_{it}F_{ic}}$, for i=1,2,3 (repeated index not indicating summation)

$$f_{44}=\frac{1}{F_4^2}\ ;\ f_{55}=\frac{1}{F_5^2}$$

$f_{ij}\cong\frac{1}{2}\sqrt{f_{ii}f_{jj}}$; repeated index not indicating summation

Christensen
Mode I: Matrix dominated failure

$$\alpha_1 k_1\sigma_{ii}+\left(\frac{1}{2}+\alpha_1\right)\left[\frac{-\sigma_{ii}^2}{2}+\sigma_{ij}\sigma_{ij}\right]+\sigma_{1i}\sigma_{1i}\le k_1^2 \quad i,j=2,3$$

Where $k_1=\frac{|F_{2c}|}{2}$ and $\alpha_1=\frac{1}{2}\left(\frac{|F_{2c}|}{F_{2t}}-1\right)$

Mode II: Fiber dominated failure

$$-\alpha_2 k_2\sigma_{11}+\frac{1}{4}(1+2\alpha_2)\sigma_{11}^2-\frac{(1+\alpha_2)^2}{2}\sigma_{11}\sigma\le k_2^2$$

Where $\sigma=\frac{\sigma_{22}+\sigma_{33}}{2}$ and $k_2=\frac{F_{1t}}{2}$ and $\alpha_2=\frac{1}{2}\left(\frac{F_{1t}}{|F_{1c}|}-1\right)$

Table 1.3: Hashin-Rotem mode-based failure criteria

Fiber failure modes	$\frac{\lvert\sigma_1\rvert}{F_1} = 1, \frac{\lvert\sigma_2\rvert}{F_2} = 1$
Interfiber failure mode on plane 1	$\left(\frac{\tau_5}{F_5}\right)^2 + \left(\frac{\tau_6}{F_6}\right)^2 = 1$
Interfiber failure mode on plane 2	$\left(\frac{\tau_4}{F_4}\right)^2 + \left(\frac{\tau_6}{F_6}\right)^2 = 1$
Interfiber failure mode on plane 3	$\left(\frac{\sigma_3}{F_3}\right)^2 + \left(\frac{\tau_4}{F_4}\right)^2 + \left(\frac{\tau_5}{F_5}\right)^2 = 1$

It is often difficult to assess which theory is most applicable due to the limited available experimental data. Different loading conditions, such as biaxial normal or combined normal and shear loading, alters which model best predicts the observed failure loads. For example, under transverse tensile stress the expected matrix dominated failure is best captured with limit theories such as maximum stress, while interactive theories such as Tsai-Wu underestimate the strength. Under transverse compressive stress the opposite is true [52].

1.3.2 Damage modes in sandwich structures

Sandwich composites composed of polymer fiber-epoxy skins and a low density core are subject to failure modes in addition to those for laminates, including delamination between the core and skin or core and adhesive, micro-buckling of the skin, indentation, and core shear failure. Defining failure is difficult in composite materials in general as the entire material often does not fail simultaneously, resulting in a progression of

damage. In sandwich composites, this progressive damage could reduce the stiffness to an extent that would be unacceptable in one application but not another. For example, indentation failure could be thought to occur when a load-bearing portion of the composite is damaged enough that the whole structure would be severely weakened.

Combinations of analytical and computational analyses are common in investigating sandwich composites due to the complex multi-material nature. For example, delamination in composite materials has many potential applications ranging from prediction of crack propagation at bi-material interfaces, which are important in the field of microelectronics packaging at solder junctions, and delamination of composite laminates due to crack tip singularities in anisotropic materials. Predicting delamination growth is an active area of research and one approach uses a numerical method for calculating the stress intensity factor (SIF) in composites and utilizes the SIF as a criterion for delamination growth [57]. There have also been interesting works on properties of dissimilar materials, especially relating to interface cracks. Sun [58] used various FEM methods to determine the stress intensity factor for cracks between dissimilar materials. In Sun's work, the results from the various methods (modified versions of the virtual crack extension method and crack closure integral method) were compared to analytical results [59] for jointed dissimilar semi-infinite plates with double-edge cracks. Fairly accurate mode-separated SIF were found using those methods. Shih applied elastic plastic analysis to interface and bimaterial cracks [60-62] to predict yield zone size and deformation. Analytical work by Hutchinson, Mear, and Rice [63] investigates interface cracks between dissimilar elastic half spaces and derive complex

stress intensity factors and conditions for propagation. Hutchinson and Suo [64] present an excellent review of the fracture mechanics of layered media.

The particular failure mode a sandwich composite may sustain is influenced by both the material geometry and applied loading. In compressive loading of a sandwich composite, Carlsson [65] found that various failure modes could be elicited by varying structural parameters. As the panels increased in length, the failure mode progressed from compressive failure in the face sheets to face wrinkling to global buckling. The core material in sandwich composites is usually the weakest component and can fail in several modes, some being: delaminating from the face sheets, crushing at the loading site, and core shear failure. Core shear fracture has been analytically, numerically, and experimentally investigated due to the rich nature of the failure process. The fracture process in sandwich composites under low-speed impact has been experimentally observed by Xu and Rosakis [66], and interface cracks were found to appear first and were shear dominated. Experimental work by Carlsson [67] sought to analyze an analytical model for shear debonding. Zenkert [68] demonstrated detecting core shear cracks with nondestructive testing and residual strength prediction. Impact on sandwich composites may result in core crushing damage that may act as initiation sites for other failure modes (such as delamination) and can affect the total strength of the panel [69-72].

Higher-order analytical models have been developed [73, 74] to improve failure analysis of sandwich composites under complex loadings such as blasts or with delamination within the structure. Fracture in sandwich composites is also complicated by the near-universal presence of mode mixity where the crack propagation takes place

under combined Mode I and II loading. Recent work by Berggreen [75] has analyzed delamination fracture in foam core sandwich composites accounting for mode mixity and deriving expressions for the corresponding strain energy release rates.

Fatigue crack growth in sandwich composites under flexural loading is another active area of research. Carlsson [76] describes a series of three-point bending tests with a fixture where localized indentation damage was minimal. The observed cracks were initially core-skin debonds that propagated slowly along the foam-skin interface, eventually kinking into the core as a shear crack which grew in an unstable manner. Fatigue failure in the foam core itself has been studied by Zenkert [77] who found the failure modes in closed cell polymeric foams under tension, compression, or shear were the same under fatigue as static loading and that the failure modes were loading specific. Thomsen [78] found that the presences of geometry changes and material boundaries can influence the fatigue life of sandwich composites and the structural performance can be enhanced by modifying the shape of the interface.

Modeling of sandwich composites also requires models of the foam core to accurately describe various failure modes. Brocca [79] describe a microplane model for stiff foams used in sandwich composites and utilized finite element analysis to compare three-point bending tests for failure by core indention. This model of cellular materials was able to achieve good results compared to experimental core indention observations. Experimental characterization of multi-axial yield behavior of polymer foams has also been performed by Deshpande and Fleck [80], producing failure envelopes under complex loading which could lead to better foam models.

Sandwich structures have a number of failure modes depending on loading type and structural properties. For example, using Steeves and Fleck's analysis [81] for a beam in three-point bending, the failure modes include core shear, microbuckling, indentation, and face wrinkling. Using Fleck's model for the expected damage modes (Table 1.4), one can design a sandwich structure to avoid failing in an undesirable mode. For a particular foam core and skin type, the failure map can be plotted based on skin thickness versus core thickness, non-dimensionalized using the loading span in a three-point bend test by finding the minimum failure load index.

Table 1.4: Nondimensional failure modes for sandwich composite under three-point bending [81]

Non-dimensional Parameters	$\overline{P} = \frac{P}{bL\sigma_f}; \overline{t} = \frac{t_f}{c}; \overline{c} = \frac{c}{L}; \overline{\sigma} = \frac{\sigma_c}{\sigma_f}; \overline{\tau} = \frac{\tau_c}{\sigma_f}; \overline{E} = \frac{E_f}{\sigma_f}; \overline{\rho} = \rho_c/\rho_f$
Microbuckling failure load index	$\overline{P_M} = 4\overline{t}(\overline{t}+1)\overline{c}^2$
Core Shear failure load index	$\overline{P_{cs}} = 2\overline{\tau}(\overline{\tau}+1)\overline{c}$
Indentation failure load index	$\overline{P_I} = \left(\frac{\pi^2\overline{\sigma}^2\overline{E}}{3}\right)^{1/3} \overline{t}(\overline{t}+1)^{1/3}\overline{c}^{-4/3}$

Applying Fleck's analytical model [81] to Divinycell H100 and H200 PVC foam core and carbon fiber composite face plates (CFRP), we can see the transitions from one expected failure mode to another. In Figure 1.6, the failure maps for a sandwich composite with properties from Table 1.5 using carbon fiber skin and H200 or H100 foam core were determined as a function of foam core thickness (*c*) versus face plate

thickness (t). The span was held constant and used to normalize the core thickness ($\bar{c}$), while the fiber thickness ($\bar{t}$) was normalized by the core thickness. The principal failure modes in this structure are indentation, core shear, and microbuckling. The top right area corresponds to core shear failure, the bottom area corresponds to indentation failure, and the far left strip corresponds to microbuckling. Microbuckling only occurs when the foam core is very thin compared to the span. The contours represent lines of constant load index ($\overline{P}$). There is an inverse relation in the transition between the other two failure modes. As the core gets thinner, a thicker skin is required to obtain core shear failure, otherwise an indentation failure is more likely. Comparing the H200 with the H100 failure maps we see a slight vertical shift in the indentation to core shear transition. This shift is due to the increased strength of H200 foam core, thus a thinner skin can be used and still avoid an indentation failure. The increased strength of the H200 core also enlarges the microbuckling region as the face sheets would fail first when very thin cores are utilized.

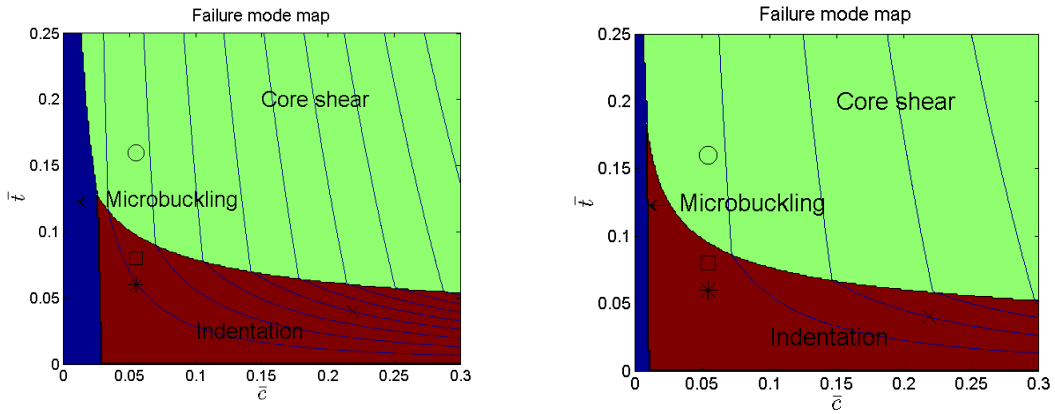

(a) (b)

Figure 1.6: Failure mode map for a sandwich structure under three-point bending loading, CFRP fiber skin and (a) H200 foam (b) H100 foam for 229 mm (9 inch) span, with the following foam and skin thickness dimensions: x (50mm/2mm), o (12.5mm/2mm), □ (12.5mm/1mm), * (12.5mm/0.75mm)

Table 1.5: Mechanical and physical properties of selected materials for sandwich structures

	Young's modulus (GPa)	Tensile strength (MPa)	Compressive strength (MPa)	Shear strength (MPa)	Density (kg/m^3)
H100	0.135[a]	3.5[a]	2.0[a]	1.60[a]	100[a]
H200	0.310[a]	7.1[a]	5.4[a]	3.5[a]	200[a]
CFRP laminate 0.66 FVF AS/H3501	138 L[b] 8.96 T[b]	1447 LU[b] 51.7 TU[b]	1447 LU[b] 206 TU[b]	93[b]	1600[b]

[a]DIAB [82], [b]Agarwal [26], L (longitudinal), T (transverse) directions

1.4 Damage Detection in Composites

Detecting damage in composites is a broad topic of interest that is needed to assess the state of the structure, its reliability, and its residual strength. There are a number of common destructive and nondestructive methods to gauge the damage extent. For example, measuring residual strength or stiffness is a simple overall measure of damage in a sample [70]. Ultrasonic testing is a common nondestructive evaluation (NDE) technique that utilizes high frequency sound waves (1-25 MHz) that are transmitted into a sample being analyzed. The sound waves interact with damage such as voids, cracks, and delaminations, resulting in reflected waves. The depth of damage can be determined using the measured time of flight and the known wave speed in the material [26]. Material properties such as elastic modulus can also be determined using ultrasonic waves by measuring the transverse and longitudinal wave velocities [83]. A common NDE technique known as acoustic emission (AE) attempts to monitor damage in real time by recording and counting the number of acoustic 'events' during loading. These acoustic events occur when some damage occurs such as a fiber breaking, and thus the rate of damage can be correlated to the rate of AE events [26]. X-ray radiography can

also be utilized as a NDE technique: damaged regions such as cracks and voids in a composite absorb less radiation as they contain less matter. The contrast between damaged areas and the composite can be enhanced with the addition of radiopaque materials (such as barium salts) into the defects, which is known as penetrant-enhanced radiography [26]. Damage can also be characterized by recording surface deformation of a sample under loading utilizing laser shearography or digital image correlation. In digital image correlation an applied speckle pattern is tracked to determine the strain field [84]. Laser shearography utilizes the speckle effect that laser illumination produces on an object. Displacement gradients can be measured by fringe pattern analysis utilizing a shearographic video laser interferometer [26]. Laser shearography is a very sensitive technique but is applicable to only small displacements, unlike digital image correlation.

1.4.1 Damage detection using thermal imaging

A rich area of NDE methods uses thermal wave analysis to detect the location and extent of local damage. A key figure in the use of thermal imaging for structural monitoring is Gerd Busse. His paper [85] describes a method of noncontact photothermal detection. This utilizes a periodically deposited energy source and the resultant thermal wave in the material is detected. The thermal wave is a highly damped scalar wave propagating at a low speed. Variations on or within the sample can affect the propagation of this wave and this forms the basis for monitoring subsurface defects using thermal imaging. Another of Busse's papers [86] describes the use of phase sensitive modulated thermography to extend the depth range of thermal imaging. Since the thermal wave is highly damped with increasing frequency, generating low frequency waves allows for deeper analysis. The changes in temperature are obtained using a high sensitivity focal

plane thermal camera employing an array of infrared detectors with a finite number of pixels. The intensity variation of the signal can be quite small but Busse showed the phase shift from pixel to pixel (which would indicate damage) can be more easily detected. He also showed that the relevant parameter is thermal diffusion length μ given by

$$\mu=\sqrt{2k/\omega} \tag{1.6}$$

where k denotes thermal diffusivity while ω is the angular frequency of modulation. The signal magnitude is affected by boundaries in a depth that is less than μ, while signal phase still responds at about twice this depth [87].

Another major application of thermal imaging utilizes the thermoelastic effect. The thermoelastic effect is the temperature variation (ΔT) due to change in the sum of the principal stresses (in a homogeneous, isotropic material) ($\sigma_x+\sigma_y$),

$$\Delta T = -\frac{\alpha T}{\rho C_p}\Delta\left(\sigma_x + \sigma_y\right), \tag{1.7}$$

where α denotes the linear thermal expansion coefficient, T is the absolute temperature, ρ the density, and C_p is the specific heat capacity at constant pressure. An excellent review of the application of thermoelastic stress analysis (TSA) is given by Dulieu-Barton [88]. Also, a review of the general theory of TSA, starting from thermodynamics, is given by Pitarresi and Patterson [89], where they derive the fundamental equations in a more general form. Lesniak [90] illustrate the use of TSA to detect stress variation on a sample by measuring the temperature variation near a crack tip and used curve fitting techniques to determine the stress intensity factor of the crack. Dulieu-Barton [91] developed a computer program FACTUS that determined stress intensity factors for various crack

angles and a novel approach for determining the non-singular stress term from the thermal signal related to thermoelasticity. The method for the non-singular term appears to work but was subject to high levels of noise. The extent of crack tip plasticity and non-adiabatic effects was observed localized near the crack tip (~3 mm) which had no influence on the stress intensity factor.

TSA has also been used to detect damage in composite structures. Paynter and Dutton [92] used a second harmonic correlation rather than just the in-phase correlation to detect damage. They showed that the second harmonic is due to local buckling due to sub-surface damage causing a localized region of tension to form when the rest of the surface was in compression. Recent work by Dulieu-Barton [93], focused on developing a correction methodology for quantitative thermoelastic stress analysis. From TSA theory, the measured temperature variation can be linearly related to the sum of the principal stresses (Eq. (1.7) within a sample and a model to correct the temperature based on the wavelength range of the detector was developed. The correction factor has to be determined experimentally due to the specific optics in use for each specific thermal camera. The applicability of this method was demonstrated on damage growth in a cyclically loaded composite laminate coupon with a hole. The method was able to remove the temperature rise due to the heat from friction in the cracked/delaminated area resulting in revealing a better stress redistribution due to damage.

The method used in this thesis combines the nondestructive measurements of thermoelastic stress analysis [88, 89, 91, 93, 94] and digital image correlation (DIC) [84, 95-99] to study damage evolution in sandwich composite structures and foam core materials.

1.4.2 Infrared measurements

A common instrument used for measuring full-field temperature is a focal plane array infrared (IR) camera. The fundamental phenomenon measured is electromagnetic radiation in the infrared spectrum. Infrared radiation is emitted by all objects with temperature above absolute zero and by measuring the amount of radiation and knowing some properties of the body in question the true temperature can be determined. The intensity of radiation energy can be determined by the Stefan-Boltzmann law, which follows as temperature to the fourth power. At a given temperature and frequency or wavelength of electromagnetic radiation, one can use Planck's law to determine the intensity of radiation. These equations are only valid for black bodies or perfect emitters. These perfect emitters are not normally encountered in nature, so a correction factor is applied, making them a gray body. This correction factor, known as emissivity, is not generally constant for all frequencies of light, but since commonly used sensors are only sensitive to a narrow range of radiation, it is common to assume the emissivity is a constant. Planck's law (1.8) describes the energy emitted by a black body at a given wavelength λ (μm) and absolute temperature T (Kelvin) per surface and per unit of solid angle (steradian) [100]. $L_{\lambda,b}$ is defined as the spectral radiance at a given wavelength with the subscript *b* indicating a blackbody assumption and utilizing constants from Table 1.6.

$$L_{\lambda,b}(\lambda,T) = \frac{2hc_o^2}{\lambda^5\,[\exp(hc/\lambda KT)-1]} = \frac{c_1}{\lambda^5\,[\exp(c_2/\lambda T)-1]}10^{-6}\ (Wm^{-2}\mu m^{-1}sr^{-1}). \tag{1.8}$$

Table 1.6: Values of physical constants [100]

Quantity	Symbol	Value	Units
Speed of light in vacuum	c_o	2.99792458 x 10^{8}	Meter $second^{-1}$
Planck constant	h	6.626076 x 10^{-34}	Joule second
Boltzmann constant	K	1.380658 x 10^{-23}	Joule $Kelvin^{-1}$
Stefan-Boltzmann constant	σ	5.67051 x 10^{-8}	Watt $meter^{-2}Kelvin^{-4}$
First radiation constant $c_1 = 2hc_o^2$	c_1	1.19104039 x 10^{-16}	Watt $meter^{2}$
Second radiation constant $c_2 = hc_0/K$	c_2	1.438769 x 10^{4}	μm Kelvin

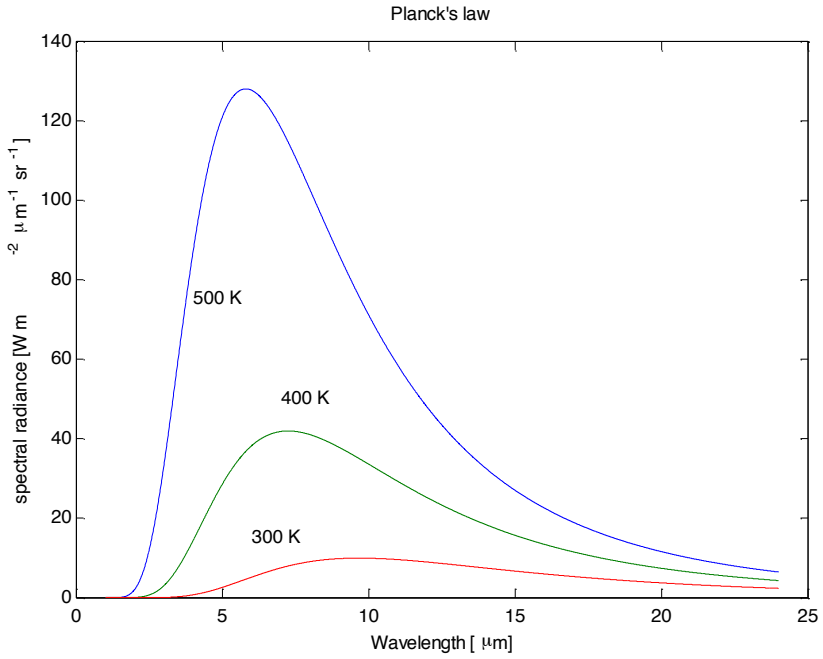

Figure 1.7: Blackbody spectral radiation according to Planck's law plotted for various temperatures

Planck's function ($L_{\lambda,b}$) is plotted for various blackbody temperatures in Figure 1.7, and one can observe a distribution of emitted radiation at various frequencies based on temperature, with the peak shifting toward lower wavelengths as temperature increases.

The IR detector (InSb) in the SC6000 FLIR camera [101] used in this thesis work is sensitive to radiation in the mid wave IR spectrum 3-5 μm. Thus, for a given temperature

of a sample a characteristic amount of radiation will be incident on the detector. This incident radiation is converted to an electric signal and is recognized as 'counts' by the camera hardware. The number of 'counts' will depend on the intensity of incident radiation and the integration time of the camera. For each integration time, a calibration should be performed to correlate counts to a number of known temperature and emissivity conditions. This calibration is also limited in the temperature range available due to the sensor electronics. For example, if not enough counts are registered it becomes difficult to distinguish between actual temperature reading and noise. If too many counts are detected in the integration time the sensor becomes saturated. Thus for a given integration time there is a detectable temperature range with this sensor.

1.5 Thesis Outline

A background on the hull and wave slamming of panels and the motivation for the research presented in the thesis as related to high-speed marine craft made of composite materials and sandwich structures is discussed in Chapter 1. This chapter also includes brief discussion of composite materials and sandwich structures, their failure modes and thermal temperature measurements. Damage detection techniques are discussed with a focus on applicability to sandwich composite materials. Chapter 2 presents fundamentals of thermoelasticity, as well as thermoelastic stress analysis (TSA) and digital image correlation (DIC) for displacement measurement, the two techniques employed for measurements of damage evolution in sandwich structures. A number of examples of the combined thermoelastic stress analysis (TSA) and digital image correlation (DIC) method are discussed. The TSA method assumes the material investigated is isotropic and homogenous. The loading is also assumed to be elastic and adiabatic, which is enforced

by cyclic loading. Chapter 3 presents the application of the combined TSA-DIC method to simulated slamming experiments on composite sandwich structures, and the resulting damage and failure modes are discussed. Conclusions for the present study and recommendations for future research are presented in Chapter 4. The appendix presents results for thermoelastic calibration and modeling of Divinycell H100 foam.

References

1. Mouritz, A.P., Gellert, E., Burchill, P., and Challis, K., *Review of advanced composite structures for naval ships and submarines.* Composite Structures, 2001. **53**(1): p. 21–41.

2. Faltinsen, O.M., *Hydrodynamics of high-speed marine vehicles*. 2005, Cambridge; New York: Cambridge University Press. xix, 454 p.

3. Faltinsen, O.M., *The effect of hydroelasticity on ship slamming.* Philosophical Transactions of the Royal Society of London Series A—Mathematical Physical and Engineering Sciences, 1997. **355**(1724): p. 575–591.

4. White, B.S. and Fornberg, B., *On the chance of freak waves at sea.* Journal of Fluid Mechanics, 1998. **355**: p. 113–138.

5. Kharif, C. and Pelinovsky, E., *Physical mechanisms of the rogue wave phenomenon.* European Journal of Mechanics B—Fluids, 2003. **22**(6): p. 603–634.

6. Faltinsen, O.M., *Water entry of a wedge with finite deadrise angle.* Journal of Ship Research, 2002. **46**(1): p. 39-51.

7. Greenhow, M. and Lin, W.M., *Non linear free surface effects: experiments and theory, Report Number 83-19*. 1983, Department of Ocean Engineering, MIT: Cambridge, MA.

8. Karman, T.V., *The impact of seaplance floats during landing* 1929, NACA, TN 321: Washington.

9. Wagner, V.H., *Phenomena associated with impact and sliding on liquid surfaces*. 1932, NACA, Transaction 1366, translated from ZAMM. 12: 193–215.

10. Dobrovol'skaya, Z.N., *On Some Problems of Similarity Flow of Fluid with a Free Surface.* Journal of Fluid Mechanics, 1969. **36**: p. 805–829.

11. Zhao, R. and Faltinsen, O., *Water Entry of 2-Dimensional Bodies.* Journal of Fluid Mechanics, 1993. **246**: p. 593–612.

12. Zhao, R. and Faltinsen, O.M. *Water entry of arbitrary two-dimensional sections with and without flow separation*. in *Symp. on Naval Hydrod.* 1997. Trondheim: National Academy Press.

13. Faltinsen, O.M., Landrini, M., and Greco, M., *Slamming in marine applications.* Journal of Engineering Mathematics, 2004. **48**(3–4): p. 187–217.

14. Faltinsen, O.M., *Hydroelastic slamming.* Journal of Marine Science and Technology, 2000. **5**(2): p. 49–65.

15. Haymen, B., Haug, T., and Valsgard, S. *Slamming drop tests on a GRP sandwich hull model*. in *ICSC2*. 1992. Florida.

16. Stenius, I., *Hydroelasticity in Marine Hull Bottom Panels — Modeling and Characterization*, in *KTH Engineering Sciences*. 2009, KTH Centre for Naval Architecture: Stockholm, Sweden.

17. Battley, M., Allen, T., Schierlink, J., Lake, S., and Pehrson, P. *Hydroelastic Behaviour of Slam Loaded Composite Hull Panels*. in *3rd High Performance Yacht Design Conference*. 2008. Auckland.

18. Battley, M. and Lake, S., *Dynamic performance of sandwich core materials.* 16th International Conference on Composite Materials, 2007.

19. Stenius, I., Rosen, A., and Kuttenkeuler, J., *Explicit FE-modeling of fluid-strucutre interaction in hull-water impacts.* International Shipbuilding Progress, 2006. **53**(2): p. 103–121.

20. Stenius, I., Rosen, A., and Kuttenkeuler, J., *Explicit FE-modelling of hydroelasticity in panel-water impacts.* International Shipbuilding Progress, 2007. **54**(2–3): p. 111–127.

21. Qin, Z. and Batra, R.C., *Local slamming impact of sandwich composite hulls.* International Journal of Solids and Structures, 2009. **46**(10): p. 2011–2035.

22. Vinson, J.R. and Sierakowski, R.L., *The behavior of structures composed of composite materials*. 2nd ed. Solid mechanics and its applications. 2002, Dordrecht; Boston: Kluwer Academic Publishers. xiv, 435 p.

23. Record, S.J., *The Mechancial Properties of Wood Including a Discussion of the Factors Affecting the Mechanical Properites , and Methods of Tiber Testing*. 1914, New York: John Wiley and Sons, Inc.

24. *Biomedical materials*. 2009, New York: Springer.

25. Laraia, V.J. and Heuer, A.H., *Novel Composite Microstructure and Mechanical Behavior of Mollusk Shell.* Journal of the American Ceramic Society, 1989. **72**(11): p. 2177–2179.

26. Agarwal, B.D., Broutman, L.J., and Chandrashekhara, K., *Analysis and performance of fiber composites*. 3rd ed. 2006, Hoboken, N.J.: John Wiley. xiv, 562 p.

27. Vinson, J.R. and Chou, T.-W., *Composite materials and their use in structures*. 1975, New York: Wiley. xii, 438 p.

28. Bishop, E., *The Mosquito: the wooden wonder*. 1990, Washington, D.C.: Smithsonian Institution Press. 170 p.

29. Agarwal, B.D. and Broutman, L.J., *Analysis and performance of fiber composites*. SPE monographs. 1980, New York: Wiley. ix, 355 p.

30. DIAB. *DIAB — Sandwich Composite Cores*. Available from: http://www.railway-technology.com/contractors/passenger/diab/.

31. DIAB. *DIvinycell P foam Low FST, Thermoplastic Core*. Available from: http://www.diabgroup.com/americas/u_products/u_divinycell_p.html.

32. Ko, W., Gong, L., and Quinn, R., *Reentry Thermal Analysis of a Generic Crew Exploration Vehicle Structure.* NASA TM-214607, 2007.

33. Crane, R., Gillespie, J., Heider, D., Yarlagadda, S., and Advani, S., *Intelligent Processing and Inspection of Naval Composites.* AMPTIAC Quarterly, 2003. **7**(3): p. 41–48.

34. Sun, C.T. and Zhou, S.G., *Failure of Quasi-Isotropic Composite Laminates with Free Edges.* Journal of Reinforced Plastics and Composites, 1988. **7**(6): p. 515–557.

35. Sun, C.T. and Kelly, S.R., *Failure in Composite Angle Structures .1. Initial Failure.* Journal of Reinforced Plastics and Composites, 1988. **7**(3): p. 220-232.

36. Sun, C.T. and Kelly, S.R., *Failure in Composite Angle Structures .2. Onset of Delamination.* Journal of Reinforced Plastics and Composites, 1988. **7**(3): p. 233–244.

37. Zhou, S.G. and Sun, C.T., *Failure Analysis of Composite Laminates with Free Edge.* Journal of Composites Technology & Research, 1990. **12**(2): p. 91–97.

38. Waas, A.M., Babcock, C.D., and Knauss, W.G., *An Experimental-Study of the Initiation and Progression of Damage in Compressively Loaded Composite Laminates in the Presence of a Circular Cutout.* AIAA/ASME/ASCE/AHS/ASC 30th Structures, Structural Dynamics and Materials Conference, Pts 1–4, 1989: p. 1000–1011.

39. Waas, A.M., Babcock, C.D., and Knauss, W.G., *Damage Progression in Compressively Loaded Laminates Containing a Circular Cutout.* Aiaa Journal, 1991. **29**(3): p. 436-443.

40. Comiez, J.M., Waas, A.M., and Shahwan, K.W., *Delamination Buckling — Experiment and Analysis.* International Journal of Solids and Structures, 1995. **32**(6–7): p. 767–782.

41. Schultheisz, C.R. and Waas, A.M., *Compressive failure of composites .1. Testing and micromechanical theories.* Progress in Aerospace Sciences, 1996. **32**(1): p. 1-42.

42. Waas, A.M. and Schultheisz, C.R., *Compressive failure of composites .2. Experimental studies.* Progress in Aerospace Sciences, 1996. **32**(1): p. 43–78.

43. Carlsson, L.A., Gillespie, J.W., and Pipes, R.B., *On the Analysis and Design of the End Notched Flexure (Enf) Specimen for Mode-II Testing.* Journal of Composite Materials, 1986. **20**(6): p. 594–604.

44. Trethewey, B.R., Gillespie, J.W., and Carlsson, L.A., *Mode-II Cyclic Delamination Growth.* Journal of Composite Materials, 1988. **22**(5): p. 459–483.

45. Ozdil, F. and Carlsson, L.A., *Mode-I Interlaminar Fracture of Interleaved Graphite Epoxy.* Journal of Composite Materials, 1992. **26**(3): p. 432–459.

46. Whitcomb, J.D., *Finite Element Analysis of Instability Related Delamination Growth.* Journal of Composite Materials, 1981. **15**(5): p. 403–426.

47. Shivakumar, K.N. and Whitcomb, J.D., *Buckling of a Sublaminate in a Quasi-Isotropic Composite Laminate.* Journal of Composite Materials, 1985. **19**(1): p. 2–18.

48. Whitcomb, J.D. and Woo, K., *Analysis of Debond Growth in Tubular Joints Subjected to Tension and Flexural Loads.* Computers & Structures, 1993. **46**(2): p. 323–329.

49. Daniel, I.M., *Experimentation and modeling of composite materials.* Experimental Mechanics, 1999. **39**(1): p. 1–19.

50. Hinton, M.J. and Soden, P.D., *Predicting failure in composite laminates: The background to the exercise.* Composites Science and Technology, 1998. **58**(7): p. 1001–1010.

51. Hinton, M.J., Kaddour, A.S., and Soden, P.D., *Evaluation of failure prediction in composite laminates: background to 'part C' of the exercise.* Composites Science and Technology, 2004. **64**(3–4): p. 321–327.

52. Daniel, I.M., *Failure of composite materials.* Strain, 2007. **43**(1): p. 4–12.

53. Hill, R., *A theory of the yielding and plastic flow of anisotropic metals.* Proceedings of the Royal Society of London. Series A—Mathematical and Physical Sciences, 1948. **193**(1033): p. 281–297.

54. Christensen, R.M., *Stress based yield/failure criteria for fiber composites.* International Journal of Solids and Structures, 1997. **34**(5): p. 529–543.

55. Oguni, K. and Ravichandran, G., *A micromechanical failure model for unidirectional fiber reinforced composites.* International Journal of Solids and Structures, 2001. **38**(40–41): p. 7215–7233.

56. Daniel, I.M. and Ishai, O., *Engineering mechanics of composite materials*. 2nd ed. 2006, New York: Oxford University Press. xviii, 411 p.

57. Chow, W.T. and Atluri, S.N., *Stress intensity factors as the fracture parameters for delamination crack growth in composite laminates.* Computational Mechanics, 1998. **21**(1): p. 1–10.

58. Ikeda, T. and Sun, C.T., *Stress intensity factor analysis for an interface crack between dissimilar isotropic materials under thermal stress.* International Journal of Fracture, 2001. **111**(3): p. 229–249.

59. Erdogan, F., *Stress Distribution in Bonded Dissimilar Materials with Cracks.* Journal of Applied Mechanics, 1965. **32**(2): p. 403.

60. Ghahremani, F. and Shih, C.F., *Corner Singularities of 3-Dimensional Planar Interface Cracks.* Journal of Applied Mechanics—Transactions of the ASME, 1992. **59**(1): p. 61–68.

61. Shih, C.F., *Elastic Plastic Analysis of a Collinear Array of Cracks on a Bimaterial Interface.* Materials Science and Engineering A—Structural Materials Properties Microstructure and Processing, 1989. **107**: p. 145–157.

62. Shih, C.F. and Asaro, R.J., *Elastic Plastic and Asymptotic Fields of Interface Cracks.* International Journal of Fracture, 1990. **42**(2): p. 101–116.

63. Hutchinson, J.W., Mear, M.E., and Rice, J.R., *Crack Paralleling an Interface between Dissimilar Materials.* Journal of Applied Mechanics—Transactions of the ASME, 1987. **54**(4): p. 828–832.

64. Hutchinson, J.W. and Suo, Z., *Mixed-Mode Cracking in Layered Materials.* Advances in Applied Mechanics, Vol 29, 1992. **29**: p. 63–191.

65. Vadakke, V. and Carlsson, L.A., *Experimental investigation of compression failure mechanisms of composite faced foam core sandwich specimens.* Journal of Sandwich Structures & Materials, 2004. **6**(4): p. 327–342.

66. Xu, L.R. and Rosakis, A.J., *Impact failure characteristics in sandwich structures Part I: Basic failure mode selection.* International Journal of Solids and Structures, 2002. **39**(16): p. 4215–4235.

67. Carlsson, L.A., Sendlein, L.S., and Merry, S.L., *Characterization of Face Sheet Core Shear Fracture of Composite Sandwich Beams.* Journal of Composite Materials, 1991. **25**(1): p. 101–116.

68. Zenkert, D. and Vikstrom, M., *Shear Cracks in Foam Core Sandwich Panels — Nondestructive Testing and Damage Assessment.* Journal of Composites Technology & Research, 1992. **14**(2): p. 95–103.

69. Shipsha, A. and Zenkert, D., *Compression-after-impact strength of sandwich panels with core crushing damage.* Applied Composite Materials, 2005. **12**(3–4): p. 149–164.

70. Zenkert, D., Shipsha, A., Bull, P., and Hayman, B., *Damage tolerance assessment of composite sandwich panels with localised damage.* Composites Science and Technology, 2005. **65**(15–16): p. 2597–2611.

71. Shipsha, A., Hallstrom, S., and Zenkert, D., *Failure mechanisms and modelling of impact damage in sandwich beams — A 2D approach: Part I — Experimental investigation.* Journal of Sandwich Structures & Materials, 2003. **5**(1): p. 7–31.

72. Shipsha, A., Hallstrom, S., and Zenkert, D., *Failure mechanisms and modelling of impact damage in sandwich beams — A 2D approach: Part II — Analysis and modelling.* Journal of Sandwich Structures & Materials, 2003. **5**(1): p. 33–51.

73. Li, R.F. and Kardomateas, G.A., *Nonlinear High-Order Core Theory for Sandwich Plates with Orthotropic Phases.* AIAA Journal, 2008. **46**(11): p. 2926–2934.

74. Li, R., Frostig, Y., and Kardomateas, G.A., *Nonlinear high-order response of imperfect sandwich beams with delaminated faces.* AIAA Journal, 2001. **39**(9): p. 1782–1787.

75. Quispitupa, A., Berggreen, C., and Carlsson, L.A., *On the analysis of a mixed mode bending sandwich specimen for debond fracture characterization.* Engineering Fracture Mechanics, 2009. **76**(4): p. 594–613.

76. Kulkarni, N., Mahfuz, H., Jeelani, S., and Carlsson, L.A., *Fatigue crack growth and life prediction of foam core sandwich composites under flexural loading.* Composite Structures, 2003. **59**(4): p. 499–505.

77. Zenkert, D. and Burman, M., *Tension, compression and shear fatigue of a closed cell polymer foam.* Composites Science and Technology, 2009. **69**(6): p. 785–792.

78. Thomsen, O.T., Bozhevolnaya, E., Lyckegaard, A., and Mortensen, F., *Characterisation and assessment of load response, failure and fatigue phenomena in sandwich structures induced by localised effects: A review.* Strain, 2008. **44**(1): p. 85–101.

79. Brocca, M., Bazant, Z.P., and Daniel, I.M., *Microplane model for stiff foams and finite element analysis of sandwich failure by core indentation.* International Journal of Solids and Structures, 2001. **38**(44–45): p. 8111–8132.

80. Deshpande, V.S. and Fleck, N.A., *Multi-axial yield behaviour of polymer foams.* Acta Materialia, 2001. **49**(10): p. 1859–1866.

81. Steeves, C.A. and Fleck, N.A., *Collapse mechanisms of sandwich beams with composite faces and a foam core, loaded in three-point bending. Part 1: analytical models and minimum weight design.* International Journal of Mechanical Sciences, 2004. **46**(4): p. 561–583.

82. DIAB. *Divinycell H Technical Data Sheet*. Available from: http://www.diabgroup.com/americas/u_literature/u_pdf_files/u_ds_pdf/H_DS_US.pdf.

83. Sierakowski, R.L. and Chaturvedi, S.K., *Dynamic loading and characterization of fiber-reinforced composites*. 1997, New York: Wiley. xiii, 252 p.

84. Bruck, H.A., Mcneill, S.R., Sutton, M.A., and Peters, W.H., *Digital Image Correlation Using Newton-Raphson Method of Partial-Differential Correction.* Experimental Mechanics, 1989. **29**(3): p. 261–267.

85. Busse, G., *Imaging with Optically Generated Thermal Waves.* IEEE Transactions on Sonics and Ultrasonics, 1985. **32**(2): p. 355–364.

86. Busse, G., Wu, D., and Karpen, W., *Thermal Wave Imaging with Phase Sensitive Modulated Thermography.* Journal of Applied Physics, 1992. **71**(8): p. 3962–3965.

87. Busse, G., *Optoacoustic Phase-Angle Measurement for Probing a Metal.* Applied Physics Letters, 1979. **35**(10): p. 759–760.

88. Dulieu-Barton, J.M. and Stanley, P., *Development and applications of thermoelastic stress analysis.* Journal of Strain Analysis for Engineering Design, 1998. **33**(2): p. 93–104.

89. Pitarresi, G. and Patterson, E.A., *A review of the general theory of thermoelastic stress analysis.* Journal of Strain Analysis for Engineering Design, 2003. **38**(5): p. 405–417.

90. Lesniak, J.R., Bazile, D. J., B.R., Zickel, M.J.,Cramer, K. E., and Welch, C. S., *Stress Intensity Measurement via Infrared Focal Plane Array*, in *Nontraditional Methods of Sensing Stress, Strain, and Damage in Materials and Structures*, D.A. Stubbs, Editor. 1996, American Society for Testing and Materials: Philadelphia.

91. Dulieu-Barton, J.M., Fulton, M.C., and Stanley, P., *The analysis of thermoelastic isopachic data from crack tip stress fields.* Fatigue & Fracture of Engineering Materials & Structures, 2000. **23**(4): p. 301–313.

92. Paynter, R.J.H. and Dutton, A.G., *The use of a second harmonic correlation to detect damage in composite structures using thermoelastic stress measurements.* Strain, 2003. **39**(2): p. 73–78.

93. Dulieu-Barton, J.M., Emery, T.R., Quinn, S., and Cunningham, P.R., *A temperature correction methodology for quantitative thermoelastic stress analysis and damage assessment.* Measurement Science & Technology, 2006. **17**(6): p. 1627–1637.

94. Dulieu-Barton, J.M. and Quinn, S., *Thermoelastic stress analysis of oblique holes in flat plates.* International Journal of Mechanical Sciences, 1999. **41**(4-5): p. 527–546.

95. Chu, T.C., Ranson, W.F., Sutton, M.A., and Peters, W.H., *Applications of Digital-Image-Correlation Techniques to Experimental Mechanics.* Experimental Mechanics, 1985. **25**(3): p. 232–244.

96. Sutton, M.A., Cheng, M.Q., Peters, W.H., Chao, Y.J., and McNeill, S.R., *Application of an Optimized Digital Correlation Method to Planar Deformation Analysis.* Image and Vision Computing, 1986. **4**(3): p. 143–150.

97. Sutton, M.A., McNeill, S.R., Jang, J.S., and Babai, M., *Effects of Subpixel Image-Restoration on Digital Correlation Error-Estimates.* Optical Engineering, 1988. **27**(10): p. 870–877.

98. Sutton, M.A. and Chao, Y.J., *Measurement of Strains in a Paper Tensile Specimen Using Computer Vision and Digital Image Correlation .1. Data Acquisition and Image-Analysis System.* Tappi Journal, 1988. **71**(3): p. 173–175.

99. Sutton, M.A., *Image correlation for shape, motion and deformation measurements: basic concepts, theory and applications*. 2009, New York: Springer.

100. Maldague, X., *Theory and practice of infrared technology for nondestructive testing*. Wiley series in microwave and optical engineering. 2001, New York;: Wiley. xix, 684 p.

101. FLIR. *SC 6000 Datasheet* Available from: http://www.flir.com/WorkArea/linkit.aspx?LinkIdentifier=id&ItemID=19966.

Chapter 2: Combined Thermoelastic Stress Analysis and Digital Image Correlation With a Single Infrared Camera

2.1 Introduction

A methodology to combine two noncontact techniques, namely thermoelastic stress analysis (TSA) and digital image correlation (DIC) is proposed. Such a combination will provide improved thermal variation results for TSA by correcting for sample motion and distortion during loading, such as that encountered in simulated hull slamming experiments. Key benefits of TSA are that it is a noncontact measurement, can work with very small strains, and no differentiation is required to obtain the stress field. With DIC, the individual components of strain can be computed based on measured displacements but there is a limiting detectable strain magnitude that must be inferred via differentiation of displacement data. Some of the other full field stress measurement methods such as photoelasticity and coherent gradient sensing (CGS) will be briefly introduced. The fundamentals of thermoelasicity and development of the TSA method will also be presented. Details of the combined TSA-DIC method will be expounded, including performance characterization. Several examples demonstrating the combined TSA-DIC method will be compared to theoretical and numerical solutions.

2.1.1 Full field stress analysis

A number of methods and sensors exist that can measure the stress or displacement of a specimen. Measuring these quantities in an average sense under uniaxial loading is

rather common and forms the basis of materials testing. Force transducers such as load cells can measure the total load in a sample and one can determine an average stress state. There are not many methods to measure the stress directly; the most common approach is to determine the strain and infer the stress via an assumed constitutive law. The total displacement of a sample can be measured with an LVDT, which can provide an average strain value. Improved displacements can be measured using clip-on displacement gauges or similar devices that measure the displacement over a small portion of the sample. Though surface-mounted strain gauges can be thought of as a point measurement, they still are actually averaging the strain over their gauge length. These methods all give a single scalar measurement for the strain state. Other methods exist that will give a measure of the full field deformation. For example, a precise grid can be deposited or marked on a surface before deformation and the distortion can be determined during loading. One can get a rough full field displacement map by comparing the distances between several points on a sample. Expanding on this idea of tracking a random pattern of particles is the basis for digital image correlation (DIC). In DIC, a subset of a random pattern is tracked (instead of a single spot) via a correlation algorithm [96] and the displacement in the deformed image is computed. With advances in computational power and introduction of digital cameras, one can track numerous subsets to subpixel accuracy rather efficiently. Each subset then represents a scalar value in the full field displacement map. By differentiating this displacement map, the strain field can be determined similar to having an almost infinite number of strain gauges in all orientations.

In order to get a more precise picture of the stress state in a complicated body, full field measurements need to be employed. Several optical methods exist to provide a full

field measure of a material's in-plane stress state. These optical methods usually provide a linear combination of the stress or strain components. Photoelasticity, for example, provides the difference in the principal stresses and the principal directions [102, 103]. The basis of the photoelastic method is the existence of stress-induced birefringence, a property only found in certain materials. Another method, known as coherent gradient sensing (CGS) [104, 105], provides a spatial derivative of the sum of the principal stresses when used in transmission and the gradient of out-of-plane displacement when used in reflection. In transmission, CGS is based on stress-induced changes to the refractive index, thus the applicable materials are limited to transparent materials with a sufficiently high stress-optic constant. In reflection CGS, any smooth surface is applicable and the surface deformations provide the necessary distortion to the light rays. Both photoelasticity and CGS require carefully aligning optics, light source, and gratings, and determining the stress state can require fairly tedious fringe pattern analysis. A third method, and focus of the present work, known as thermoelastic stress analysis (TSA) provides the sum of principal stresses but with much simpler setup than either photoelasticity or CGS methods. The physical basis for TSA is the thermoelastic effect which is present in all materials. The important material properties for TSA are specific heat capacity, density, and thermal expansion. Though all materials have a thermoelastic effect; some materials have higher sensitivities and would be easier to measure experimentally.

2.1.2 Thermoelasticity

The thermoelastic stress analysis method is based on a remarkable physical property that a small temperature change accompanies an elastic deformation due to the required

volume change. The first scientific writing documenting the presence of a thermoelastic effect was noted in natural rubber by Gough in 1805 [106]. The thermoelastic effect in metals was first discovered by Weber in 1830 [107] while investigating vibrating metal wires. A theoretical basis was first formulated by Lord Kelvin in the 1850s [108-110] giving rational explanations for the observed stress-based temperature change. Kelvin developed an expression for the exact temperature change a material would experience when subject to an infinitesimal volume change. Thus, the physical foundation for TSA was laid; the derivation of which is shown in the subsequent section.

The coupling between deformation and temperature is essentially a consequence of the laws of thermodynamics. In order to maintain an energy balance, the temperature of an elastically deformed specimen must change if the volume of the specimen changes without the addition or removal of heat. With the advent of sensitive infrared (IR) cameras and detectors, the technique of thermoelastic stress analysis could exploit the thermoelastic property to quantitatively measure the small temperature change caused by elastic deformation. This small variation in temperature resulting from an applied elastic loading forms the basis for the thermoelastic stress analysis method.

2.1.3 Thermoelastic stress analysis (TSA)

The TSA method is a relatively new technique that has the capability to provide a full field noncontact stress measurement. The fundamental TSA relationship was first proposed by Biot [111] in 1956, building on the theoretical basis laid by Kelvin a hundred years earlier. Based on previous analysis (Biot [111], Patterson [89]) the fundamental thermoelastic relation can be derived from first principles, which will be presented here for completeness. A state function for internal energy and the differential

form for the internal energy u, which is a function of strain (ε_{ij}) and temperature (T) is defined as,

$$u = u(\varepsilon_{ij}, T), \tag{2.1}$$

$$du = \left(\frac{\partial u}{\partial \varepsilon_{ij}}\right)_T d\varepsilon_{ij} + \left(\frac{\partial u}{\partial T}\right)_{\varepsilon_{ij}} dT. \tag{2.2}$$

Utilizing the 1st and 2nd laws of thermodynamics, the change in internal energy is written as a result of heat added q and work done on the system w. The differential change in entropy ds is defined as the differential heat added δq divided by the absolute temperature T.

$$du = \delta w + \delta q \tag{2.3}$$

$$ds = \frac{\delta q}{T} \geq \frac{(\delta q)_{reversible}}{T} \tag{2.4}$$

One can rewrite the work component by assuming the deformations are quasi-static and the deformations are small in general. Then, by the principle of virtual work, the work done by external forces is equal to the strain energy gained by the material,

$$\delta w = \delta w_v v = \frac{\sigma_{ij} d\varepsilon_{ij}}{\rho}, \tag{2.5}$$

where σ_{ij} is the stress tensor and ρ is the density of the material.

At this point, it is necessary to introduce another state variable known as the Helmholtz free energy. The Helmholtz thermodynamic potential H per unit mass and its derivative can be written as follows,

$$H = u - Ts, \tag{2.6}$$

$$dH = du - Tds - s\,dT. \tag{2.7}$$

Now, combining the 1st and 2nd laws and the new definition for the work done on the system, the incremental internal energy can be expressed as,

$$du = \delta q + \delta w = Tds + \frac{\sigma_{ij} d\varepsilon_{ij}}{\rho}. \tag{2.8}$$

This relation is then combined with the differential form for Helmholtz free energy (2.7), which simplifies to

$$dH = \frac{\sigma_{ij} d\varepsilon_{ij}}{\rho} - s\,dT. \tag{2.9}$$

Since *H* is a function of strain and temperature and an exact differential, one can write it in the following form, which can be compared to the previous relation,

$$dH = \left(\frac{\partial H}{\partial \varepsilon_{ij}}\right)_T d\varepsilon_{ij} + \left(\frac{\partial H}{\partial T}\right)_{\varepsilon_{ij}} dT. \tag{2.10}$$

Comparing (2.9) and (2.10), the following relations between stress and strain tensors and between entropy and temperature can be written,

$$\sigma_{ij} = \rho \left(\frac{\partial H}{\partial \varepsilon_{ij}}\right)_T, \tag{2.11}$$

$$s = -\left(\frac{\partial H}{\partial T}\right). \tag{2.12}$$

The entropy, per unit mass, is taken as a state function of strain and temperature to obtain the following relation,

$$ds = \left(\frac{\partial s}{\partial \varepsilon_{ij}}\right)_T d\varepsilon_{ij} + \left(\frac{\partial s}{\partial T}\right)_{\varepsilon_{ij}} dT. \tag{2.13}$$

Combining this form for the exact differential of entropy with the previous relation for entropy (2.12) produces the following relation,

$$ds = -\left(\frac{\partial^2 H}{\partial \varepsilon_{ij} \partial T}\right) d\varepsilon_{ij} - \left(\frac{\partial^2 H}{\partial T^2}\right)_{\varepsilon_{ij}} dT. \tag{2.14}$$

In order to remove the dependence on H in (2.14), the definition for specific heat at constant volume (c_ε) has to be introduced. Combining the 2nd law (2.4) and the previous relation for entropy, (2.12), the following relation is obtained,

$$c_\varepsilon = \left(\frac{\delta q}{dT}\right)_{\varepsilon_{ij}} = \left(\frac{T ds}{dT}\right)_{\varepsilon_{ij}} = T\left(\frac{ds}{dT}\right)_{\varepsilon_{ij}} = -T\left(\frac{\partial^2 H}{\partial T^2}\right)_{\varepsilon_{ij}}. \tag{2.15}$$

The above relation for specific heat and (2.11) are combined to completely remove the dependence on H from the exact entropy differential (2.14),

$$ds = -\frac{1}{\rho}\left(\frac{\partial \sigma_{ij}}{\partial T}\right) d\varepsilon_{ij} + c_\varepsilon \frac{dT}{T}. \tag{2.16}$$

At this point, a constitutive model has to be introduced to proceed any further. In order to determine the partial derivative of stress and temperature in (2.16), the most general stress-strain-temperature relation for linearly thermoelastic solids, also known as the Duhamel-Neumann relation, is utilized.

$$\sigma_{ij} = C_{ijkl}\varepsilon_{kl} - \beta_{ij}(T - T_0) - \varphi_{ij}(M - M_0)$$
$$with \qquad i, j, k, l = 1,2,3 \tag{2.17}$$

where C_{ijkl} is the fourth-order elastic isothermal stiffness (modulus) tensor, β_{ij} is the second-order thermal expansion tensor, φ_{ij} is the hygroscopic strain tensor, T_0 is the reference temperature, and M_0 is the reference humidity. For simplicity, the following form, which ignores the hygroscopic term, is employed,

$$\sigma_{ij} = C_{ijkl}(\varepsilon_{kl} - \alpha_{kl}\Delta T) \quad where \quad \beta_{ij} = C_{ijkl}\alpha_{kl}\,. \tag{2.18}$$

For the special case of a homogenous isotropic material, the previous relation (2.18) can be rewritten in the following form,

$$\sigma_{ij} = 2\mu\varepsilon_{ij} + (\lambda\varepsilon_{kk} - \gamma\Delta T)\delta_{ij} \quad where \quad \gamma = (3\lambda + 2\mu)\alpha\,. \tag{2.19}$$

In this well known relation, μ and λ are the Lamé constants and α is the linear thermal expansion coefficient. We can now determine the partial differential of the stress tensor with respect to temperature,

$$\frac{\partial\sigma_{ij}}{\partial T} = -\gamma\delta_{ij}. \tag{2.20}$$

Equation (2.20) is combined with the entropy relation (2.16), to obtain (2.21).

$$ds = c_\varepsilon\frac{dT}{T} + \frac{\gamma}{\rho}\delta_{ij}\varepsilon_{ij} = c_\varepsilon\frac{dT}{T} + \frac{\gamma}{\rho}\varepsilon_{kk} \tag{2.21}$$

This relationship is integrated, setting $s = 0$ and $T = T_0$ as initial conditions to obtain the following,

$$s = c_\varepsilon\log\left(\frac{T}{T_0}\right) + \frac{\gamma}{\rho}\varepsilon_{kk}\,. \tag{2.22}$$

Assuming the temperature change is very small compared to the reference temperature, only the linear term in the infinite logarithmic power series is considered,

$$s = c_\varepsilon \log\left(1 + \frac{\Delta T}{T_0}\right) + \frac{\gamma}{\rho}\varepsilon_{kk} = c_\varepsilon \frac{\Delta T}{T_0} + \frac{\gamma}{\rho}\varepsilon_{kk} \,. \tag{2.23}$$

The last major assumption is that the process is adiabatic and thus set $s = 0$ in (2.23) leading to one form of the thermoelastic relationship,

$$c_\varepsilon \frac{\Delta T}{T_0} = -\frac{\gamma}{\rho}\Delta\varepsilon_{kk} \,. \tag{2.24}$$

One of the issues in applying the previous relationship is that the specific heat at constant volume is not a commonly determined property. This relationship is made more useful by replacing the volumetric strain with a form involving hydrostatic pressure. This is accomplished by manipulating (2.19) and the stress-strain-temperature relation for isotropic materials as shown below is obtained,

$$\begin{gathered}
\sigma_{ij} = 2\mu\varepsilon_{ij} + (\lambda\varepsilon_{kk} - \gamma\Delta T)\delta_{ij} \;, \\
\sigma_{ij}\delta_{ij} = 2\mu\varepsilon_{ij}\delta_{ij} + (\lambda\varepsilon_{kk} - \gamma\Delta T)\delta_{ij}\delta_{ij} \;, \\
\sigma_{kk} = 2\mu\varepsilon_{kk} + (\lambda\varepsilon_{kk} - \gamma\Delta T)\, 3 \,, \\
\varepsilon_{kk} = \frac{\sigma_{kk} + 3\gamma\Delta T}{2\mu + 3\lambda} = \frac{\alpha}{\gamma}\,(\sigma_{kk} + 3\gamma\Delta T) \,.
\end{gathered} \tag{2.25}$$

By substituting the above relation for the volumetric strain term into the previous thermoelastic relation (2.24),

$$\begin{gathered}
\Delta\sigma_{kk} = -\Delta T\left(\frac{\rho c_\varepsilon}{\alpha T_0} + 3\gamma\right), \\
\gamma = \frac{E\alpha}{1 - 2\nu} \,.
\end{gathered} \tag{2.26}$$

Rearranging terms, the following relation is obtained, and one can notice the bracketed term is the definition of specific heat at constant pressure (c_p), which is a very commonly reported material property,

$$\Delta\sigma_{kk} = -\Delta T \frac{\rho}{\alpha T_0}\left[c_\varepsilon + \frac{3E\alpha^2 T_0}{\rho(1-2\nu)}\right]. \tag{2.27}$$

Thus, the commonly used form of the TSA relationship is derived from fundamental thermodynamics and is valid for homogeneous isotropic materials undergoing elastic and adiabatic transformations,

$$\Delta\sigma_{kk} = -\Delta T \frac{\rho}{\alpha T_0} c_p\,, \tag{2.28}$$

$$\Delta\sigma_{\beta\beta} = -\Delta T \frac{\rho}{\alpha T_0} c_p \quad where\ \beta = 1{,}2. \tag{2.29}$$

The basic TSA equation (2.28) predicts a linear relationship between temperature variation and the variation of the sum of principal stresses with the assumption that the material properties are constant. Additional assumptions in the derivation are that an isotropic, homogenous material undergoes elastic and adiabatic deformations [89]. Under plane stress loading conditions, there are stress terms only in the in-plane directions (1, 2). This modifies the basic TSA equation, as the sum of the in-plane principal stresses is then linearly related to the temperature variation (2.29), which is the form of the TSA relationship used in the present work. The adiabatic assumption is enforced by cyclically loading the sample at a sufficiently high rate. By utilizing the thermoelastic effect and the basic TSA relationship, one can correlate a measured temperature change at a location on the sample to the stress variation at that location. In order to apply the thermoelastic stress analysis method, a thermal signal must be measured and converted to a temperature

field usually by sensor calibration. Since TSA requires a cyclic loading, the thermal signal needs to be measured at a rate at least twice the loading frequency in order to satisfy the Nyquist sampling theorem and accurately determine the amplitude of thermal variation.

2.1.4 Thermography fundamentals

Thermoelastic stress analysis utilizes temperature changes on a material surface. All objects above absolute zero (0 K) emit electromagnetic radiation; the intensity of which is frequency and temperature dependent following Planck's law. In order to utilize this radiation as a measurement for temperature, Planck's law (1.8) is integrated with respect to frequency producing the Stefan-Boltzmann law (1.9), which states the total energy emitted is proportional to the fourth power of absolute temperature. At a given temperature, a unique value for the emitted radiation is obtained and by distinguishing varying levels of radiation intensity, it is possible to determine the temperature without physically contacting the body. In practice, a particular sensor and lens combination is calibrated rather than relying on these theoretical expressions. The calibration involves fitting measured intensities to known temperatures and then fitting a function. A commonly used form of calibration function for converting measured signal '*U*' in volts to temperature '*T*' in Kelvin is given below. Where *R*, *B*, and *F* are the fitting parameters

$$T(U) = \frac{B}{\ln\left(\frac{R}{U} + F\right)} \quad . \tag{2.30}$$

A trend in Planck's law shows the emitted radiation intensity peaks at a wavelength that decreases with increasing temperature; also known as Wien's displacement law. Though radiation is theoretically emitted at all wavelengths, the majority of radiation is

concentrated around this peak wavelength. Each type of infrared sensor technology is sensitive to only a portion of the infrared (IR) spectrum. The spectrum is usually divided, arbitrarily, into several regions covering the operating wavelengths for each sensor type. A common subdivision scheme is Near (0.75–1.4 μm), Short (1.4–3 μm), Mid (3–8 μm), Long (8–15 μm), and Far (15–1000 μm) IR regions. The IR region extends from Near IR, which is just beyond visible light, often used in fiber optic telecommunications and night vision systems, to Far IR, which ends at microwave radiation and has applications in producing terahertz radiation. The band most suitable for a particular application would have the peak wavelength for that temperature in the spectral range of the sensor.

In order to determine the temperature accurately with a thermographic imaging system, typically an array infrared camera, the emissivity of the surface must be known. As two bodies at the same temperature will emit different amounts of radiation if their emissivities are different. To explain emissivity further, for some given incident radiation on a surface, the energy can be reflected, absorbed, or transmitted in varying ratios. In an opaque body, no energy is transmitted, so the reflected and absorbed energy ratios have to be inversely related. For example, a highly reflective material has a low absorptance. The emissivity of a body is equal to its absorptance by Kirchhoff's law [100] which can be demonstrated if one considers a small body in equilibrium within a large opaque box that can be considered a blackbody. Since the small body is in equilibrium, the rate of flux leaving or emitted must equal the rate of flux arriving or absorbing on the body and therefore the object's emissivity is equal to its absorptance. The characteristic radiation intensity for a body at a given temperature and emissivity allows for the true temperature

to be determined by an IR camera. Often, a high emissivity coating is applied to a surface to minimize reflections and allow the assumption of unity emissivity.

Modern cameras benefit greatly from improvements in imaging sensor technology. The most noticeable improvement came with the replacement of single point scanning cameras with focal plane array cameras commonly called CCD (charged couple device) or CMOS (complementary-symmetry metal–oxide–semiconductor) for the sensor measurement technique. Monolithic sensors built onto a silicon substrate are mostly used in visible light sensors but a few infrared detector materials such as PtSi, PbS, and PbTe have been demonstrated. In many ultraviolet and infrared detectors, a hybrid sensor where a detector structure is mounted to a separate silicon readout is employed. This gives greater material flexibility and twice the detector surface area, as the readout lines are not etched in the same surface. Various common infrared detector materials can be made in this hybrid format such as HgCdTe, InGaAs, and InSb. These sensor materials have wavelength dependent quantum efficiency curves, for example, indium antimonide (InSb) is most sensitive between 1–5 μm wavelengths (Near to Mid IR).

CCD and IR cameras operate on the same basic principles and the wavelengths they are sensitive to are fairly close so the size of the optics and general camera proportions can be the same. The optics are different as they need to be transparent to the wavelength of light being studied and thus IR transparent lenses are often opaque to visible light and vice versa. The shutter speed or integration time for digital cameras can be varied quite dramatically. At high framing rates, a short integration time is required. In order to get sufficient signals at high frame rates with a CCD camera, samples are often illuminated by bright external lights or lasers. With an IR camera, the samples temperature is the

radiation source and thus, in order to get very high frame rates, the sample must be at a relativity high temperature. The reason one can illuminate the sample with a bright light to increase the information with a CCD is that the primary method the radiation is getting to the sensor is by reflection of the visible spectrum off of the sample. With an IR camera, the radiation is emitted from the sample, not reflected from the surrounding environment, so a bright external light source could be detrimental.

2.2 Digital Image Correlation (DIC)

2.2.1 DIC fundamentals

There are a number of optical methods for measuring displacement and strain, such as holography, speckle interferometry, speckle-shearing interferometry, and moiré. Interferometric techniques are limited in that they require a stable platform and are not well suited outside the laboratory. The moiré technique is more robust but the fringe patterns produced need to be analyzed, which can be quite time consuming. The DIC approach does not have rigid stability requirements and the method is easily automated and scalable. The fundamental theory in DIC analysis is that the motion of numerous small subsets is matched in the sequence of images [95, 99]. The DIC method relies on searching a random surface pattern to track the motion of unique image subsets. The surface pattern should be of high contrast and random without preferential direction. The motion of each of these subsets is found via a correlation algorithm comparing the original image to the deformed one. The precision and accuracy of this tracking method is influenced by the applied speckle pattern and subset tracking size. Tracking many subsets allows the full field deformation to be tracked to subpixel accuracy. A key aspect

of this work is the introduction of digital image correlation (DIC) to provide motion correction on the infrared data, thus producing higher fidelity thermal images of deforming samples, which leads to improved TSA results.

2.2.2 Tracking particles with IR camera

In order to incorporate the DIC method for distortion correction of thermal data, a speckle pattern must be applied to the surface to provide tracking information. A contrasting speckle pattern in IR can be created by exploiting the thermal property of emissivity. Incident radiation can reflect from a surface, be absorbed, or transmit through a surface. The ratio of the energy for each of these modes is given by the reflectivity(ρ), emissivity(ε), and transmittance (τ), respectively, and must sum to unity. A model for the total energy that reaches the detector after being transmitted through the atmosphere is given by (2.31). The radiation (U) can be emitted from the body, ambient (*amb*) radiation can be reflected off the body or emitted by the atmosphere (*atm*) between the object (*obj*) and camera.

$$U_{tot} = \varepsilon\,\tau\,U_{obj} + (1-\varepsilon)\,\tau U_{amb} + (1-\tau)\,U_{atm} \tag{2.31}$$

$$U_{obj} = \frac{1}{\varepsilon\,\tau}U_{tot} - \frac{(1-\varepsilon)}{\varepsilon}U_{amb} - \frac{(1-\tau)}{\varepsilon\,\tau}U_{atm} \tag{2.32}$$

The body is assumed opaque and has no transmittance so the emissivity is ε and the reflectivity is $(1-\varepsilon)$. The atmosphere has some transmittance (τ) at the wavelength of interest and does not reflect so the emissivity of the atmosphere is $(1-\tau)$. The conversion of thermal signal to temperature requires the emissivity of the object and atmosphere be known or assumed. If a uniform temperature surface has two different

regions of emissivity, in the conversion from thermal signal to temperature one of the emissivities is applied to the entire surface. This leads to a correct value for temperature in one region and some error on the other. To find the temperature error resulting from an error in emissivity, the calibration relation (2.30) and the estimated energy from the body (2.32) are combined and differentiated with respect to emissivity.

$$\Delta T = \frac{\delta T}{\delta U_{obj}} \frac{\delta U_{obj}}{\delta \varepsilon} \Delta \varepsilon \tag{2.33}$$

$$\begin{aligned} T_{obj} &= \frac{B}{\ln\left(\frac{R}{U_{obj}} + F\right)} \approx \frac{B}{\ln\left(\frac{R}{U_{obj}}\right)} \quad assuming\ F \ll \frac{R}{U_{obj}} \\ \frac{\delta T_{obj}}{\delta U_{obj}} &= -\frac{B}{\left(\ln\left(\frac{R}{U_{obj}}\right)\right)^2} \frac{1}{\frac{R}{U_{obj}}} \frac{-R}{U_{obj}^2} = \frac{T_{obj}^2}{U_{obj} B} \end{aligned} \tag{2.34}$$

$$\begin{aligned} \frac{\delta U_{obj}}{\delta \varepsilon} &= \frac{-U_{tot}}{\varepsilon^2 \tau} + \frac{1}{\varepsilon^2} U_{amb} + \frac{(1-\tau)}{\varepsilon^2 \tau} U_{atm} \\ &= -\frac{1}{\varepsilon}\left(U_{obj} - U_{amb}\right) \end{aligned} \tag{2.35}$$

$$\Delta T = -\frac{T_{obj}^2}{B}\left(1 - \frac{U_{amb}}{U_{obj}}\right)\frac{\Delta \varepsilon}{\varepsilon} \tag{2.36}$$

Relation (2.36) gives the expected error on temperature for an emissivity error, where U_{amb} and U_{obj} are the sensor signals which can be determined using the calibration relation (2.30). When the emissivity error is positive (assumed higher than true) and the object is cooler than ambient the temperature error is positive in those regions of low emissivity. As long as the ambient temperature is not equal to the object, there will be some temperature difference between the two emissivity regions.

Simply applying a speckle pattern of white spray paint on a base black coating would provide insufficient information for DIC tracking in IR, as the emissivities of two standard spray paints are nearly identical. The resulting speckle pattern will have low contrast leading to poor DIC tracking. In order to perform DIC with an IR camera, the speckle pattern needs to be applied with lower emissivity paint thus creating a contrasting speckle pattern in IR even though the surface is at a uniform temperature. A main benefit of performing DIC on the infrared images is the simplicity of only using a single camera to obtain both thermal and deformation fields. A separate CCD camera for DIC analysis in the visual spectrum could be used but geometric and magnification corrections as well as time synchronizing the two-camera system adds complexity and possible sources of error. Another benefit of the single IR camera system is that no additional light source is required to illuminate the sample as the radiation is being naturally emitted. With a CCD camera, an external illumination source is required, which could introduce additional heat to the sample possibly, interfering with the TSA measurement or altering the material response. The limitations of using the single IR camera for both TSA and DIC are that IR cameras have lower resolution than CCD cameras and the applied lower emissivity speckles produce spots with different temperature variation than the high emissivity background and have to be dealt with either by removal or correction.

2.3 Combining TSA and DIC

The demonstration of the combined TSA-DIC method was performed on samples of an aluminum alloy 2024. The samples were square plates of side 50.8 mm (2”) and 3.18 mm (1/8”) thick. The thermal and mechanical properties of the materials employed in the

present investigation, aluminum 2024, cast nylon 6, and extruded acrylic are presented in Table 2.1.

Table 2.1: Material properties for TSA analysis

Material	α x 10-6 [oC-1]	ρ [kg/ m-3]	C_p (J/Kg-^{o}C)	Yield stress (MPa)	E (GPa)	ν	Sensitivity $\alpha/(\rho\, Cp)$ [MPa-K]-1
Al 2024-T6[a]	23.2	2780	875	> 345	72.4	.33	9.5375e-6
Nylon 6, cast[b]	63–180 Avg. 80	1110–1170 Avg. 1150	1670	40–100	1.3–4.2 Avg. 2.92	.39	4.1655e-5
Acrylic extruded[c]	60–110 Avg. 72	1150–1190 Avg. 1180	1470	45–86	1.38–3.30 Avg. 2.88	.37–.43 Avg. .402	4.1508e-5

[a][112], [b][113],[c][114]

The coefficient of linear thermal expansion, α, as well as the specific heat capacity, C_p, and elastic modulus, E, have a broad range of properties for both nylon and acrylic. The properties have little or no variation with temperature, particularly for the small temperature changes associated with elastic deformation. The thermoelastic sensitivity for each material was calculated based on the reported average material properties.

The emissivity of aluminum with an oxidized alumina surface is 0.2–0.3 [100] and thus at room temperature the majority of IR radiation detected is from reflections of the surrounding environment. In order to improve the thermographic signature, a uniform coating of high emissivity Krylon 1602 ultra flat black paint was applied to the samples. The spectral emissivity, from 3 to 14 μm, for this paint has been reported by Wan [115] and is reproduced in Figure 2.1 below.

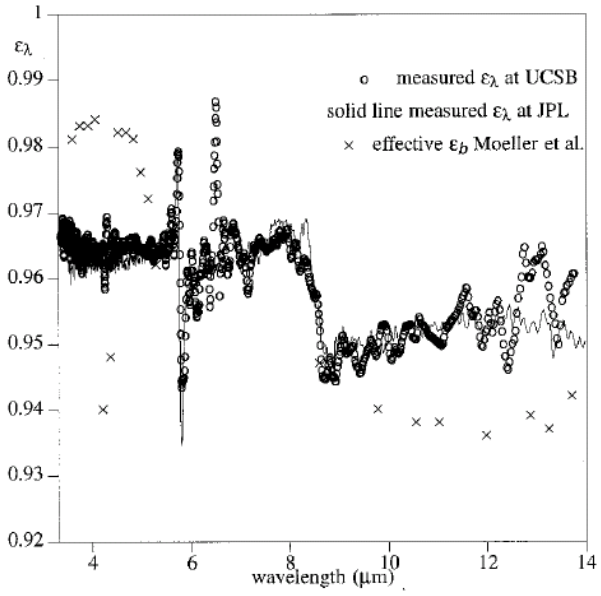

Figure 2.1: Spectral emissivities of ultra flat black paint (Krylon 1602) samples measured at University of California, Santa Barbara (o) and JPL (solid line), and the effective emissivities of the MAS blackbodies (x) [115]

Figure 2.1 shows that Krylon 1602 provides a high emissivity base coating of 0.96 [115] in the 3–5 μm range. Approximately 96 percent of the IR radiation would be emitted from the body with about 4 percent of the total radiation coming from reflected sources. The exact percentages will depend on the relative intensity of reflected source and body temperature. An inherent thermal contrast was created using low emissivity paint for the speckle pattern. The speckle pattern was applied via an airbrush which allowed for a large degree of control over speckle size and distribution. The paint was custom created by mixing 0.425cc of aluminum powder into a base of 4mL golden acrylic titanium white paint diluted with 2mL of water. An example of this speckle pattern is presented in Figure 2.2.

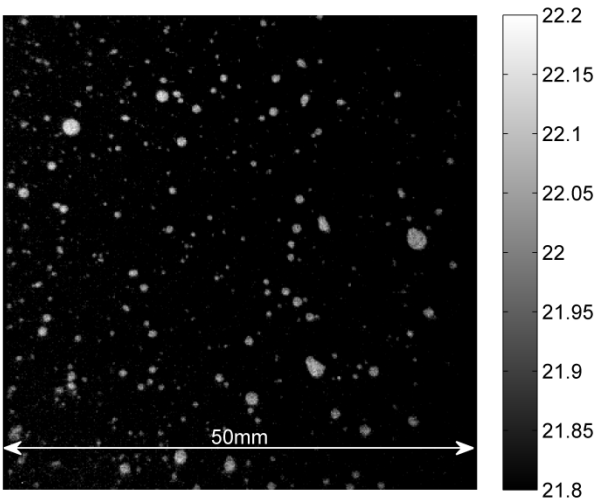

Figure 2.2: IR image demonstrating the speckle pattern thermal contrast (^{o}C) on uniform temperature aluminum sample with applied lower emissivity paint as speckles over high emissivity base (Krylon 1602)

A servo hydraulic testing machine (MTS, Model # 662.10A-08) was used to cyclically load the samples at a constant frequency (5 Hz) and with accurate prescribed displacements. The sample was subjected to cyclic tension-tension loading to alleviate clearance issues with the machine grips. The time varying temperature field was recorded using a sensitive IR camera FLIR SC6000 [101] with a resolution of 640 x 512 pixels at 10 frames per loading cycle. The IR camera has a temperature sensitivity of 20 mK. The framing rate was chosen to accurately track the time varying temperature field. The samples were cycled a number of times before recording allowing the samples to equilibrate and thus avoid recording any initial thermal transients. Each image of the thermal recordings was processed by a commercial digital image correlation software, VIC-2D [116], to determine the deformation map for each frame. The distortion of the IR image sustained during loading was corrected for using the deformation field determined for each frame from DIC. Thus, the temperature variation at each pixel is equivalently the temperature variation at a single material point. Utilizing a fast Fourier analysis (FFT),

the amplitude of temperature variation over time at the loading frequency was determined for each pixel. Utilizing the thermoelastic sensitivity, determined from material properties in Table 2.1, this measured temperature variation was converted to a sum of principal stress variation.

A demonstration of the potential benefit of the TSA-DIC method is shown below for a cracked 2024 aluminum sample with an applied speckle pattern. An initial notch 1.5 mm wide was cut halfway into the side of a 50.8-mm-wide 3.18-mm-thick aluminum plate to act as a stress concentration. The plate was then cyclically loaded in tension until a fatigue crack initiated. The combined TSA-DIC analysis was then performed at a stress level so as not to grow the crack but still provide sufficient thermal variation. The full field distortion field for each frame was determined via DIC. The DIC correction step removes the motion of the sample due to both rigid body motion caused by the loading apparatus and material deformation from loading forces. The temperature variation amplitude was found for each pixel after this DIC distortion correction, Figure 2.3(a), and the percent error when not correcting for sample motion is displayed in Figure 2.3(b). Errors on the order of 10% were observed in areas with high thermal gradients. The peak magnitude of temperature variation difference was approximately 0.06 ^{o}C, which corresponds to errors in stress level of approximately 20 MPa, thus demonstrating full field displacement correction improves temperature variation analysis.

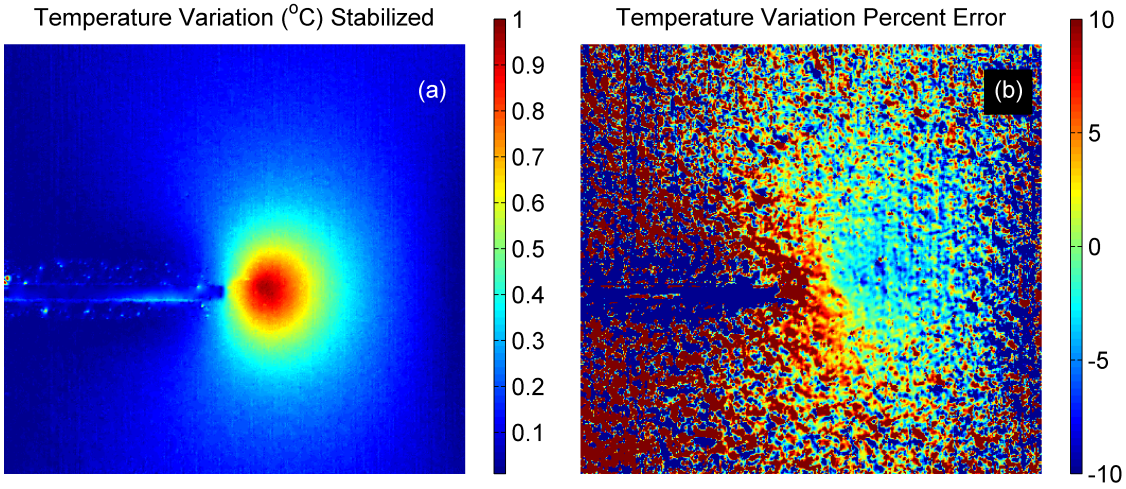

Figure 2.3: (a) Temperature variation around fatigue crack tip in Al2024; (b) Percent error when not accounting for sample motion and distortion

2.4 Performance Characterization of Combined TSA-DIC Method

2.4.1 Stress resolution

The particular stress resolution of TSA will depend on the material of interest but the noise floor for the temperature variation measurement is constant. The TSA noise floor of the SC6000 IR camera was determined by recording a static scene, Figure 2.4, at 20 fps. The temperature variation at frequencies from 1 to 10 Hz was determined using the FFT method and found to be fairly independent of frequency with a magnitude of 0.0105 ^{o}C, Figure 2.5. Thus, any temperature variation above 0.0105 ^{o}C could theoretically be determined. For example, the minimum observable stress for 2024 aluminum alloy would be 3.6 MPa and for acrylic would be 0.84 MPa, using the properties in Table 2.1.

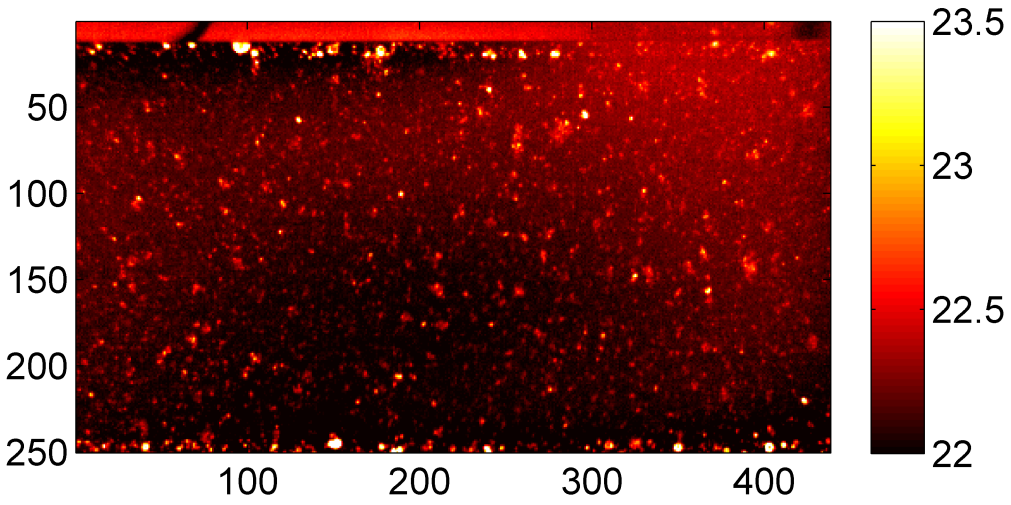

Figure 2.4: Temperature field (^{o}C) example during static test

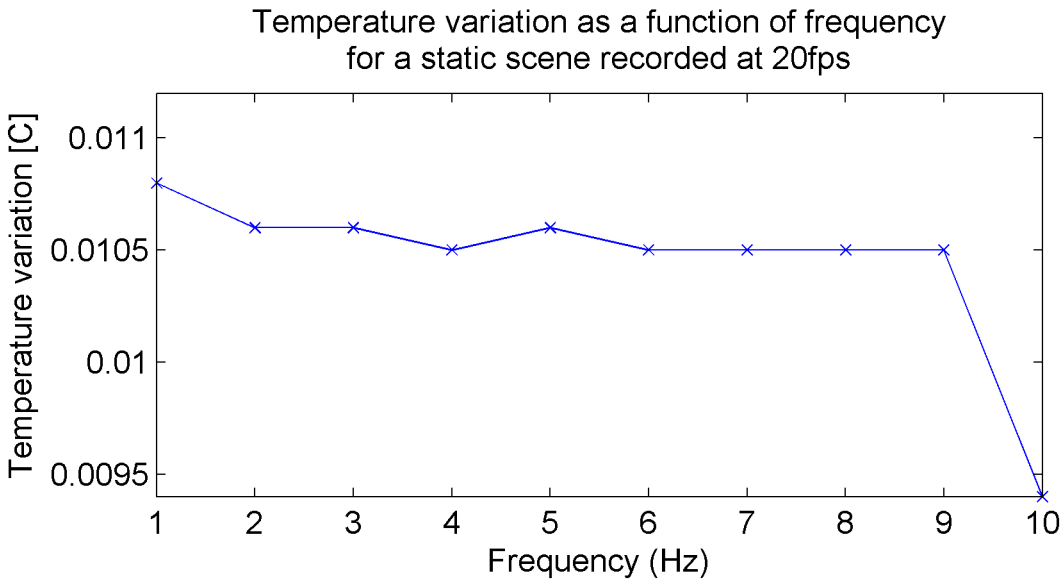

Figure 2.5: Temperature variation as a function of frequency for a static scene recorded at 20 fps with a SC6000 IR camera

2.4.2 Displacement and strain resolution

The DIC noise floor using IR images from the SC6000 camera was determined by recording a static scene, Figure 2.4, at 20 fps. The sample was prepared with a high

emissivity base coat followed by lower emissivity speckles. The pixel displacement and strain during the static test was determined using the VIC-2D software. The displacement range during the recording and variation at 1 Hz in pixels is presented in Figure 2.6. The maximum displacement range for a single location was 0.18 pixels with the average over-all range of 0.1 pixels. The strain field was also determined using the VIC-2D software for each frame of the static IR recording. The maximum range of strain found in the static recording was 1600 μstrain which occurred near the edges where data is less reliable. The average strain range was 450 μstrain. The average variation in strain at 1 Hz was 25 μstrain. This strain noise floor on range is comparable to other DIC measurements [97].

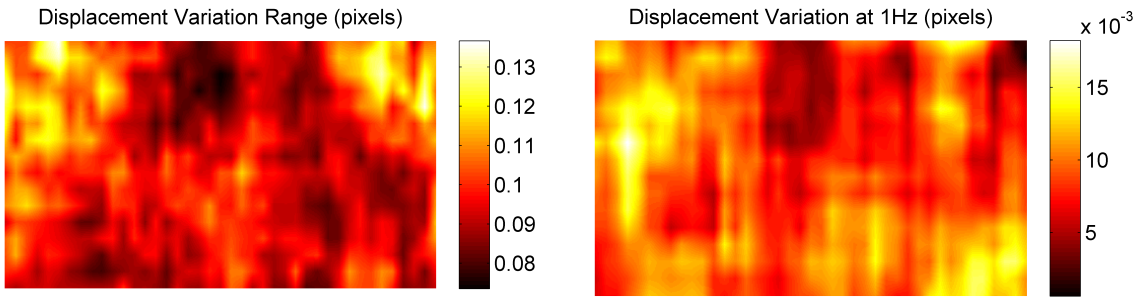

(a) (b)

Figure 2.6: (a) Displacement range and (b) variation in pixels at 1 Hz for a static speckled sample

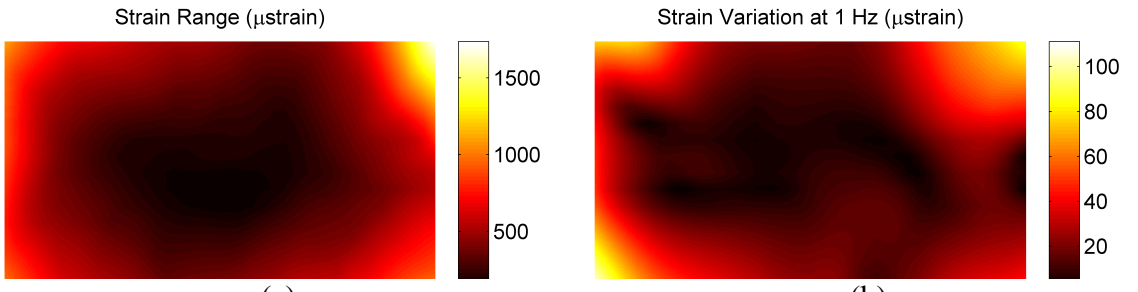

(a) (b)

Figure 2.7: (a) Strain range and (b) variation in μstrain at 1 Hz for a static speckled sample

2.5 Processing IR images for DIC

The IR sensor in the camera that is used in the present work (FLIR SC6000) is sensitive to radiation in the mid IR spectrum, 5–8 μm. Thus, for a given temperature of a sample, a characteristic amount of radiation will be incident on the sensor. This incident radiation is converted to an electric signal and displayed as 'counts' by the camera hardware. The number of 'counts' will depend on the intensity of incident radiation and the integration time of the camera. For each integration time, a calibration should be performed to correlate counts to a number of known temperature and emissivity conditions. In this work, the factory calibration for the camera was utilized. This calibration is also limited in the temperature range available due to the sensor electronics. For example, if not enough counts are registered it becomes difficult to distinguish between actual temperature reading and noise. If too many counts are detected during the integration time the sensor becomes saturated. Thus, for a given integration time there is a detectable temperature range.

The SC6000 IR camera has a 14-bit A/D conversion which allows for 16,384 different levels when converting from counts to temperature. The camera resolution is 640 x 512 pixels with a pixel pitch of 25 x 25 μm. The maximum frame rate is 126 Hz at full frame and can be increased if the frame size is reduced to a theoretical maximum of 36,982 Hz with a window size of 64x4 pixels. The maximum frame rate is limited by the maximum data rate for the chosen window size or the integration time. The high sensitivity of the SC6000 camera is measured by its noise equivalent temperature difference of 20 mK [101], meaning temperature differences larger than 20 mK are above the intrinsic noise level and can be detected. The sensor is cooled by a Stirling closed

cycle cooler so additional liquid nitrogen cooling used in other sensitive IR cameras is unnecessary. Compared to a standard CCD camera with 10 or 12 bit conversion, the SC6000 IR camera is able to detect finer variations in radiation intensity. The IR data is converted into standard image formats in order to utilize a commercial digital image correlation code VIC-2D [116]. Prior to converting the raw thermal data into image files a number of processing steps are taken to improve image tracking. During a standard combined TSA-DIC experiment, several hundred images were taken at 10 frames per loading cycle. The thermoelastic effect can change the temperature on the order of 0.1 ^{o}C, which is approximately the temperature difference between the background and the applied speckle pattern. This temperature effect allows the determination of sum of principal stresses but the changing temperature field causes difficulties in the DIC tracking software.

An example of the image processing before DIC analysis is presented below for thermal images of a cyclically loaded 50.8 mm wide 3.18 mm thick 2024 aluminum plate with a fatigue crack from a corner of an initial 1.5 mm notch. The sample surface was prepared by first applying a high emissivity surface coat of Krylon 1602 ultra flat black paint. A speckle pattern was then airbrushed with white airbrush paint mixed with a small amount of aluminum powder. The following images cover a view area of 33.5 x 37.1 mm and the scale bars indicate pixels with 10.35 pixels per mm. In Figure 2.8, the localized temperature change due to thermoelastic effect is evident during a single loading cycle. The varying local intensity at the crack tip makes it difficult for the DIC program to track the motion.

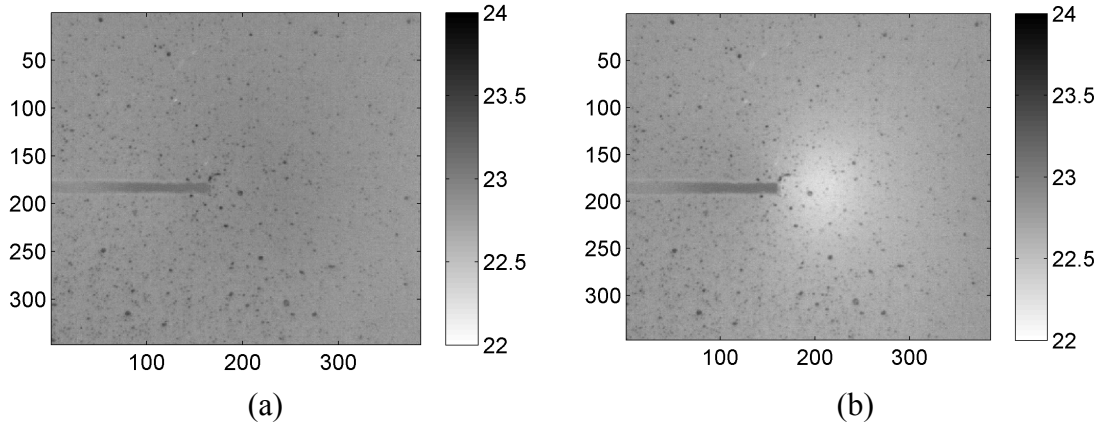

Figure 2.8: Raw temperature field (^{o}C) at two instances during tension-tension loading cycle of an aluminum 2024 plate with a fatigue crack demonstrating temperature change from thermoelastic effect

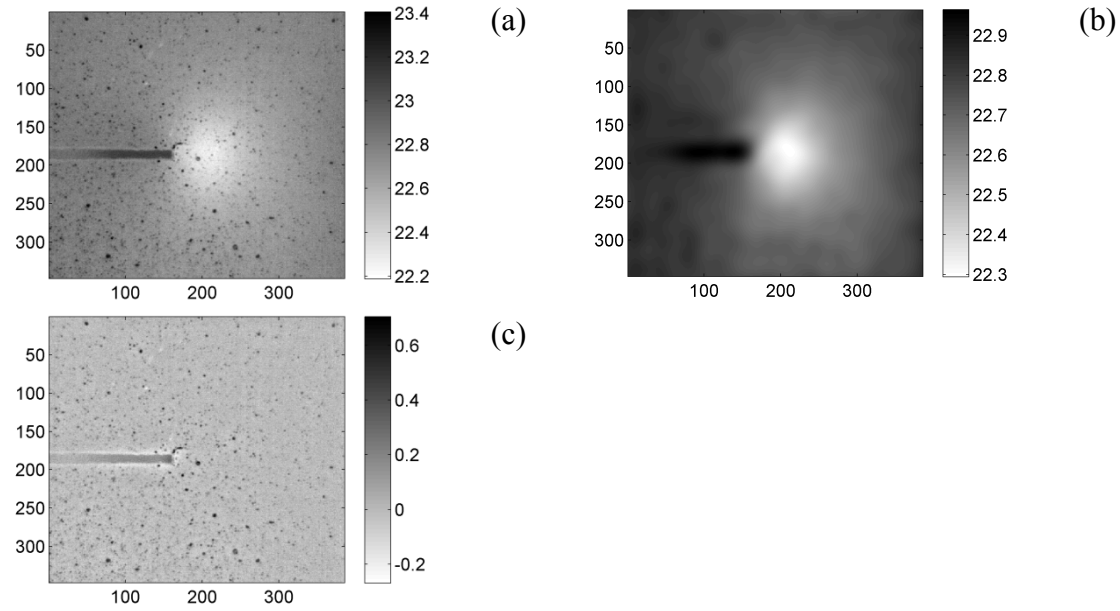

Figure 2.9: Example filtering process to improve DIC tracking. (a) Raw image; (b) Low frequency content; (c) After subtracting low frequency content (Units: ^{o}C)

In order to improve the DIC tracking, each image from the thermal recording was processed with a 2D filter in Fourier space to determine the low frequency spatial content Figure 2.9(b). The low spatial frequencies contain the gently varying temperature from

the thermoelastic effect, which was then subtracted from the raw image leaving a consistent background near zero with the speckles clearly visible in Figure 2.9(c).

In Figure 2.10(a), the difference between the two images from Figure 2.8 shows a bright region around the crack tip due to the temperature change from the thermoelastic effect that would make tracking with DIC difficult. In Figure 2.10(b), the difference between the corresponding filtered images is no longer temperature change dependent but due to the motion of the speckle pattern. The end effect is an image with consistent temperature distribution that maintains the presence of the speckle pattern for image correlation. By performing this filtering procedure on all the images in the sequence the DIC tracking of the speckle pattern can be improved.

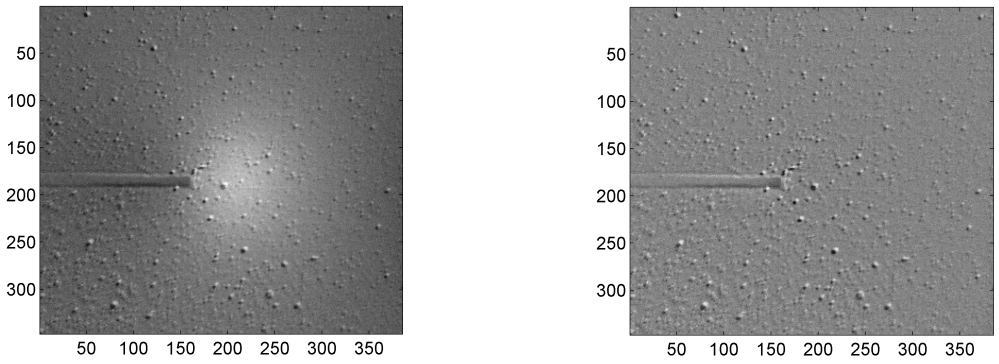

Figure 2.10: Difference between two thermal images from the same loading cycle: (a) before filtering showing thermoelastic effect and (b) after subtracting low frequency content from each image showing the speckle pattern clearly

During each combined TSA-DIC experiment, samples were cyclically loaded to induce a thermoelastic response recorded using an IR camera over a number of cycles. The raw temperature data was exported as thermal image files that were processed before performing the DIC analysis. The images were first filtered to remove low spatial frequency components from each image utilizing a 2D low pass Butterworth filter in

Fourier space with MatLab. The low frequency components encompass the background temperature and most temperature variation due to the thermoelastic effect. By removing these components, the appearance of the speckle pattern improves considerably and thus DIC tracking ability is improved. The resulting filtered files were converted to 16 bit TIFF image files for analysis with a commercial image correlation software VIC-2D.

The 2D deformation map for each image was found using the VIC-2D software and imported back into MatLab for the image correction step. The raw temperature files were corrected for this motion using a custom MatLab script such that the same material point remained located at the same pixel location in all frames. The frequency spectrum of the time varying temperature at each material point, Figure 2.11, was determined using FFT analysis. The amplitude of the thermoelastic effect was found by extracting the magnitude of the component corresponding to the loading frequency. This amplitude was found for each pixel, thus producing an image of the temperature variation distribution.

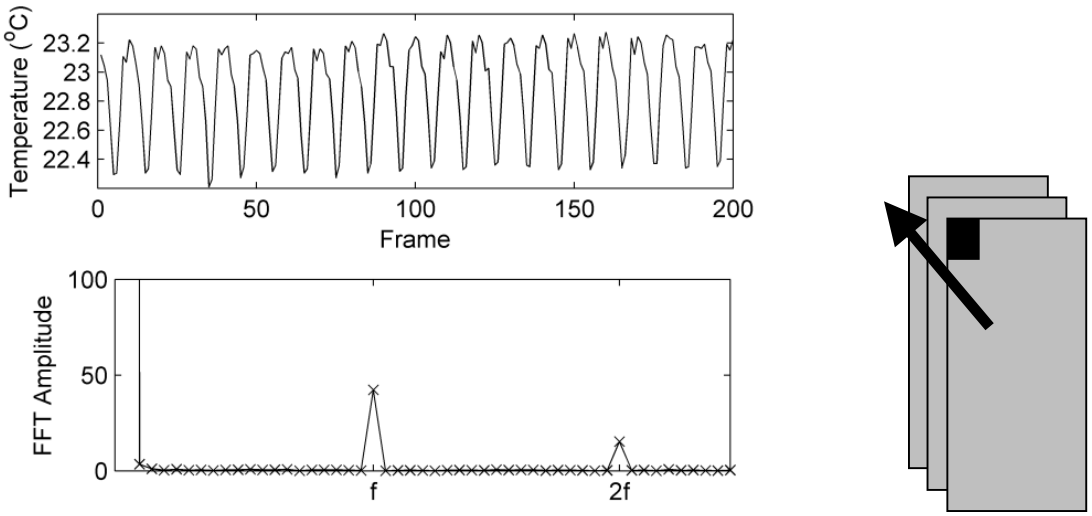

Figure 2.11: FFT analysis of the time varying signal for a single pixel. The large spike at index 0 represents the mean temperature while the spike at index f corresponds to the temperature variation amplitude at the loading frequency

In order to obtain the displacement maps with the IR camera, speckles of varying emissivity were used. The speckle pattern used for distortion correction is apparent in the temperature variation field. Since these speckles have a different emissivity than the background, the temperature variation is slightly different at a speckle, (2.36), and an example is visible in Figure 2.12. The thermal variation image can be enhanced by interpolating though each speckle from the background. The location of the speckles was determined with a high pass spatial filter and the temperature variation at these regions was removed from the resulting image. The holes created in the image were then filled in by interpolation from the boundary of each hole.

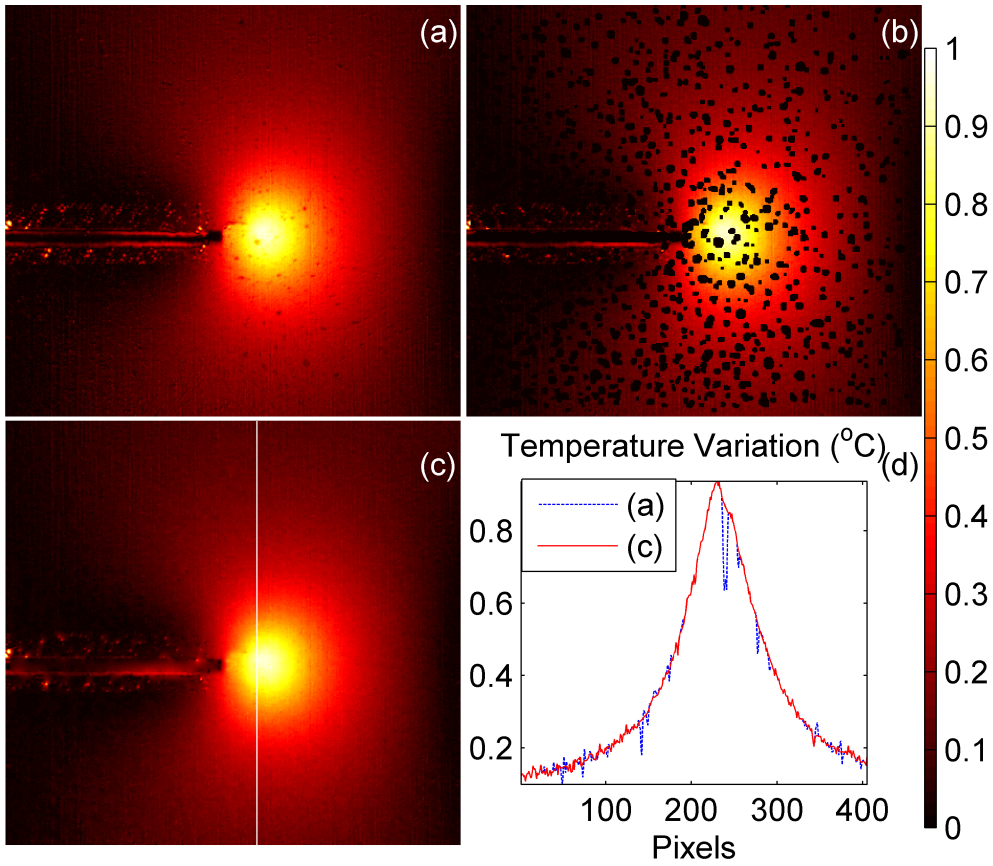

Figure 2.12: (a) Temperature variation around fatigue crack tip in Al2024 with speckle pattern emissivity effect; (b) Spot removal; (c) interpolated though spots (d) temperature variation along indicated vertical line before and after spot removal process

2.5.1 Thermal variation error

The precision of the FFT method to determine the thermal variation at the loading frequency was investigated by analyzing 9 image sets of 50 frames from a 500 frame recording, each subset covered 5 loading cycles. The standard deviation of thermal variation measurement at each pixel was determined from these repeated measurements. The mean thermal variation around the fatigue crack tip in an Al2024 sample is present in Figure 2.13. A line plot with error bars indicating the standard deviation of the amplitude measurement via FFT is presented in Figure 2.14.

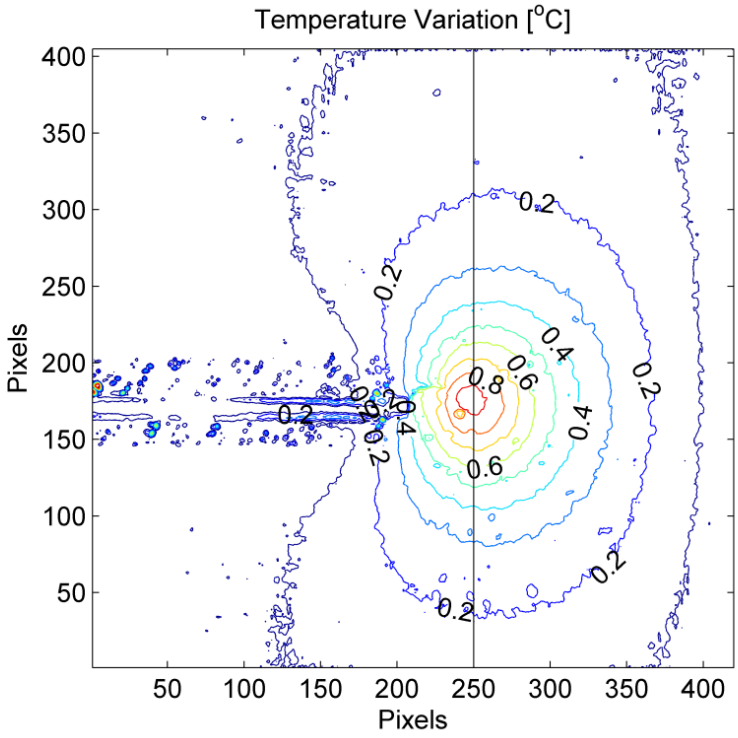

Figure 2.13: Mean thermal variation around fatigue crack tip with indicated line

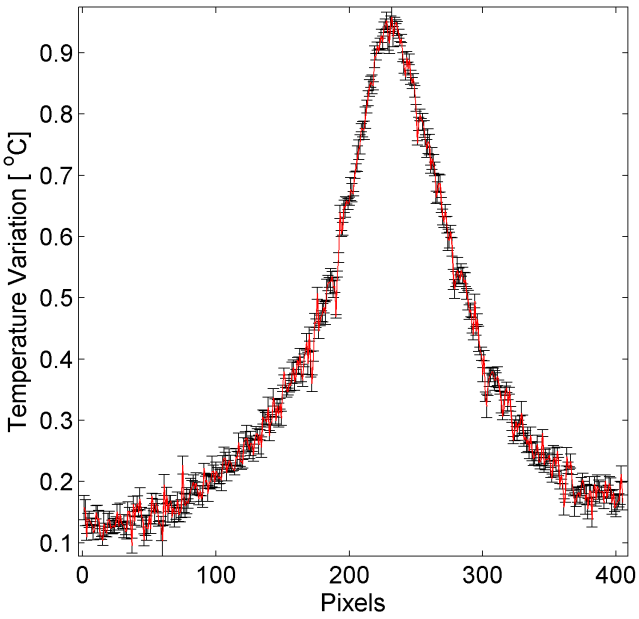

Figure 2.14: Thermal variation along indicated line with error bars equal to standard deviation of amplitude measurement via FFT

2.6 Combined TSA-DIC Examples

2.6.1 Plate with crack

As an example of the combined TSA-DIC method, the measured stress field via thermal imaging was compared to finite element simulations and theoretical stress distributions near a Mode I crack. A 1.54-mm-thick 51.5-mm-wide 2024 aluminum plate with a 24-mm-long and 1.2-mm-wide slot cut through the width was cyclically loaded in the servo hydraulic testing machine (MTS) to induce a thermoelastic response. The 200 mm long plate was held by friction grips 50 mm in height leaving a 100 mm long loading span. The plate was first coated with a high emissivity ultra flat black spray paint and then airbrushed with lower emissivity paint creating a random speckle pattern, Figure 2.15(a).

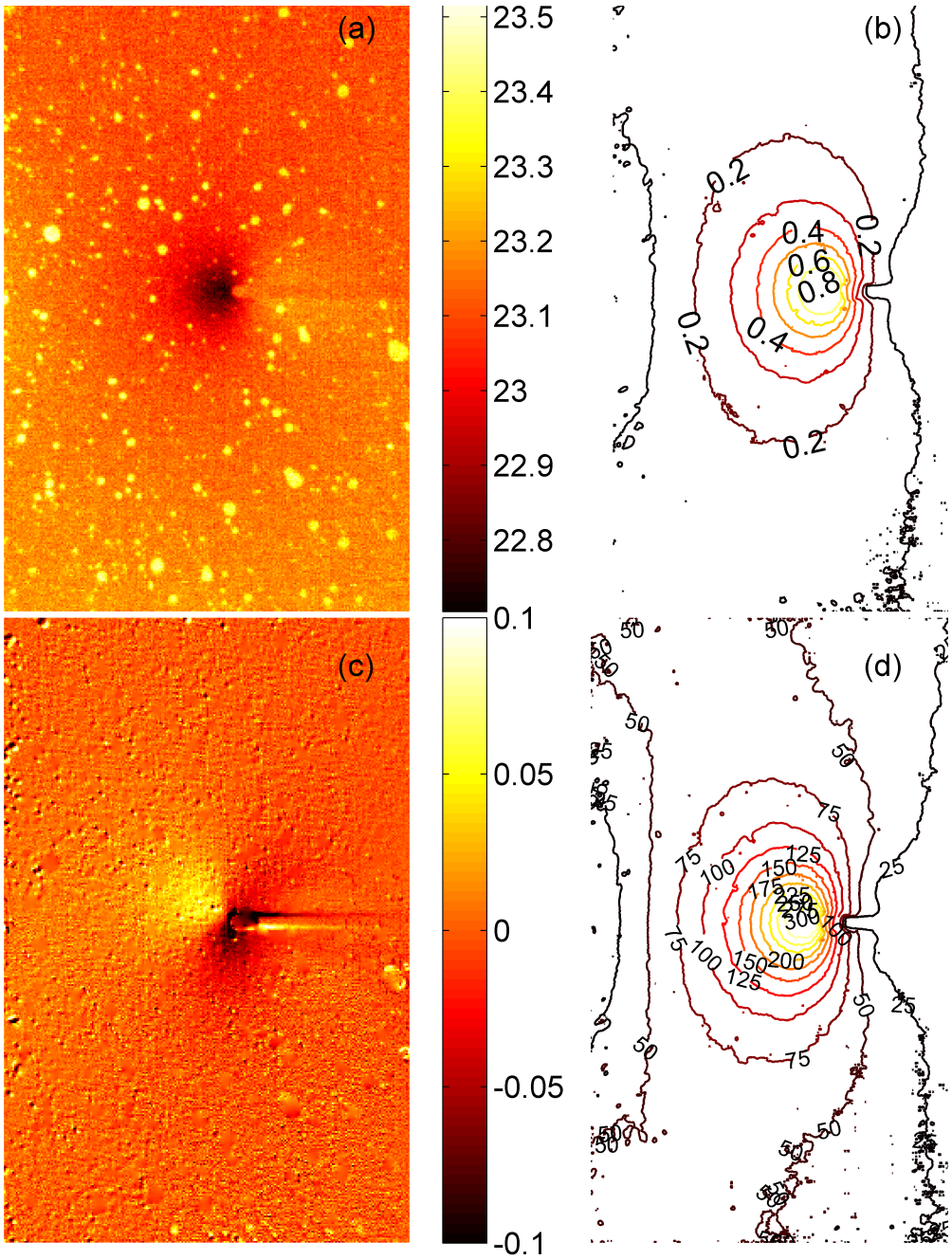

Figure 2.15: (a) Raw Temperature ^{o}C; (b)Temperature variation ^{o}C around Mode I crack in Al 2024; (c) Temperature variation difference with distortion correction; (d) variation in sum of principal stress (MPa) after applying basic TSA relationship to (b). 5.3 pixels per mm giving a field of view of 69 x45 mm

Utilizing the TSA-DIC method, the following temperature variation map was determined after correcting for the deformation caused by loading. Using the thermoelastic sensitivity for 2024 aluminum alloy (Table 2.1), this temperature variation can be converted to a variation of the sum of principal stresses using the basic TSA relation, (2.28). The plate cyclically loaded under tension-tension from 3828 N (48.2 MPa) to 96 N (1.2 MPa). As shown in Figure 2.15(d), the peak variation in the sum of principal stress was found to be approximately 320 MPa at the crack tip in this example. The yield stress of the 2024 aluminum alloy is approximately 345 MPa.

The theoretical stress distribution around a Mode I crack tip in an finite plate of width 'W' with crack of length 'a' is given in relations (2.37) to (2.40) [117]. The stress intensity factor 'K_I' indicates the magnitude of the stress in the vicinity of a crack tip from the applied far field uniform stress 'σ'. This single-edge notch tension (SENT) geometry requires a correction factor, Y, to modify the stress intensity factor to account for geometric effects since the sample is not an infinite plate. For the given geometry, the correction factor, Y, should be 2.89. The measured sum of principal stress field from TSA was compared to the theoretical stress around a Mode I crack with and without the stress intensity factor adjusted for geometric effects in Figure 2.16. The stress distribution at the crack tip does not match the theory likely due to a zone of plasticity and that the crack width is finite. Further from the crack tip, the stress matches more closely to the case without geometric correction, Figure 2.16bc, but diverges due to edge effects. Previous researchers [91] have used similar data to determine the stress intensity factors for mixed mode cracks in homogenous materials by matching stress contours to such theoretical distributions.

$$\sigma_{xx} = \frac{K_I}{\sqrt{2\pi\, r}} \cos\left(\frac{\theta}{2}\right)\left[1 - \sin\left(\frac{\theta}{2}\right)\sin\left(\frac{3\theta}{2}\right)\right] \tag{2.37}$$

$$\sigma_{yy} = \frac{K_I}{\sqrt{2\pi\, r}} \cos\left(\frac{\theta}{2}\right)\left[1 + \sin\left(\frac{\theta}{2}\right)\sin\left(\frac{3\theta}{2}\right)\right] \tag{2.38}$$

$$K_I = Y\,\sigma\sqrt{\pi\, a} \tag{2.39}$$

$$Y = \frac{\sqrt{2\tan\left(\frac{\pi a}{2W}\right)}}{\cos\left(\frac{\pi a}{2W}\right)}\left[0.752 + 2.02\left(\frac{a}{W}\right) + 0.37\left(1 - \sin\left(\frac{\pi a}{2W}\right)^3\right]\right. \tag{2.40}$$

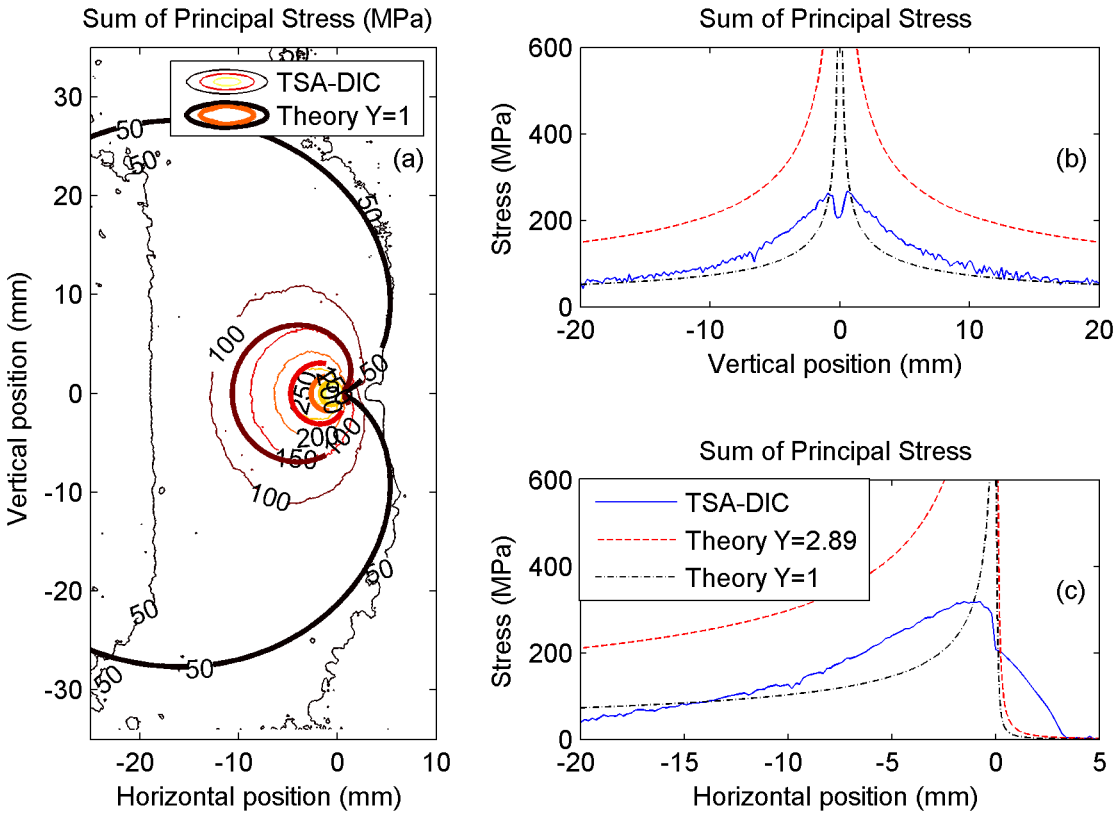

Figure 2.16: (a) Sum of principal stresses from theory and TSA; Stress along vertical line and (c) horizontal line through crack-tip comparing TSA and theoretical result for geometric correction factors Y = 1 and Y = 2.89

Utilizing the ABAQUS finite element analysis program, the stress field from the TSA method was checked using the applied force amplitude of 3733 N as a loading boundary condition in the vertical direction. A static analysis was performed on a 2D shell model

constructed of CPS4R elements matching the present geometry using material properties for 2024 aluminum alloy in Table 2.1. The top surface was fixed and the force load was applied to the bottom surface which was constrained to move uniformly in the vertical direction simulating the loading grips. There is good agreement in the magnitude and distribution of the sum of principal stresses when comparing the TSA and FEA simulation results (Figure 2.17). The discrepancy at the crack tip is likely due to a zone of plasticity as the stress exceeded the yield stress.

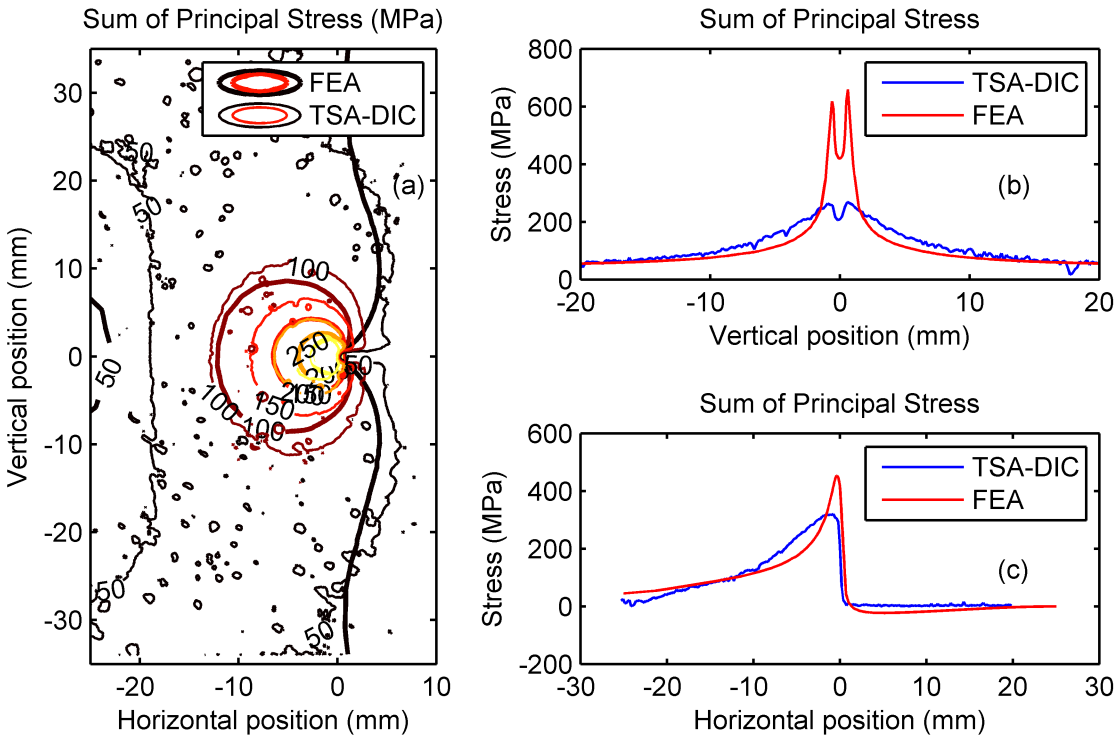

Figure 2.17: (a) Sum of principal stress field (MPa) around Mode I crack via TSA and FEA; (b) Stress along vertical line and (c) horizontal line through crack-tip comparing TSA and FEA result

In addition to the sum of principal stress field via TSA, the DIC aspect of this analysis allows the determination of displacement and strain variation as well. The vertical displacements (μm) measured with DIC and the FEA simulated displacements

are presented in Figure 2.18. The pixel variation amplitude was measured at 0.96 pixels on average and a minimum of 0.38 pixels at the top right. Using the minimum displacement at the top right region as a reference displacement (to account for rigid body motion), the bottom displacement of the cracked plate was 0.65 pixels or 0.12 mm, which is quite close to the FEA predicted maximum vertical displacement of 0.11 mm. Comparing the displacement and stress fields between the finite element simulation and DIC results, Figure 2.17 and Figure 2.18 demonstrates the ability of this method to simultaneously determine the stress field and record the displacement field accurately.

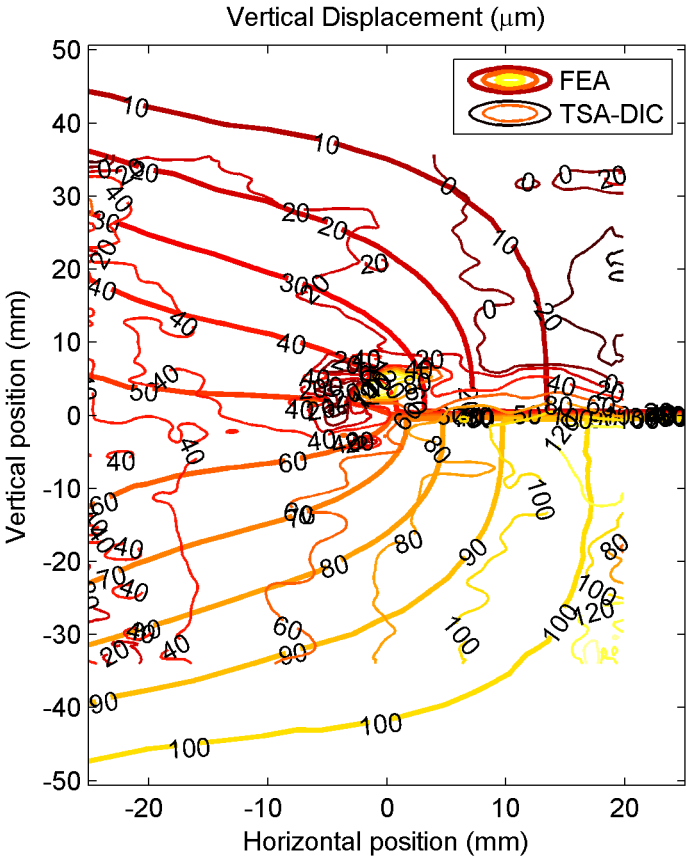

Figure 2.18: Vertical displacement (μm) in loading direction of Al2024 plate near edge crack from DIC and FEA

2.6.2 Plate with hole

A benchmark example using the combined TSA-DIC method was performed on a plate with a hole. In this example, a 50.8-mm-wide 3.2-mm-thick 2024 aluminum plate with a 9.42 mm circular hole in the center was prepared in a similar manner as the previous example, a low emissivity speckle pattern applied to a high emissivity basecoat. The sample was cyclically loaded under displacement control with an applied far field stress of 48 MPa. The sum of principal stresses from TSA was determined after correcting for motion and deformation using thermal DIC.

The theoretical stress distribution around a hole of radius 'a' in an infinite plate subject to an applied uniaxial stress, σ_o, is given in relations (2.41)–(2.43) where 'r' is the radial direction and 't' is perpendicular in the angle direction.

$$\sigma_{rr} = \frac{\sigma_0}{2}\left(1 - \left(\frac{a}{r}\right)^2\right) + \frac{\sigma_0 \cos(2\theta)}{2}\left(3\left(\frac{a}{r}\right)^4 - 4\left(\frac{a}{r}\right)^2 + 1\right) \tag{2.41}$$

$$\sigma_{tt} = \frac{\sigma_0}{2}\left(1 + \left(\frac{a}{r}\right)^2\right) - \frac{\sigma_0 \cos(2\theta)}{2}\left(3\left(\frac{a}{r}\right)^4 + 1\right) \tag{2.42}$$

$$\sigma_{rt} = \frac{\sigma_0 \sin(2\theta)}{2}\left(3\left(\frac{a}{r}\right)^4 - 2\left(\frac{a}{r}\right)^2 - 1\right) \tag{2.43}$$

Comparing the TSA-DIC results to the theoretical distribution of the sum of principal stresses (Figure 2.19) there is good correlation in magnitude and distribution. The stresses along a horizontal line through the hole center, Figure 2.20a, shows good agreement several radii away from the hole but does not capture the peak stress at the edge, likely due to difficulties resolving the small feature size. Along the vertical line through the

hole center, Figure 2.20b, the radial location of the measured zero stress transition is slightly larger than predicted by theory. Difficulties resolving the sharp stress gradients and DIC tracking issues at boundaries are the likely sources for the discrepancy between the TSA-DIC and theoretical results.

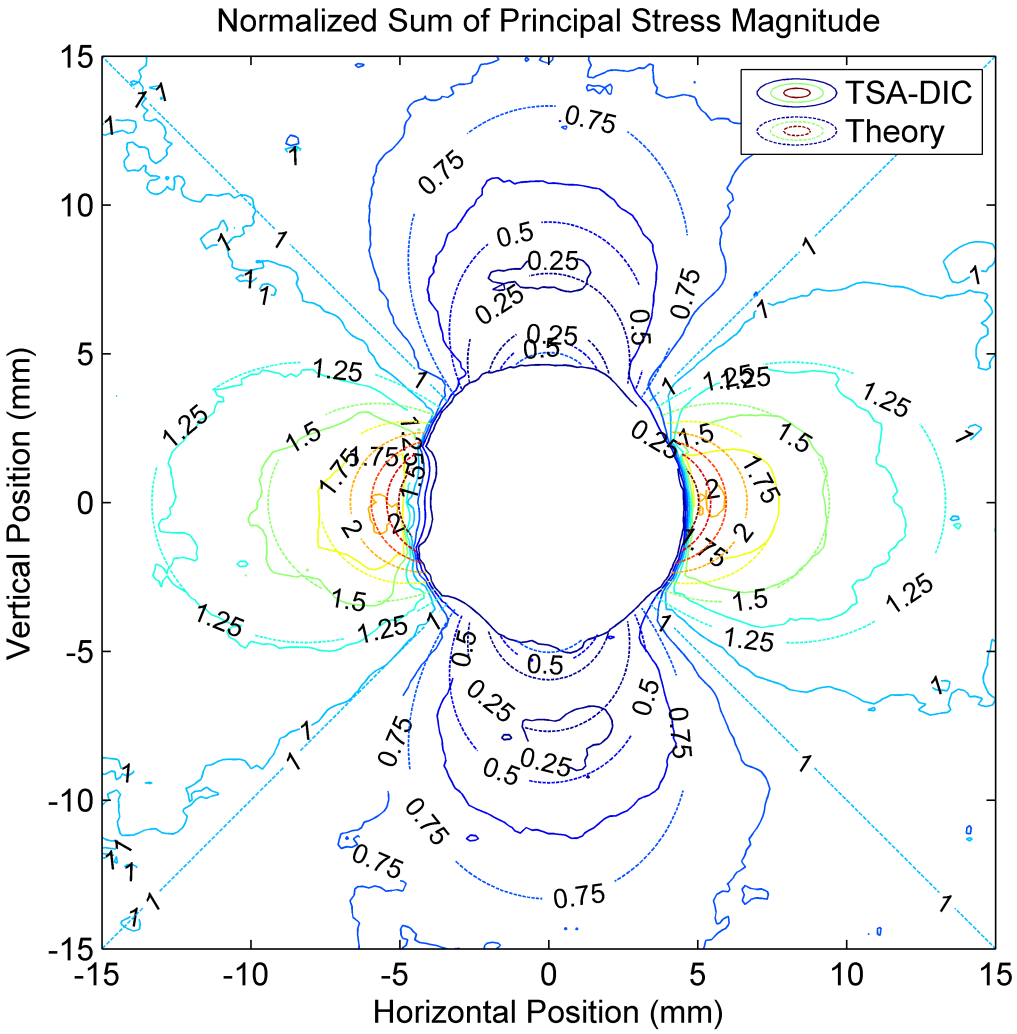

Figure 2.19: Sum principal stresses around 2024 aluminum plate 50.8-mm-wide with a 9.42 mm hole applied cyclic tensile stress comparing measured to theoretical stress distribution

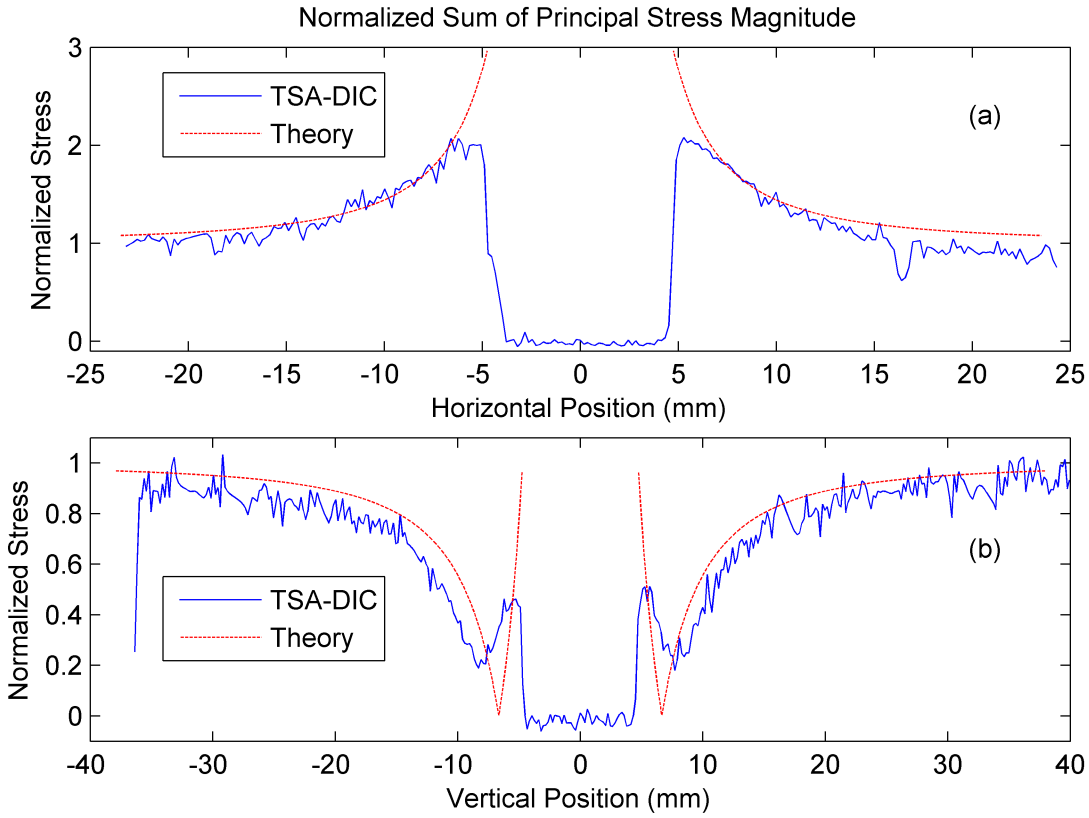

Figure 2.20: Comparing sum of principal stress magnitude between TSA-DIC method and Theory (a) along horizontal line and (b) along vertical line through hole for a 50.8 mm wide Al2024 plate with a 9.42 mm hole

An additional example demonstrating the combined TSA-DIC method was performed on a 49.8-mm-wide, 1.6-mm-thick nylon sample with a 25.4 mm circular hole in the center. The sample was cyclically loaded in the vertical direction with amplitude of 490 N. The measured deformation field from TSA-DIC analysis with single IR camera is presented in Figure 2.21 and compared to FEA results. The magnitude of the vertical displacement was on the order of 3 pixels, which corresponds to 0.5 mm amplitude. Utilizing the ABAQUS finite element analysis program, a static analysis was performed on a 2D shell model constructed of CPS4R elements matching the present geometry using material properties for nylon in Table 2.1. The experimentally applied displacement

amplitude was utilized as the FEA boundary condition. The resulting displacement magnitudes from DIC and FEA match reasonably well.

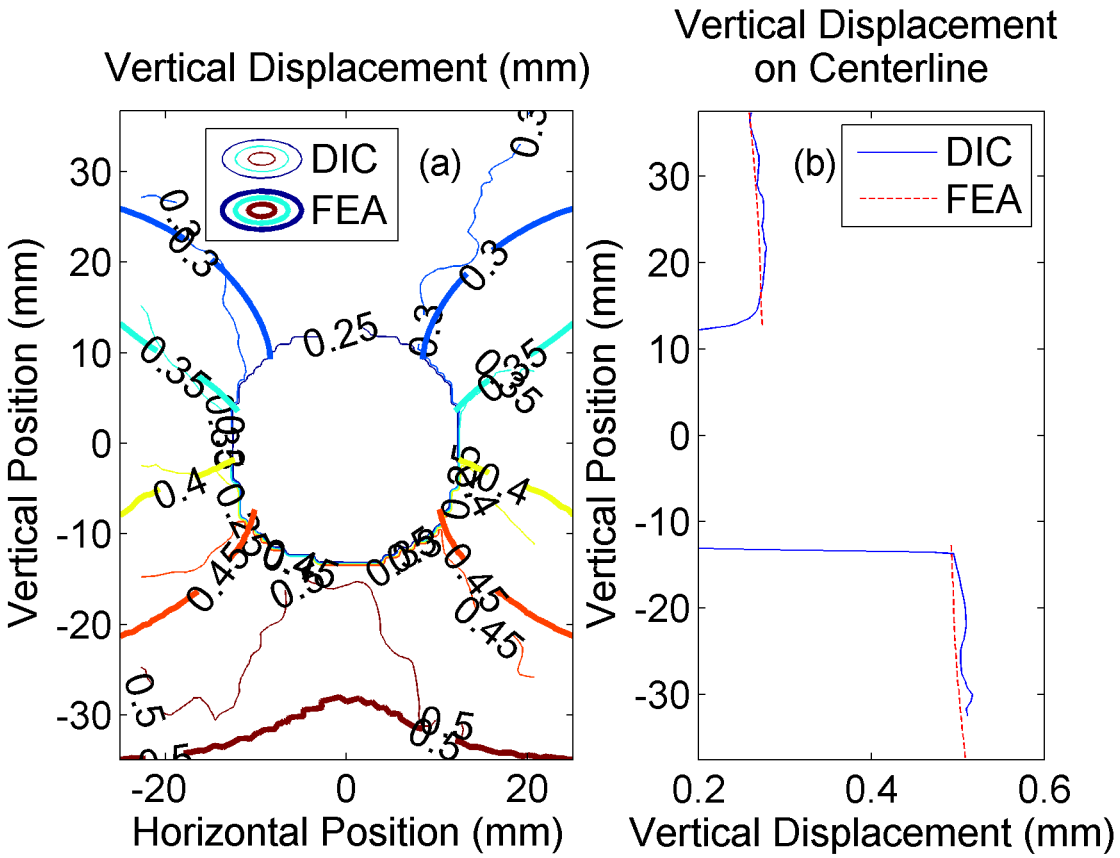

Figure 2.21: (a) Vertical displacement field form DIC and FEA; (b) Vertical displacement on vertical line through hole center

Utilizing the experimentally recorded displacements, the thermal images were corrected such each pixel represented a single material point. A TSA analysis that does not account for this pixel motion would result in an erroneous temperature variation field. The sum of principal stress variation field for a TSA analysis correcting for the sample displacement is presented in Figure 2.22(a). When the distortion is unaccounted for, an average temperature variation error of 0.04 ^{o}C was observed with regions up to 0.06 ^{o}C, which corresponds to stress errors of 5 MPa, Figure 2.22(b).

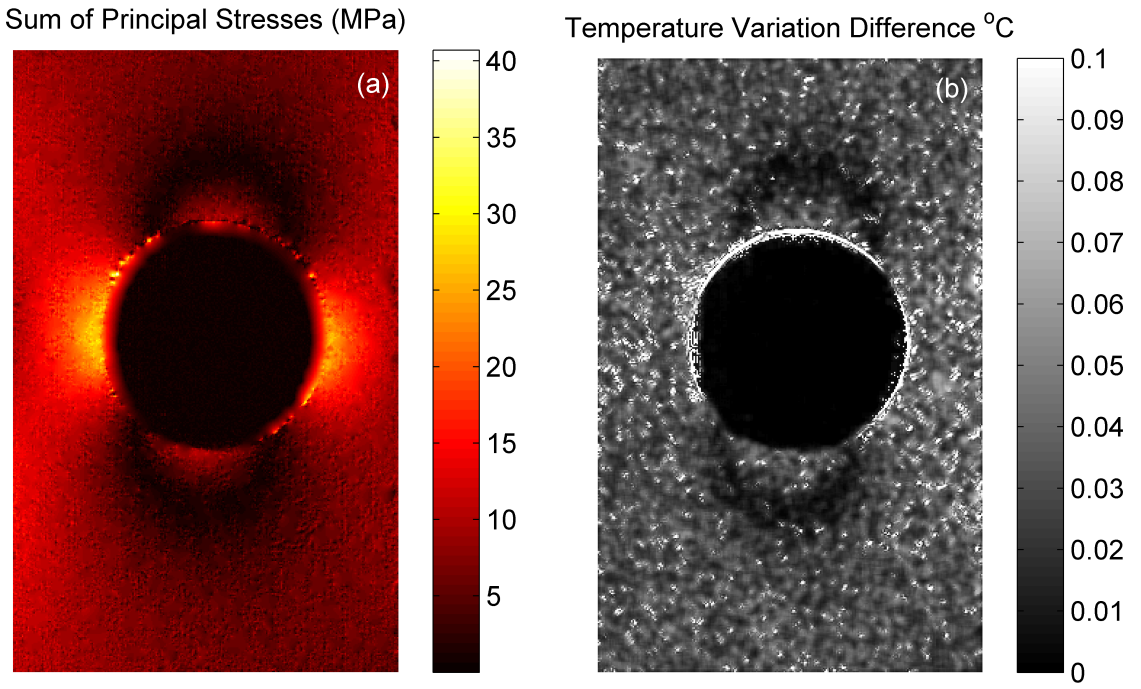

Figure 2.22: (a) Sum of principal stresses around cyclically loaded 49.8-mm-wide nylon plate with 25.4 mm hole after correcting for loading distortion; (b) temperature variation difference when not correcting for sample distortion. Field of view: 71 x 44.3-mm-with 5.98 pixels per mm

2.6.3 Bimaterial crack

To assess the applicability of the combined TSA-DIC method on structures comprising different materials, a crack at a bimaterial interface was investigated. The crack was created by gluing a 75-mm-wide, 10-mm-thick sample of acrylic to a 75-mm-wide, 10-mm-thick sample of nylon with a machined 0.38-mm-thick crack running a quarter (18.75 mm) way through the width. The sample was loaded under cyclic compression at 5 Hz at with a force variation of 6000 N. After the two samples were adhered, the surface was sanded to remove any residue and ensure a flush glue line along the interface. A coating of high emissivity flat black spray paint was applied followed by a lower emissivity speckle pattern.

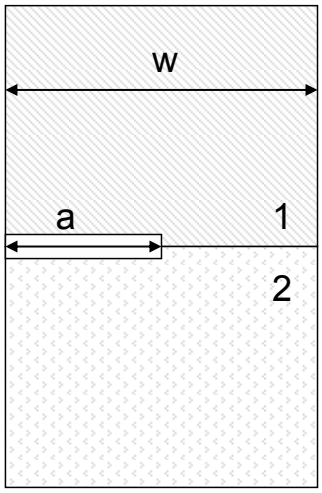

Figure 2.23: Bimaterial edge crack geometry W = 75 mm, a = 18.75 mm (a/W = 0.25) with 0.38 mm crack thickness. Material 1 is cast nylon 6 and Material 2 is extruded acrylic

For polymeric materials, it is not possible to obtain high accuracy in the thermoelastic response using material properties from published values (Table 2.1), due to their inherent variability. Either a number of high precision tests could be performed to determine these material properties (such as thermal expansion or heat capacity), or a single calibration could be performed. In the calibration test, a known cyclic stress field is applied to samples of acrylic and nylon with a servo hydraulic testing machine and the resulting temperature variation is measured via thermal imaging. The slope of the resulting calibration curve represents the combined effect of the material properties and is known as the thermoelastic sensitivity. The sensitivities for acrylic and nylon 6 are presented in Figure 2.24. The measured values fall within the range found in the literature (Table 2.1).

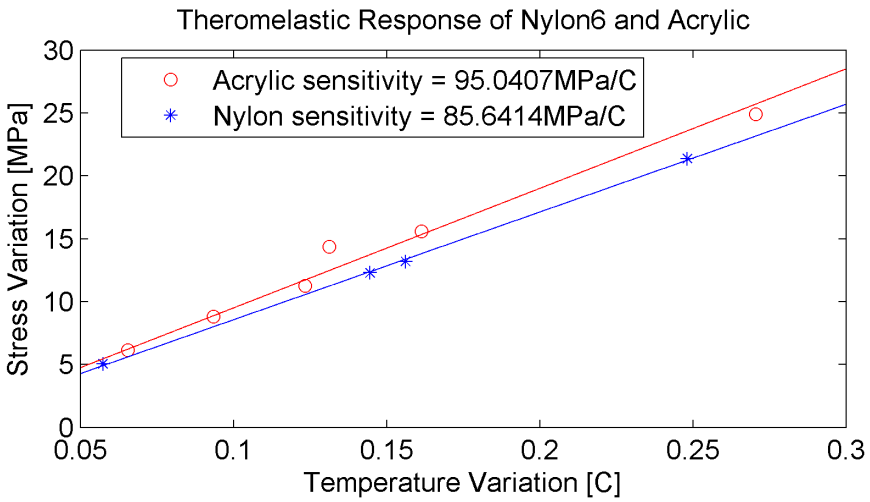

Figure 2.24: Thermoelastic sensitivity for acrylic (95.0 MPa/C) and nylon (85.6 MPa/C) determined from fitting of thermal response at various applied stress variations

The elastic modulus and Poisson's ratio can also be determined from the IR images by tracking the displacement of a few spots on the sample during a loading test. The applied stress variation can be determined either using the calibration factors in Figure 2.24 or using the applied force from the load cell. The deformation in the center region of each material was determined in the vertical (loading) and horizontal directions. The elastic modulus was determined by dividing the applied stress field by the measured strain in the loading direction. The ratio of strain in horizontal and vertical direction provided the Poisson ratio for these materials and fit in the range of expected values found in Table 2.1.

Table 2.2: Material properties of acrylic and nylon using IR displacement tracking

	Elastic modulus, E	Poisson ratio
Acrylic	2.758 ± 0.067GPa	0.42 ± 0.01
Nylon 6	1.69 GPa	0.292

The bimaterial cracked sample depicted in Figure 2.23 was cyclically loaded under compression and the resulting temperature variation was determined using the TSA-DIC

method. The displacement field was nearly uniform and too small to reliably discern any gradients, so the DIC portion of this case only corrected for the mean image motion. As shown in Figure 2.25, a discontinuity in temperature variation was found along the interface. In order to account for the two material thermoelastic sensitivities, the temperature variation image was separated into two images. The top and bottom images corresponding to nylon and acrylic respectively were multiplied by the respective calibration coefficient found in Figure 2.24. The resulting sum of principal stress variation map, Figure 2.26, was formed by combining the two scaled images together.

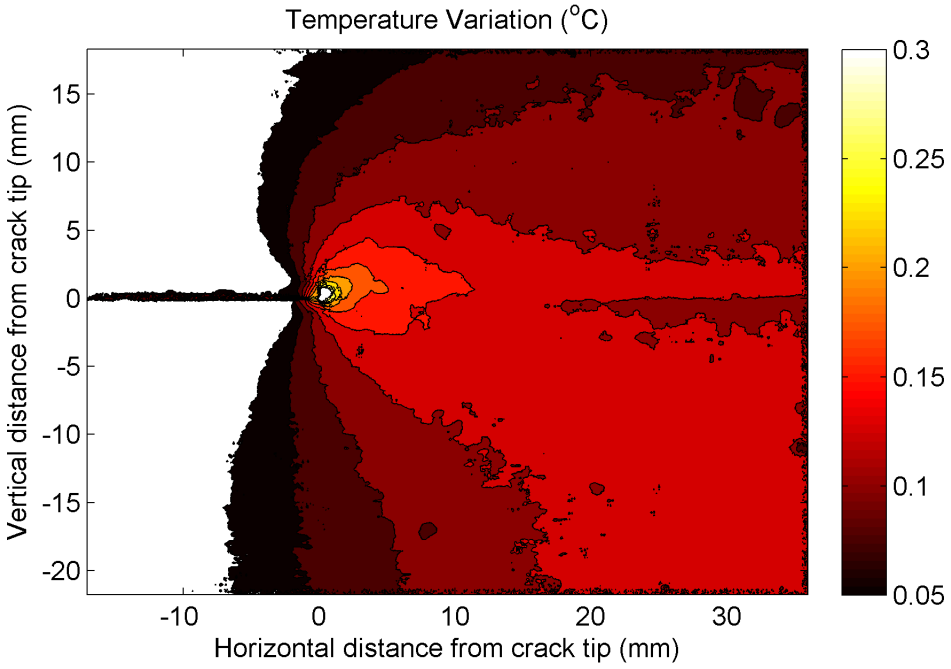

Figure 2.25: Temperature variation (°C) around bimaterial crack under 6000 N cyclic loading. Top material is nylon and bottom material is acrylic. Dimensions are in pixels with 10.6 pixels per mm giving a field of view of 40 x 52 mm

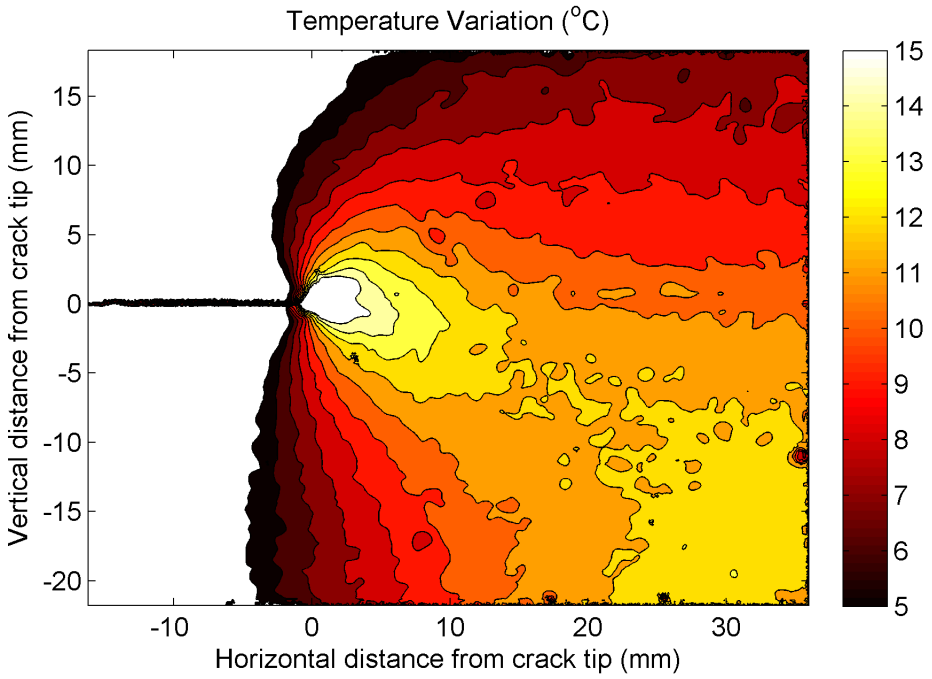

Figure 2.26: Sum of principal stress variation (MPa) around bimaterial crack under 6000 N cyclic compressive loading. Top material is nylon and bottom material is acrylic. Dimensions are in pixels with 10.6 pixels per mm giving a field of view of 40 x 52 mm

The stress field in Figure 2.26 reveals little to no discontinuity in sum of principal stresses across the interface. Clearly, there is asymmetry in the distribution of stresses in the two materials. A static 2D finite element model using the present geometry, material properties from Table 2.2, and the prescribed loading force of 6000N was created in ABAQUS. Discrepancies with the sum of principal stress contours measured experimentally and from the model, Figure 2.27, may be the result of differing boundary conditions. The stresses from the measured TSA and FEA results one pixel (94μm) above and below the interface are presented in Figure 2.28, which reveals a slight discontinuity near the crack tip. The TSA stress was lower than FEA but matches after one crack length from the tip.

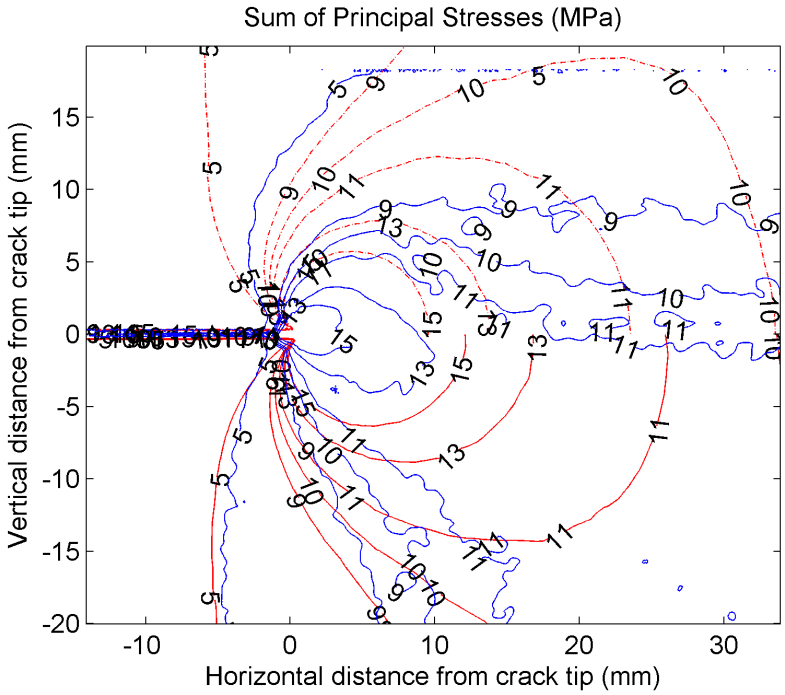

Figure 2.27: Sum of principal stress (MPa) for TSA and FEA results

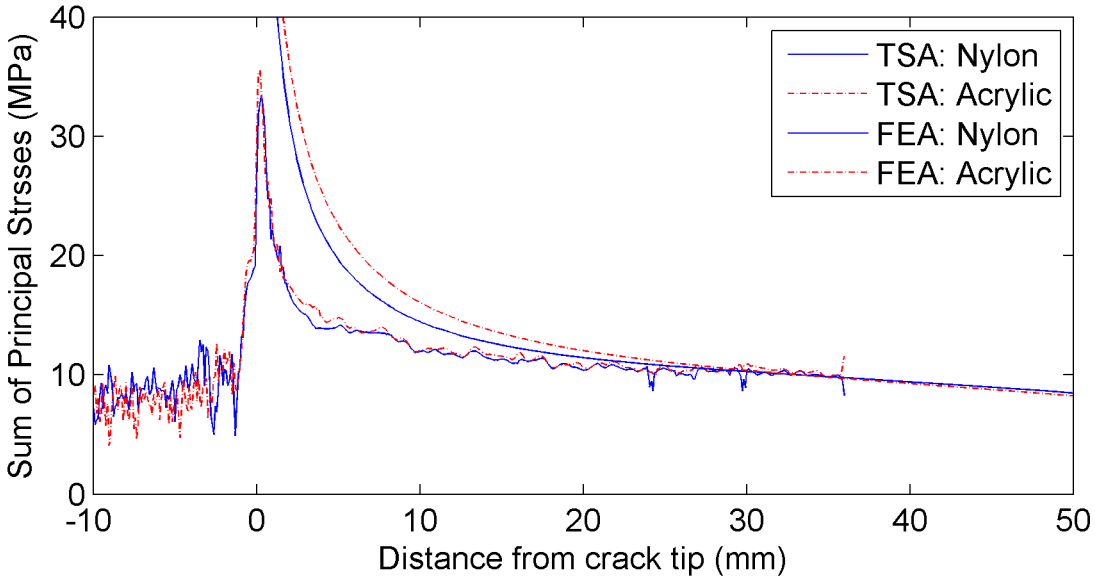

Figure 2.28: Sum of Principal Stresses (MPa); 1pixel (94 μm) above and below interface comparing TSA and FEA results

2.7 Conclusions

A methodology to combine two noncontact techniques, namely thermoelastic stress analysis (TSA) and digital image correlation (DIC) using a single IR camera has been developed. The ability to measure the thermoelastic effect and deformation with one camera greatly simplifies required data processing by not having to align two video streams in time or correcting for geometric effects of the relative camera positions. The key benefit of TSA is that the full field stress can be obtained without precise optical alignment and lenses required of other methods, such as coherent gradient sensing. Also, the very high sensitivity of the thermal camera combined with TSA can produce a full field stress measurement even when the deformations are too small for other methods. DIC allows the deformation field to be determined in a noncontact method but requires some surface preparation to provide a speckle pattern for tracking. A limitation of DIC is that the deformation field must be differentiated, which amplifies noise, to obtain the strain field, which then must be averaged and thus limits the resulting strain resolution. The deformation-induced errors in the TSA analysis were presented for example cases where areas of high thermal gradients and motion resulted in incorrect temperature variation amplitude. The combined TSA-DIC correction method was shown to improve the general TSA result in comparison to methods in which distortion is not accounted for, especially in areas with large thermal gradients. The fundamentals of thermoelasicity and development of the TSA method was presented along with the requirements for application of DIC with an IR camera. To apply DIC with an IR camera, the required speckle pattern must have thermal contrast to the surrounding body. The temperature difference as a function of emissivity was determined and utilized to produce a speckle

pattern with inherent thermal contrast, provided the ambient temperature is not identical to the body. Several examples of the combined TSA-DIC method were presented demonstrating the required image analysis for the DIC method with IR images. The resulting stress field was also compared to theoretical and finite element solutions and showed good agreement. TSA calibrations of acrylic and nylon were presented to produce accurate stress fields since published values, and thus the possible thermoelastic sensitivity varies over a range.

References

89. Pitarresi, G. and Patterson, E.A., *A review of the general theory of thermoelastic stress analysis.* Journal of Strain Analysis for Engineering Design, 2003. **38**(5): p. 405–417.
91. Dulieu-Barton, J.M., Fulton, M.C., and Stanley, P., *The analysis of thermoelastic isopachic data from crack tip stress fields.* Fatigue & Fracture of Engineering Materials & Structures, 2000. **23**(4): p. 301–313.
95. Chu, T.C., Ranson, W.F., Sutton, M.A., and Peters, W.H., *Applications of Digital-Image-Correlation Techniques to Experimental Mechanics.* Experimental Mechanics, 1985. **25**(3): p. 232–244.
96. Sutton, M.A., Cheng, M.Q., Peters, W.H., Chao, Y.J., and McNeill, S.R., *Application of an Optimized Digital Correlation Method to Planar Deformation Analysis.* Image and Vision Computing, 1986. **4**(3): p. 143–150.
97. Sutton, M.A., McNeill, S.R., Jang, J.S., and Babai, M., *Effects of Subpixel Image-Restoration on Digital Correlation Error-Estimates.* Optical Engineering, 1988. **27**(10): p. 870–877.
99. Sutton, M.A., *Image correlation for shape, motion and deformation measurements: basic concepts, theory and applications*. 2009, New York: Springer.
100. Maldague, X., *Theory and practice of infrared technology for nondestructive testing*. Wiley series in microwave and optical engineering. 2001, New York;: Wiley. xix, 684 p.
101. FLIR. *SC 6000 Datasheet* Available from: http://www.flir.com/WorkArea/linkit.aspx?LinkIdentifier=id&ItemID=19966.
102. Patterson, E.A., Ji, W., and Wang, Z.F., *On image analysis for birefringence measurements in photoelasticity.* Optics and Lasers in Engineering, 1997. **28**(1): p. 17–36.
103. Siegmann, R., Backman, D., and Patterson, E.A., *A robust approach to demodulating and unwrapping phase-stepped photoelastic data.* Experimental Mechanics, 2005. **45**(3): p. 278–289.

104. Tippur, H.V., Krishnaswamy, S., and Rosakis, A.J., *A Coherent Gradient Sensor for Crack Tip Deformation Measurements — Analysis and Experimental Results.* International Journal of Fracture, 1991. **48**(3): p. 193–204.

105. Rosakis, A., *Two Optical Techniques Sensitive to Gradients of Optical Path Difference: the Method of Caustics and the Coherent Gradient Sensor (CGS).* VCH Publishers, Inc., Experimental Techniques in Fracture (USA), 1993: p. 327–425.

106. Gough, J., *A description of a property of caoutchouc or Indian rubber; with some reflections on the cause of the elasticity of this substance in a letter to Dr. Holme.* Manchester Phil. Mem, 1805. **Second Series**(1): p. 288–295.

107. Weber, W., *Ueber die specifische Wärme fester Körper, insbesondere der Metalle.* Annalen der Physik und Chemie, 1830. **Band XX**: p. 177–213.

108. Thomson, W.L.K., *On the dynamical theory of heat.* Trans. R. Soc. Edin., 1853. **20:**(2610–283).

109. Thomson, W.L.K., *On the thermoelastic and thermomagnetic properties of matter.* Q. J. Math., 1857. **1**: p. 57–77.

110. Thomson, W.L.K., *On the thermoelastic, thermomagnetic and pyro-electric properties of matters.* Phil. Mag., 1878. **5**: p. 4–27.

111. Biot, M.A., *Thermoelasticity and Irreversible Thermodynamics.* Journal of Applied Physics, 1956. **27**(3): p. 240–253.

112. Matweb.com. *Aluminum 2024-T6* 2010; Available from: http://www.matweb.com/search/DataSheet.aspx?MatGUID=ecf8530875cb4ded9675b827f77bfac5.

113. Matweb.com. *Overview of materials for Nylon 6, Cast* 2010; Available from: http://www.matweb.com/search/DataSheet.aspx?MatGUID=8d78f3cfcb6f49d595896ce6ce6a2ef1&ckck=1.

114. Matweb.com. *Overview of materials for Acrylic, Extruded* 2010; Available from: http://www.matweb.com/search/DataSheet.aspx?MatGUID=632572aeef2a4224b5ac8fbd4f1b6f77.

115. Wan, Z.M., Zhang, Y.L., Ma, X.L., King, M.D., Myers, J.S., and Li, X.W., *Vicarious Calibration of the Moderate-Resolution Imaging Spectroradiometer*

Airborne Simulator Thermal-Infrared Channels. Applied Optics, 1999. **38**(30): p. 6294–6306.

116. Solutions, C. *Vic-2D 2009*. Available from: http://www.correlatedsolutions.com/index.php/products/vic-2d-2009.
117. Anderson, T.L., *Fracture mechanics : fundamentals and applications*. 3rd ed. 2005, Boca Raton, FL: Taylor & Francis. 621 p.

Chapter 3: Simulated Slamming Experiments on Sandwich Composites

The increasing use of sandwich composites in the marine environment is motivated both by the desire to push the performance envelope and for economic reasons. With sandwich composites, lighter marine craft can be produced which will improve the top speed for a given engine, or attain the same speed with a smaller engine while, reducing fuel usage. Additionally, marine vessels and structures such as oil rig decks are required to survive in the harsh marine environment and metal hulled vessels—either single skin, double hull, or sandwich composite with metallic facings—will suffer under the corrosive effects of seawater. The requisite maintenance cost over the operating life of a traditional steel hull vessel more than exceeds the additional costs for a polymeric sandwich composite ship. Polymeric sandwich structures do not suffer the same corrosive effects from seawater but are still subject to the same mechanical loads and wave loading as traditional ships. Wave and hull slamming are particular loads all ships must face and the effect of repeated slamming events on sandwich composite hulls is not well known.

Understanding the behavior and failure modes in the hull structure of high speed craft is necessary for the design of long lasting, safe vessels. Sandwich composites possess many desirable properties for ship design including weight reduction, noise and vibration suppression, and radar, thermal, and magnetic signature reduction; but these benefits come at the cost of increased complexity in design and manufacture. In particular, wave loading and hull slamming conditions pose a threat for high speed craft that is not fully understood. The high pressure pulse the hull experiences during a water impact is

repeated numerous times in the operational lifetime of a high speed sandwich composite vessel and understanding how these structures fail under repeated loading will allow improved future designs and provide insight for damage mitigation strategies.

3.1 Slamming Loading Device

The large number of hull slamming impacts these vessels can expect to experience makes studying the damage progression via water impact in the laboratory rather difficult, since replicating the sheer number of impacts would take an exorbitant amount of time. In addition, repeated impacts in water will cause non-quiescent conditions, which will create a different sea state for each slamming event. It is also difficult to monitor the progression of damage and failure modes in the bubbly environment created by panel slamming in water. Hence, a different approach, based on mechanical loading, is adapted to simulate repeated hull slamming. Inspiration from a mechanical shock replication device, Figure 3.1, replicating underwater explosive (UNDEX) loading via a hammer led to the idea that water slamming loads could be simulated with a mechanical slamming device. The slamming simulator magnitude and duration loading would be tailored to match the expected slamming hull surface loads. Such a mechanical slamming simulator (MSS) would make monitoring the damage progression feasible due to dramatically shortened time to repeat loading. Water impacts would more accurately capture the loading state, but at the expense that only a few impacts simulating hull slamming could be performed in a realistic time frame. Diagnostic instrumentation can be readily applied with the MSS as it allows easy access to the sample during loading without worrying about the effect of water on the instrumentation. Optical measurements during water impact loading are also difficult to perform as the electronics need to be protected from

water and the field of view is quickly blocked with water spray. Thus, with the mechanical slamming simulator, the frequency of loading can be dramatically higher and with simpler implementation of diagnostic instrumentation then water impacts.

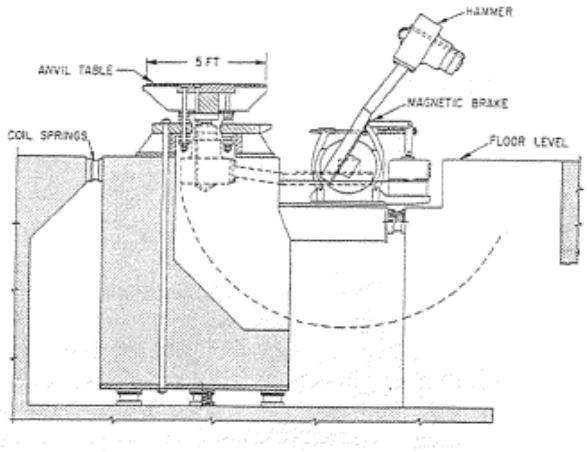

Figure 3.1: Mechanical shock testing machine simulating underwater explosive loads as described in MIL-S-901D [118]

A custom built mechanical slamming simulator (MSS) device, shown in Figure 3.2, was designed to operate for extended durations and is operated using compressed lab air. The loading source, a large pneumatic piston, used a pulse shaper to distribute load in a fashion similar to water loading. The hull slamming simulator was designed to sustain repeated loading of up to 22 kN (5000 lbf) on a sample of interest. A 15.24-cm-(6 in)-wide steel I beam with 12.7-mm-(1/2 in)-thick plates and webs was utilized as the base support structure. The large piston supplied the force and was attached to the beam via high strength steel bolts. A support structure of two 15.2 by 25.4 cm (6 by 10 in) aluminum plates 2.54 cm (1 in) thick was also mounted, providing support for the samples. To minimize pressure losses in the pneumatic plumbing, large 19 mm (3/4 in) diameter hoses and fittings were utilized. The device operated off the lab air supply and the pressure was set using large 25.4 mm (1 in) diameter high-flow regulators to

minimize restriction in the air flow and ensure a fast response of the piston. The pneumatic piston was chosen with large 19 mm (3/4 in) ports to provide faster response than standard 12.7 mm (1/2 in) or 9.5 mm (3/8 in) ports would allow.

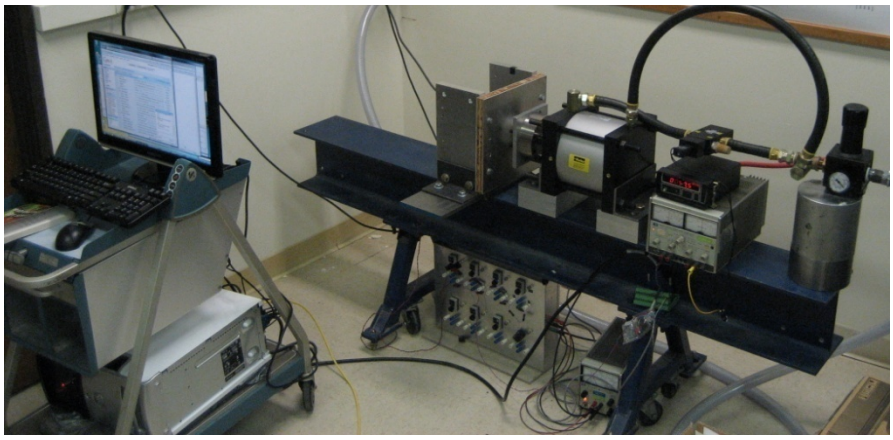

Figure 3.2: Hull slamming simulator facility for imposing dynamic loading on sandwich structures

The piston was manufactured by the pneumatic division of Parker Hannifin with a bore diameter of 20.3 cm (8 in) and a stroke length of 10.1 cm (4 in). The total force imparted by the piston was adjustable via inline high-flow regulators 25.4 mm (1 in) diameter (Parker model #P3NRA98BNG). A schematic for the device operation is shown in Figure 3.3.

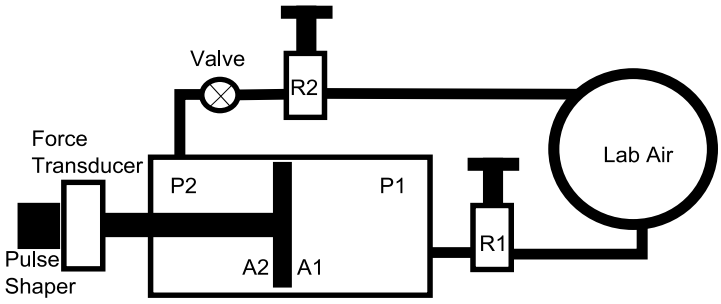

Figure 3.3: Schematic of the mechanical slamming simulator (MSS)

The maximum piston force was adjusted by a manual regulator (R1) and the extension was controlled by a 3-way solenoid valve (Parker model #B8W4ADG49A) with 19 mm ports. A second regulator was utilized to adjust the pressure on the opposite side of the piston wall. When the valve is closed, both sides of the piston wall are pressurized so that the sample is not loaded. After the valve is opened, the front side of the piston is evacuated with the pressure P2 reducing to atmospheric pressure and the resulting force applied by the piston is equal to pressure P1 times the piston cross-sectional area A1. The valve is then closed and both sides of the piston are pressurized, reducing the force from the piston to P1*A1-P2*A2. The area A1 was 0.0325 m^2 (50.2 in^2) and A2 was 0.0318 m^2 (49.2 in^2), which are not identical due to the 25.4 mm (1 in) piston rod. This process of opening and closing the solenoid valve can operate at frequencies up to 5 Hz and was controlled via a LabVIEW program. The LabVIEW program also acquired force data from a 33.3-KN-(7500 lbf)-capacity load cell (model # LPU-7.5K) from Transducer Techniques, and strain gages mounted to the sample (Figure 3.4) using a data acquisition board from National Instruments (model # PCI-6221). A unique benefit of using the pneumatic actuated slamming device is that it avoids the rising temperature of the machine grips commonly found in servo hydraulic testing devices such as the MTS. After sustained loading, the MTS machine grips themselves heat up from contact with the hydraulic fluid resulting, in thermal gradients in the samples.

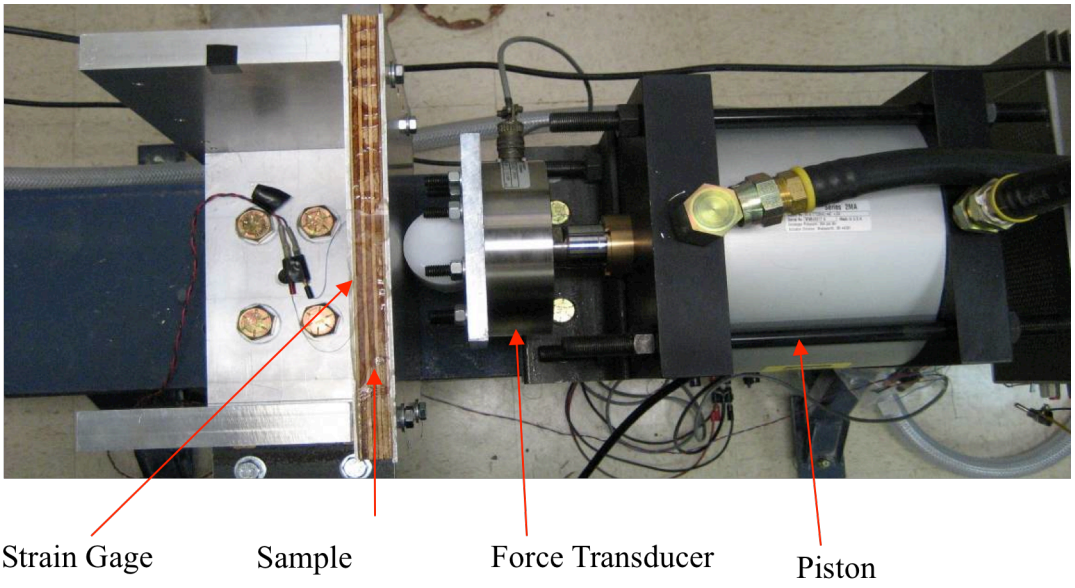

Figure 3.4: Close-up view of the MSS device

3.2 Design and Performance Characterization

The design of the slamming device allows for repeated loading on the order of a few Hertz. The maximum force obtainable was determined by the supplied pressure times the piston cross-sectional area. The maximum possible pressure the piston, hoses, and fittings can sustain is approximately 1 MPa (150 psi), the cross-sectional area was 0.0325 m^2 (50 in^2) thus giving a maximum design force of 32.5 kN (7300 lbf). The lab air pressure supply was 0.5 MPa (75 psi) and thus the maximum force obtainable in practice was 16.25 kN (3650 lbf). The piston force could be adjusted with the high-flow regulators R1 and R2 by setting the desired pressure, P2, on the far side of the piston (see Figure 3.3). The default state has both sides of the piston wall at nearly the same pressure. When the valve was opened, the fore side of the piston evacuated and the force on the piston plate increased due to the resulting pressure differential. The large diameter of the high-flow regulators minimized pressure losses, thus preventing long time delays in maintaining the

pressure on the piston. The piston extended until it was resisted by the sample with the applied force equaling the force from the pressure differential.

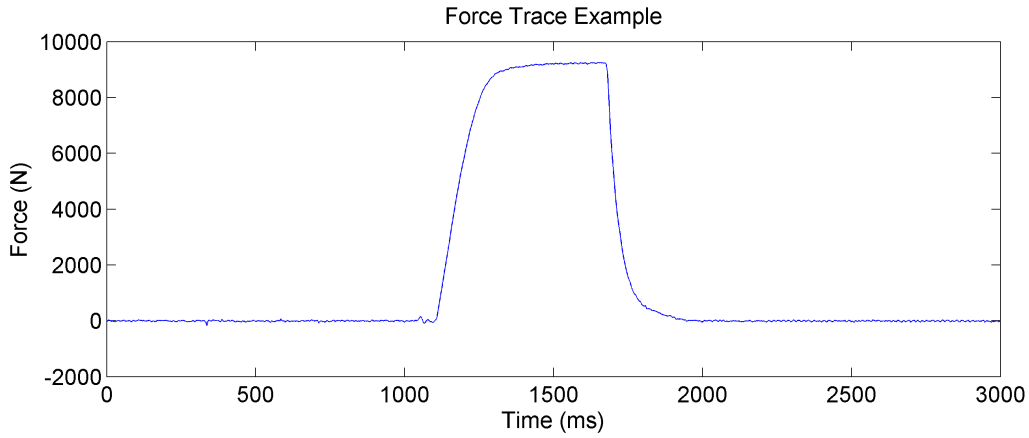

Figure 3.5: Example of MSS force trace on a rigid structure

The force trace in Figure 3.5, shows a representative loading cycle. The average rise time up to peak force was on the order of 100 ms; approximately 44.5 N/ms (10 lbf/ms) with an average fall time approximately half the rise time. Using these average rise and fall times to peak force, the minimum period was 200 ms, giving a maximum frequency of 5 Hertz. In practice, the mechanical slamming simulator was operated below 3 Hertz for long durations to ensure proper operation of the piston and to reliably reach the expected peak force.

3.2.1 Pulse replication

A general wave slamming pulse is composed of a high magnitude, short duration pressure pulse traveling along the panel, followed by a significant residual pressure (see Figure 1.2). In simulating the slamming pressure event with the MSS, a long duration representative average pressure was chosen as the magnitude for the cyclically loaded samples. Since the majority of slamming energy is found during the long duration

residual pressure pulse, it is reasonable to believe the high cycle damage growth is strongly influenced by the relatively long duration residual pressure. Thus, the aim of the mechanical slamming simulator pressure matching was to match the duration and magnitude of the average pressure during a slamming event.

The theoretical pressure profiles discussed in Chapter 1 can be found by solving a similarity solution [10]. The residual pressure coefficient can then be determined from the numerical solution. Pressure measurements from a model slamming test [119] are shown in Figure 3.6: the duration of the impulsive peak duration is on the order of milliseconds while the entire pressure pulse can last several hundred milliseconds. The duration of the pressure loading depends on several factors, namely, the size of the panel, the entry velocity, and the slamming angle. For example, at the same velocity a larger panel would sustain a longer duration pulse with the speed and size of the panel determining the time before the entire panel is submerged.

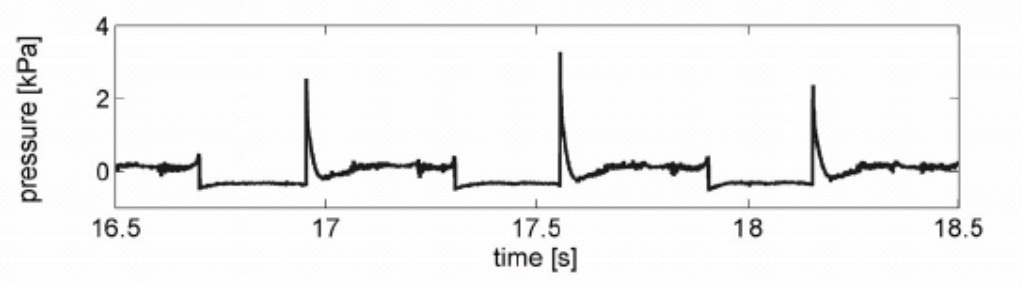

Figure 3.6: Typical pressure during model slamming events [119]

Utilizing finite element modeling, several geometries and materials were investigated in the design of the pulse shaper or impactor. The impactor designed would ideally emulate the magnitude and distribution of the slamming load while maintaining contact with the sample during loading. Several impactor geometries were tested, as shown in

Figure 3.7, along with the resulting pressure distribution along the contact surface. Initially, nylon with a nominal elastic modulus of 4 GPa was investigated as the impactor material as it would deform more under loading than metal and distribute the pressure. Comparing the trapezoidal to the rectangular impactor geometries in Figure 3.7, the peak pressure increased by a factor of three even though the contact area decreased by a factor of two under identical applied force. The cylindrical impactor gave a peak pressure four times the rectangular impactor under the same applied force.

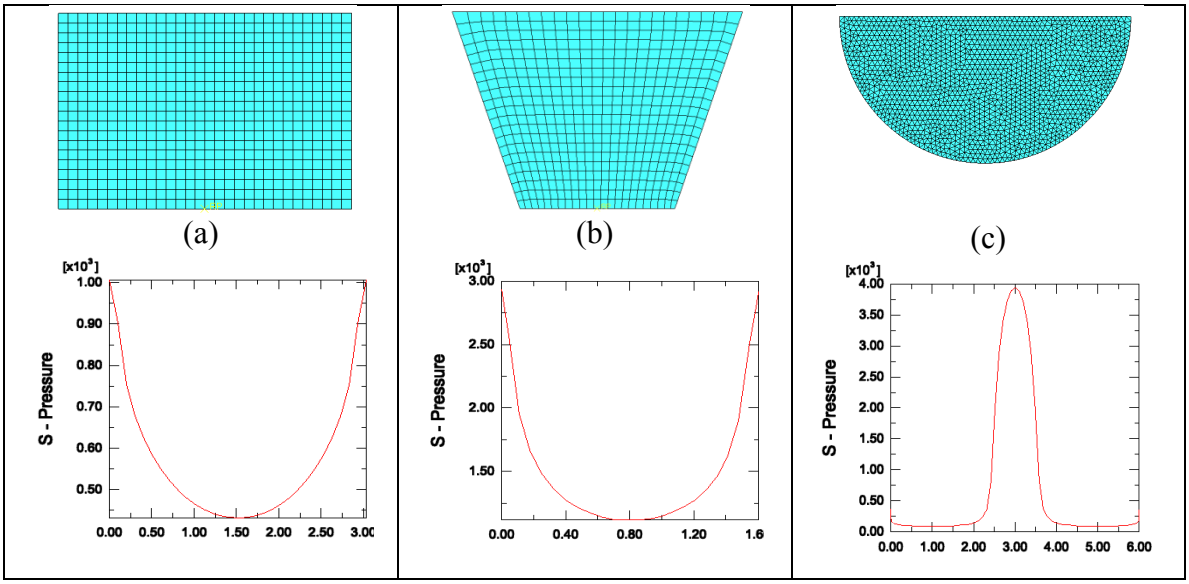

Figure 3.7: Pressure distribution along contact edge for several nylon impactor geometries utilizing finite element analysis. (a) Rectangle (b) Trapezoid, (c) Cylinder. Same loading force is applied in all cases

Several geometries were testing on simply supported sandwich composite beams with 50 mm H100 PVC foam core and 2 mm quasi-isotropic carbon fiber reinforced epoxy composite skins covering a 228 mm span. In practice, when the nylon cylinder was used to impact a composite sandwich beam, the localized high pressure resulted in indentation failure, as shown in Figure 3.8. This failure mode is undesirable as it is not normally observed in wave slamming damage.

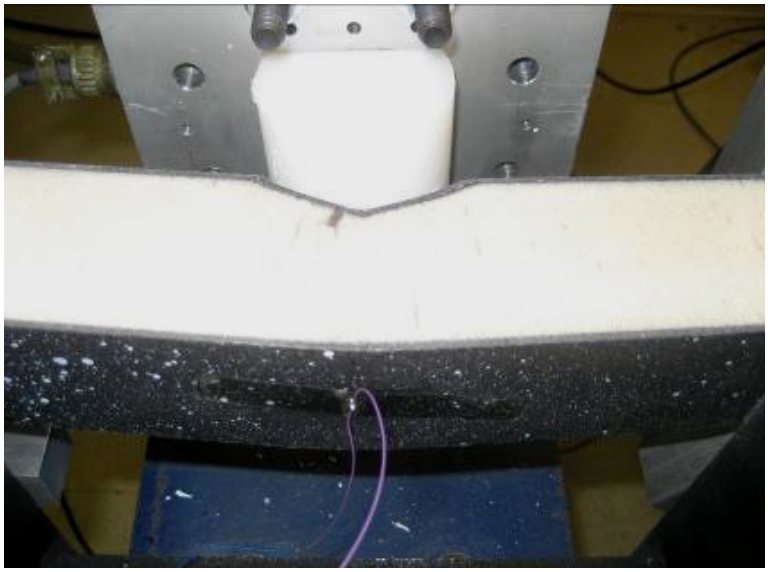

Figure 3.8: Indentation failure of sandwich structure under repeated slamming using nylon half cylinder impactor

The effect of the impactor's elastic moduli on the pressure distribution at the contact interface with the sandwich composite beam was analyzed using the commercial finite element program ABAQUS. The finite element model used to simulate the sandwich composite is shown in Figure 3.9, where the distance between the rigid supports was 228.6 mm (9"), and the impactor span was 150 mm applied at the center line and the same width as the beam. Only half the geometry was modeled, taking advantage of symmetry. The skins were rigidly tied to the foam core while the interface of impactor and rigid support to the beam was modeled frictionless.

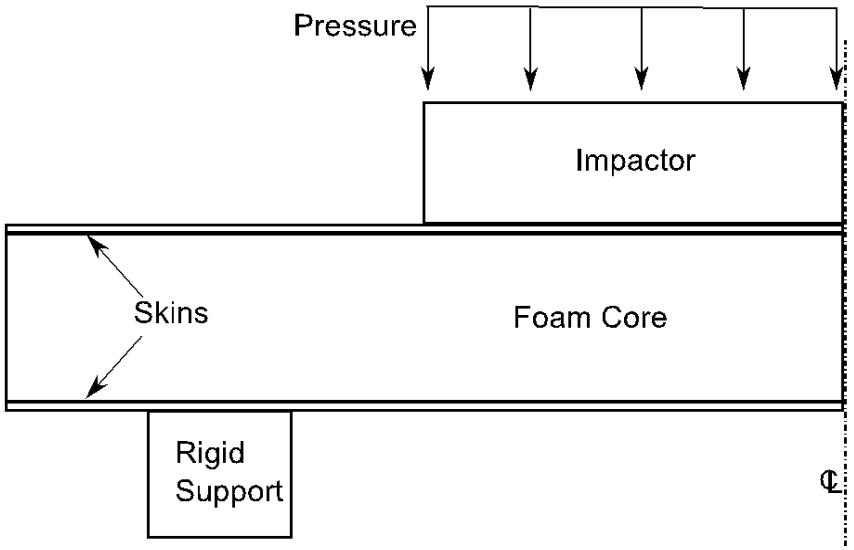

Figure 3.9: FEA geometry of the sandwich structure simulating hull slamming test condition

The pressure distribution from finite element analysis (FEA) under the impactors for various elastic moduli is shown in Figure 3.10. The top surface of the impactor was subject to uniform vertical displacement. The results demonstrate the softer impactor (Young modulus = 10 MPa) maintains contact with the sample, whereas the stiffer impactor (10 GPa) separated leading to large stress concentrations. In order to mechanically replicate the slamming load (fluid-structure coupling) magnitude without introducing large stress concentrations, a soft rubber pulse shaper was chosen with a loading span of 150 mm (6”). This material choice allowed the force to be transmitted smoothly without causing indention damage (Figure 3.8). The pressure distribution for several loading forces on a soft impactor (Young modulus = 10 MPa) is shown in Figure 3.11 to demonstration that the loading pressure is maintained during the simulated slamming event. There is a small stress concentration near the impactor edge tapering off toward the centerline.

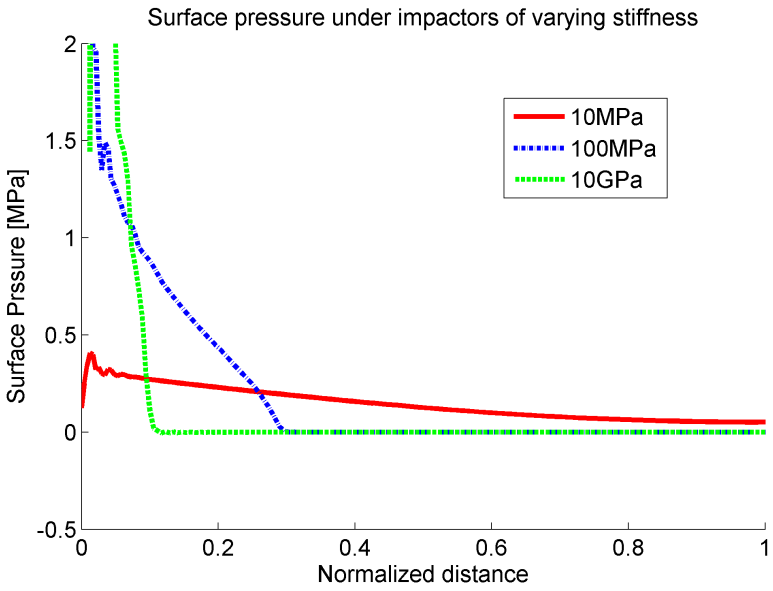

Figure 3.10: Surface pressure per unit width under impactors of varying stiffness with prescribed top vertical displacement of 2.5 mm. Plotted against normalized distance from edge to centerline of rectangular impactor

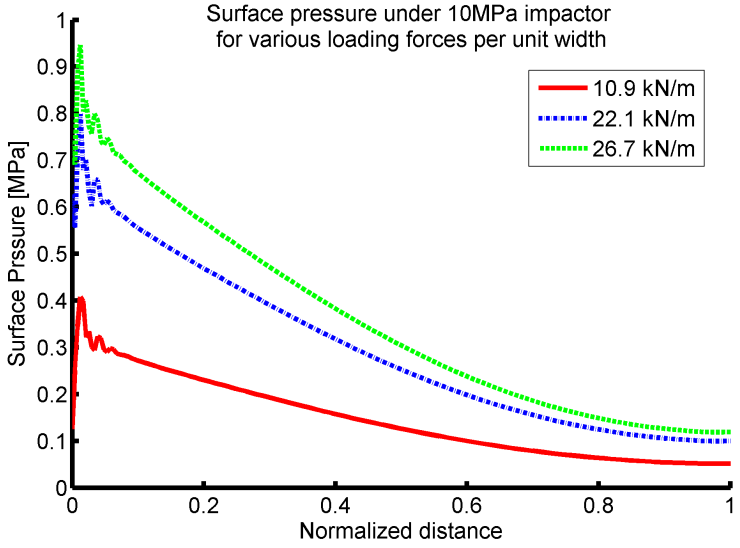

Figure 3.11: Surface pressure per unit width under rubber impactor with elastic modulus of 10 MPa for several loading forces. Distance is normalized with the half-length of rectangular impactor

Experimental pressure forces utilizing the MMS were determined from measured force assuming uniform distribution. A characteristic pressure over time plot is shown in Figure 3.12 utilizing the measured force and constant contact area. The peak force was approximately 4000 N.

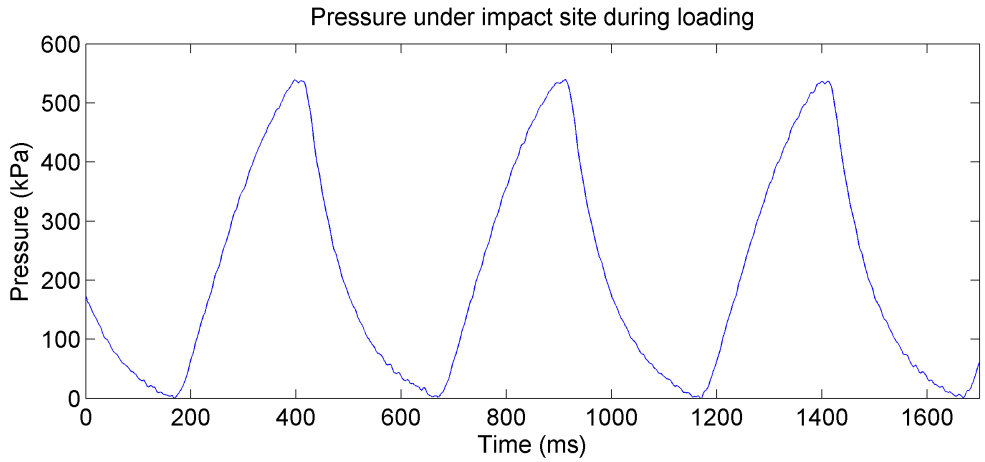

Figure 3.12: Pressure under rubber impactor inferred from experimentally measured force history over impact area 0.0077 m^2 onto a sandwich composite beam

In this case, the peak pressure was 537 kPa with an average value of 228 kPa. The duration of each cycle was 500 ms and the total applied impulse per cycle was 885 N-s. Taking the average pressure as the representative loading measure, a comparable slamming condition can be determined by finding the appropriate wedge velocity and slamming angle. The pressure during wedge slamming events has been calculated in previous wedge slamming studies [11] and nondimensionalized into the coefficient of pressure by dividing the pressure by the dynamic pressure ($0.5\ \rho V^2$) where ρ is the density of water and V is the wedge velocity. For a given pressure, the required velocity and coefficient of pressure can be determined from the definition of coefficient of pressure. The family of required velocity and pressure are presented in Figure 3.13 for a number of desired pressures.

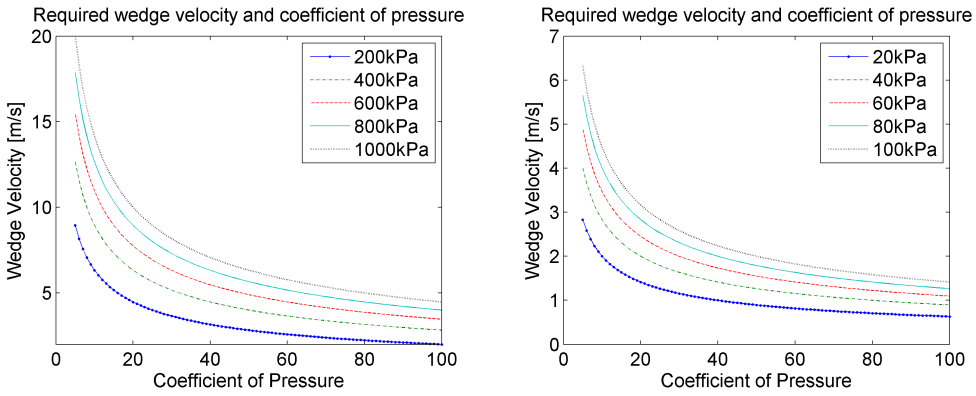

Figure 3.13: Wedge velocity and coefficient of pressure (C_p) required for obtaining particular pressures based on the wedge water entry problem. $C_p = p/0.5\ \rho V^2$

In a slamming event, there is a short duration high initial pressure pulse followed by a rapid decay to a long duration pulse with significant residual pressure. Utilizing results from previous wedge slamming studies [11], a relationship between the slamming angle and residual pressure coefficient can be ascertained and is shown in Figure 3.14. For the example presented in Figure 3.12, the desired pressure of 228 kPa lies slightly above the bottom curve in Figure 3.13 and, assuming a coefficient of pressure of 20, would require a wedge velocity of 4.7 m/s. In order to obtain a residual coefficient of pressure of 20, the required wedge angle is 10 degrees, as shown in Figure 3.14.

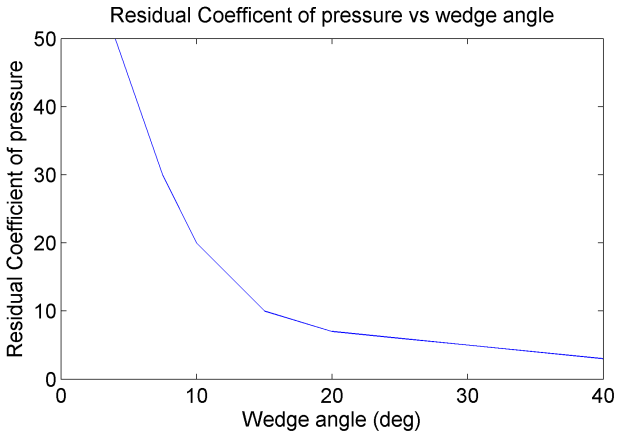

Figure 3.14: Residual pressure coefficient trailing after peak pressure pulse during a wedge slamming event. The computation is based on results from [11]

The pressure pulse was simulated mechanically using a soft impactor to maintain contact with the surface. The impulsive high pressure peak is ignored as the majority of the panel response is thought to come from the long duration trailing pressure pulse. The impulsive pressure would become more important when the duration of loading is on the order of the natural frequency of the panel. In that case, the resulting elastic vibrations could influence the fluid structure interaction and peak stress in the panel. But the cases of interest were for stiff panels where the loading state has insignificant hydroelastic effects.

3.2.2 Sandwich structure and expected failure modes

Steeves and Fleck's [81] failure mode analysis for three bending of sandwich composites is used to predict the anticipated failure modes. A more detailed description of their failure mode analysis was presented previously in Section 1.3.2. A carbon fiber PVC foam core sandwich composite geometry (similar to those utilized in ship hulls) was selected for the slamming test and manufactured by Marine Design and Composites, Owings, Maryland. The carbon fiber sandwich structure was constructed of 50-mm-thick Divinycell H100 foam core and 2-mm-thick carbon fiber (Thornel T300 3K) epoxy face sheets. The epoxy system utilized in the face sheet manufacture and attachment to the foam core was Derakane 8084. The strength properties for the components in the composite material are presented in Table 3.1. The sandwich composite panels were cut into 300-mm-long, 50-mm-wide beams for testing. The strength for the quasi-isotropic carbon fiber face sheets [120] is also presented in Table 3.1.

Table 3.1: Strength properties of sandwich structure components

Material	Strength	Young's Modulus
Carbon fiber: Thornel T300 3K 309NT[a]	Tensile: 3.8 GPa (550Ksi)	231 GPa (33Msi)
Epoxy system: Derakane 8084[b]	Tensile: 76 MPa (11Ksi)	2.9 GPa (0.42 Msi)
Foam core: Divinycell H100[c]	Tensile: 3.5 MPa Shear: 1.6 MPa	Tensile: 130 MPa Shear: 35 MPa
Facesheet: 60% VF Quasi-isotropic[d]	Tensile: 500 MPa	50 GPa

Source: [a][121], [b][122], [c][82], [d][123]

Using Steeves and Flecks' analysis described in Chapter 1, the expected failure mode for this structure and geometry under three-point bending is indentation, but it also lies near the transition to core shear failure. This proximity to core shear failure and the actual distributed loading indicate that the failure mode could be either indentation or core shear failure. Similar sample dimensions were investigated by Carlsson [76] in their study on foam core life prediction under flexural loading in sandwich composites under three-point bending. The damage mode observed in Carlsson's work was an initial delamination crack at the foam core skin interface, which propagated until a core shear kink crack occurred, extending the crack to the opposite face sheet. Similar failure progression was expected in the present work.

The applicability of the quasi-static assumption requires that the ratio of loading period to natural frequency, *R* ratio, be larger than 5 [16]. The natural period for the beam under consideration is given by (3.1) below with boundary condition factor $\mu_{NP} = \pi$ as the beam was simply supported. The beam span, *b*, was 0.228 m and the width, *w*, was 50 mm. Utilizing the material properties from Table 3.1, the bending stiffness, *D*, for the sandwich beam was 3047 N-m given by (3.2) using the tabulated material properties. Subscripts *c* and *f* indicate core and face sheets, respectively. The resulting natural period

is approximately 3.5 ms and, provided the loading period is longer than 17.5 ms, the resulting *R* ratio would indicate that a quasi-static assumption is valid. Since the loading event of interest is the long duration pressure with respect to the natural frequency of the panel, the loading can be assumed quasi-static.

$$T_{NP} = \frac{2\pi}{{\mu_{NP}}^2}\sqrt{\frac{(m)b^3}{D}} \tag{3.1}$$

$$D = EI_{sand} = 2E_f\left(\frac{wt_f^3}{12} + \frac{t_f w d^2}{4}\right) + E_c\frac{wt_c^3}{12} \tag{3.2}$$

3.2.3 Thermoelastic stress analysis (TSA) on foam core

3.2.3.1 H100 calibration

In order to apply the TSA method on foam core sandwich composite beams, the thermoelastic response of the foam core must first be measured and then calibrated. A series of calibration experiments on H100 foam blocks in compression were performed at various stress variation levels. The blocks of H100 foam were machine milled to ensure parallel edges and then cyclically compressed in the servo hydraulic testing machine (MTS). The thermal response for each stress level was recorded via an infrared camera and the temperature variation amplitude was determined as outlined in Chapter 2. Additionally, the effect of permanent strain on the thermal response of H100 foam was investigated. Samples of H100 foam were pre-compacted by various amounts and subject to uniaxial cyclical elastic loading. The corresponding thermal response for each compaction level was measured and the resulting thermoelastic sensitivity is presented in Table 3.2. The density is reported as initial before the samples were compacted and the resulting density during testing.

Table 3.2: Sample dimensions, mass, density, and observed thermoelastic sensitivity of Divinycell H100 foam core

Sample number	Dimensions (mm)	Mass (g)	Initial Density (kg/m^3)	Tested Density (kg/m^3)	Thermoelastic Sensitivity ($^oC/MPa$)
S5	29.7x40.2x52.9	6.34	102	102	0.0733
S7	39.3x45.6x43.6	8.14	96.0	104	0.0348
S9	32.0x47.3x51.1	9.16	95.9	117	0.0222

The relationship between stress variation and temperature variation for each compaction level is shown in Figure 3.15. The thermoelastic response remained linear throughout the elastic range for all the compaction levels that were examined. The resulting trend shows the thermoelastic sensitivity diminishes as the compaction or permanent strain level increases. The nonzero offset is common among the samples and represents the noise amplitude. Provided the foam core of a structure is not subject to permanent deformation, the stress field can be determined using the zero compaction thermoelastic sensitivity. By tracking the deformation field of the foam core with DIC, regions with permanent strain or lack thereof could then utilize the appropriate thermoelastic sensitivity factor.

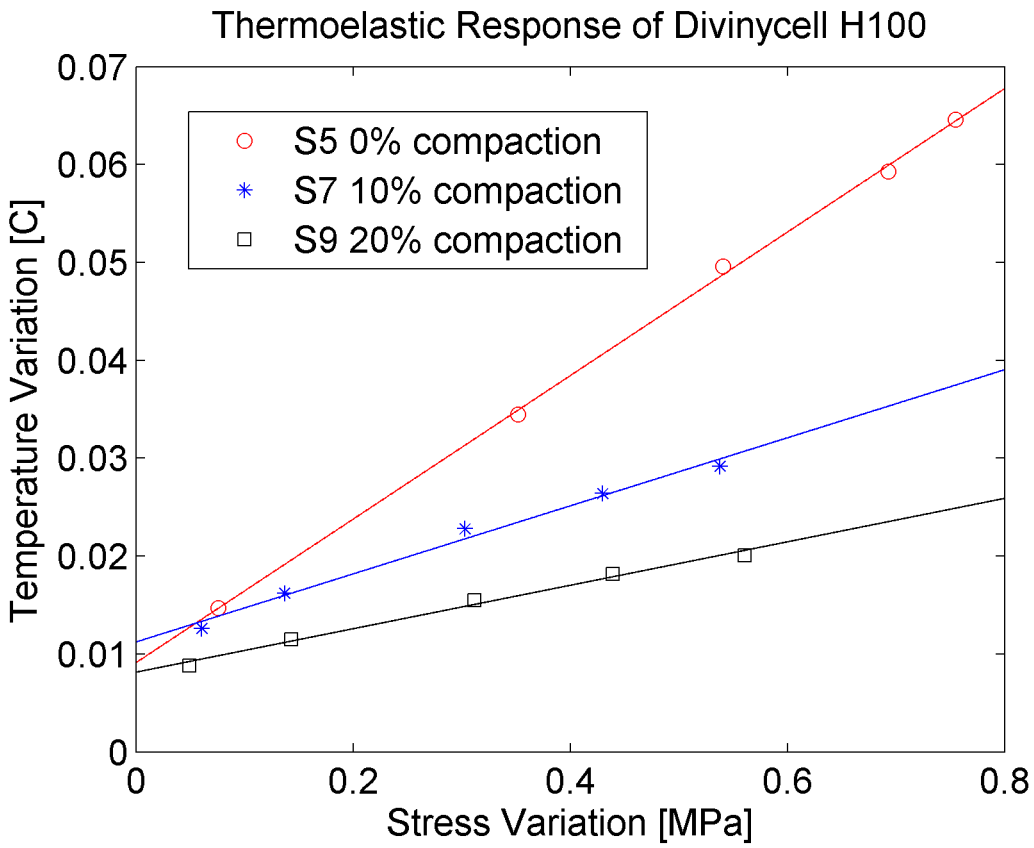

Figure 3.15: Thermoelastic response of Divinycell H100 for various compaction levels

3.2.3.2 Application of combined TSA-DIC on foam core

The ability to apply TSA under non-uniform stress state was performed utilizing a three point bend setup as shown in Figure 3.16. A sandwich composite was cyclically loaded under three-point bending center loaded with a span (L) of 187 mm under displacement control with 2mm amplitude at 5 Hertz of the center pin. The thermal response was recorded in the region below the center pin, which is shown as a dashed box (55 x 105 mm) in Figure 3.16. An example raw thermal image is presented in Figure 3.17a, also visible is the speckle pattern used for DIC correction. The time varying temperature field was recorded and processed as described in Chapter 2 for a TSA-DIC analysis. The applied speckle pattern can also be removed by a spot removal process

where the speckle locations are determined via a high-pass spatial filter. The thermal information within each speckle is replaced by an interpolation from the boundary of each spot. An example of the spot removal effect is presented in Figure 3.17b, showing a continuous temperature field within the foam core of a sandwich composite beam.

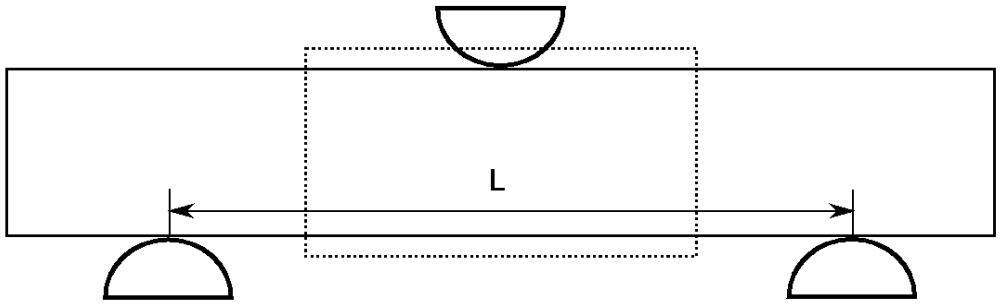

Figure 3.16 Schematic of a three-point bend configuration with observation region for combined TSA-DIC indicated by the dashed box

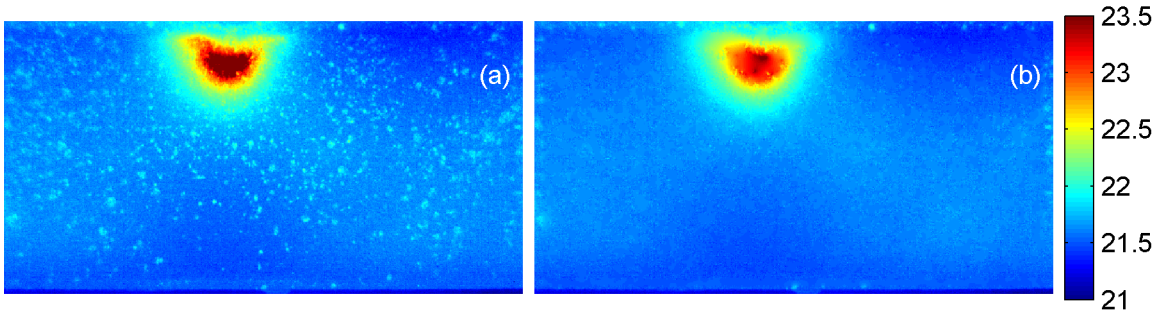

Figure 3.17: (a) Raw infrared (IR) image of foam core temperature (^{o}C) in the region under the center loading pin, (b) After spot removal. Field of view: 55 x 105 mm (5.4 pixels per mm)

A DIC analysis on the time varying thermal recording and the resulting pixel displacement and strain variation amplitude are presented in Figure 3.18. Under a bending loading cycle a significant pixel motion can be expected while still remaining elastic, thus distortion correction before a TSA analysis is necessary to remove spurious thermal variations. In order to reduce the noise in the DIC results, the average deformation and strain amplitudes at the loading frequency were determined over several

of loading cycles by utilizing the same FFT method as presented for thermal variation measurement.

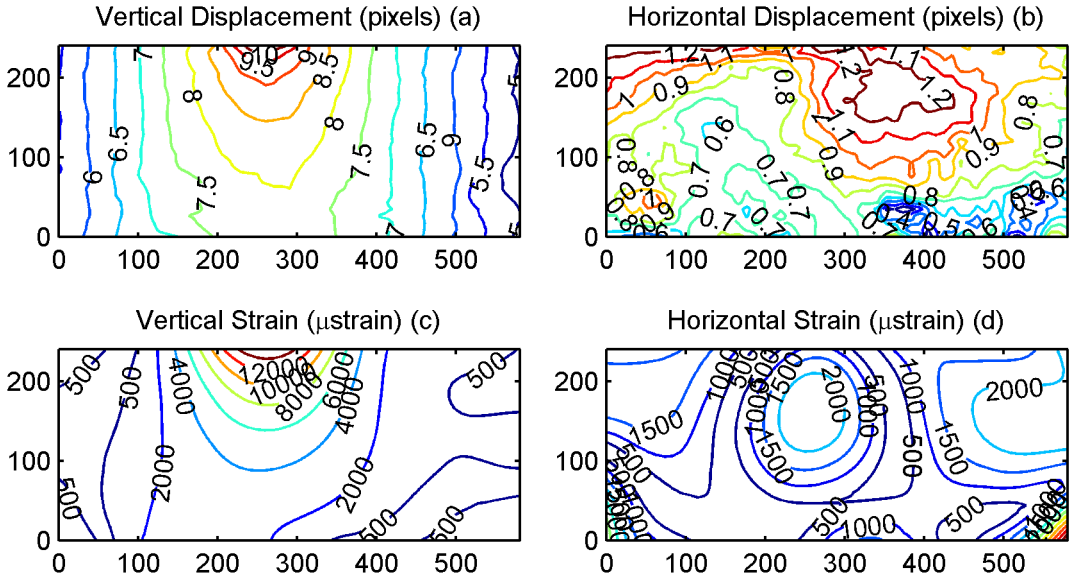

Figure 3.18: DIC displacement and strain field variation amplitude; (a) vertical and (b) horizontal pixel motion; (c) vertical and (d) horizontal strain components. Field of view: 44.4 x 107.4 mm (5.4 pixels per mm)

The computed deformation field for each frame, from DIC, was used to stabilize the thermal movie such that each pixel represented a particular material point in all frames. This stabilization improves the resolution of TSA results while reducing motion induced errors near large thermal gradients. The combined TSA-DIC result, Figure 3.19a, is compared to the TSA result without DIC correction, Figure 3.19b, demonstrating significant thermal variation errors under the loading pin when not accounting for sample motion.

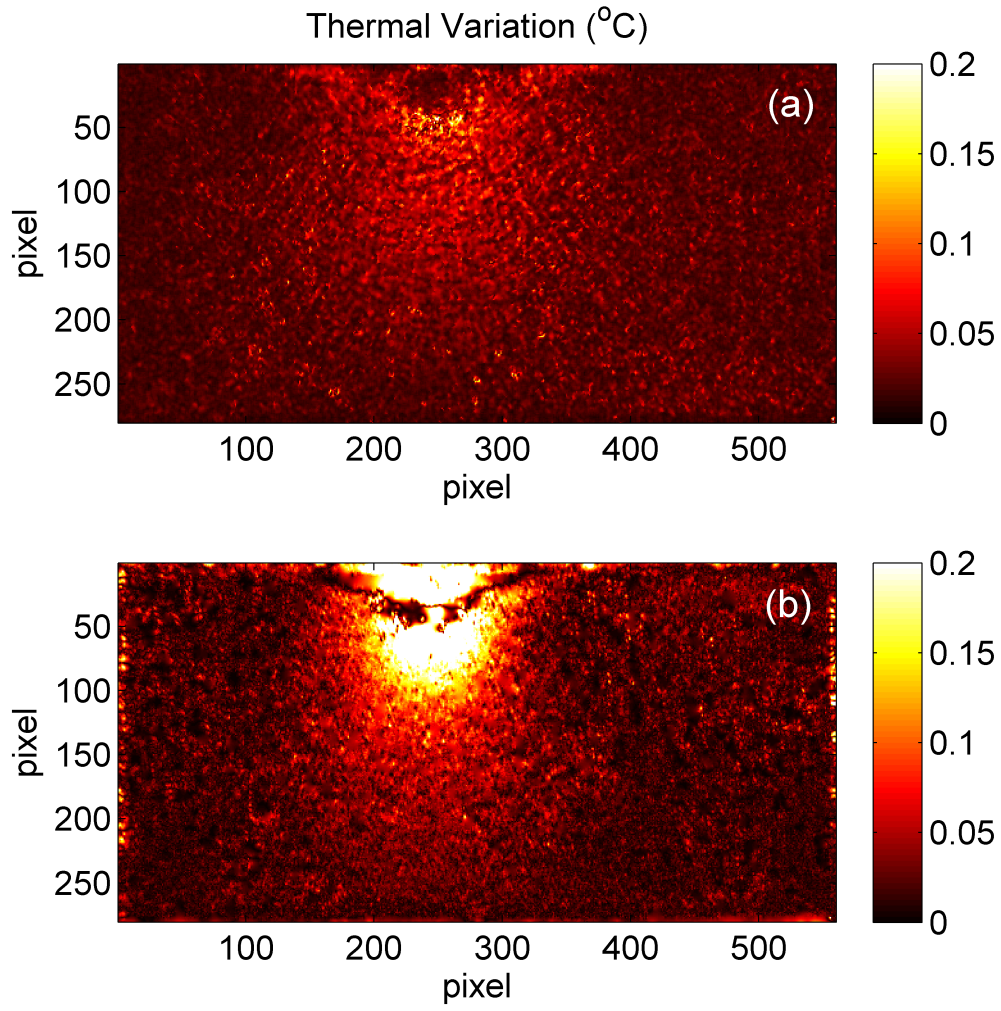

Figure 3.19: TSA results demonstrating the effect of DIC correction on sandwich composite beam under three-point bending. (a) Temperature variation (°C) in foam core with DIC correction and (b) without DIC correction. Field of view: 44.4 x 107.4 mm (5.4 pixels per mm)

Variations in the sum of principal stress, Figure 3.21b, were found utilizing the calibration for non-compacted H100 foam from Table 3.2. A stress field from DIC results, Figure 3.21c, was determined by the product of the amplitude of the sum of principal strains and the elastic modulus of H100. These stress fields have similar magnitudes and distributions with discrepancies likely due to the nature of DIC which requires averaging to determine the displacement field which then must be differentiated

to determine the strain field which requires a smoothing function to further reduce noise. A detailed ABAQUS finite element model, Figure 3.20, was loaded with rigid circular pins under the same experimentally applied center displacement. The model includes an epoxy filled groove cut into the foam core during manufacturing along the center line of the beam. The resulting sum of principal stress field from FEA, Figure 3.21a, has better agreement with the TSA results than to the DIC results. The coordinate system for these stress fields from FEA, TSA, and DIC originated at the center and edge of the epoxy intrusion. The stress along horizontal and vertical lines from the origin is presented in Figure 3.22. The TSA-DIC method obtains the stress field directly without differentiating or smoothing thus giving higher resolution and preserving finer details within the foam core such as the microstructure and heterogeneities. Away from the origin, all three methods produce similar results but near the epoxy region the stress is overestimated in the FEA possibly due to yielding. The stresses in the epoxy region from TSA and DIC are incorrect as the H100 foam sensitivity and elastic modulus were utilized in the entire region.

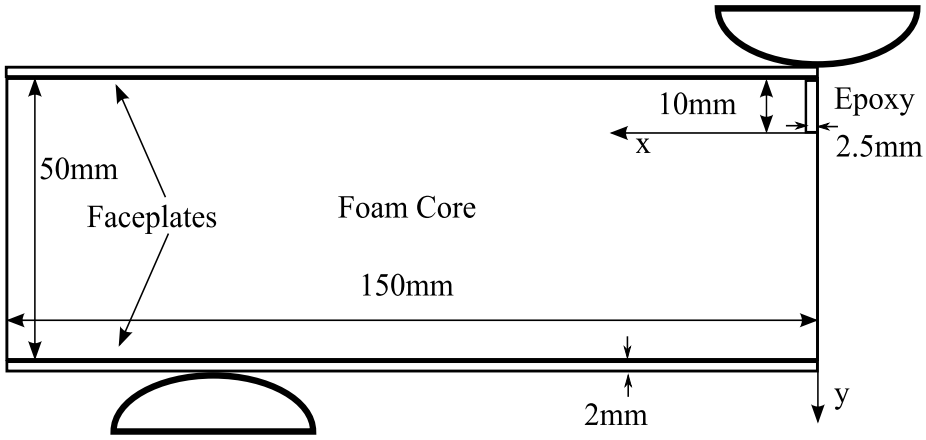

Figure 3.20: Detailed half model of three point bending test on sandwich composite beam. Center and end of epoxy filled groove cut into foam during manufacturing as origin of coordinate system

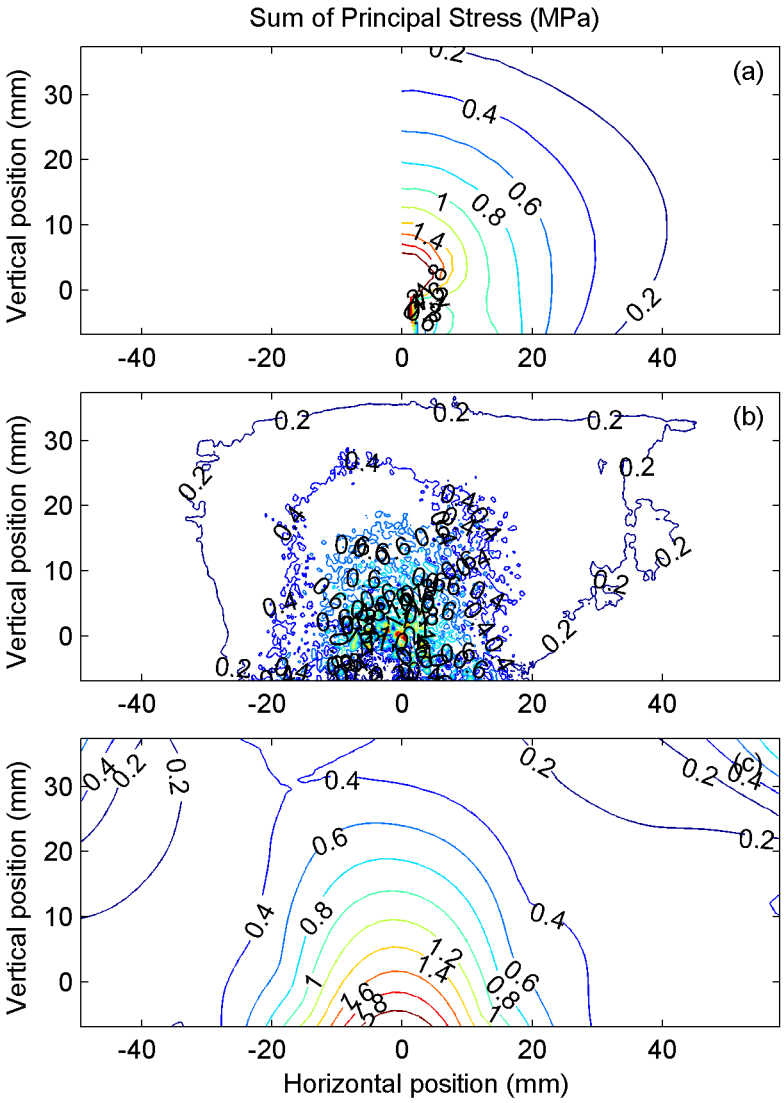

Figure 3.21: Sum of Principle Stresses (MPa) from (a) FEA model; (b) TSA-DIC analysis using thermoelastic calibration factor for H100 foam; (c) DIC strain field variation amplitude multiplied by the Young's modulus for H100 foam

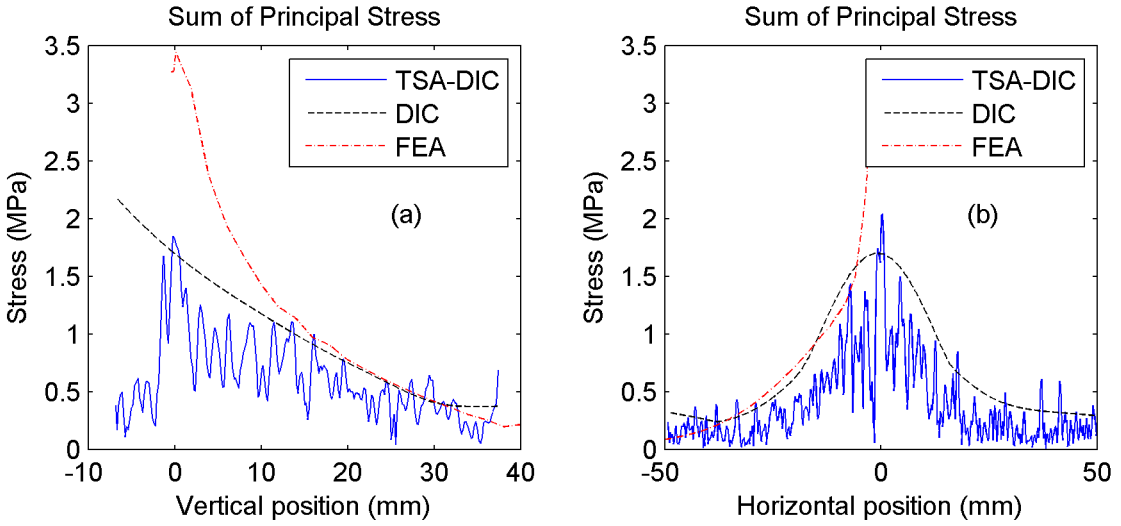

Figure 3.22: Comparison of sum of principal stress from TSA, DIC and FEA along (a) vertical centerline of beam and (b) horizontal line at edge of epoxy intrusion into foam core

3.3 TSA-DIC under hull slamming loading

In order to study the effects of repeated hull slamming events on sandwich composite structures, a series of long duration cyclic slamming experiments at various intensities and constant frequency were performed using the mechanical slamming simulator (MSS) described in Section 3.1. The testing sequence first sought to demonstrate that slamming loading would elicit a measurable thermoelastic response. Repeatedly measuring the stress field during each loading case allowed the stress evolution and damage initiation to be analyzed. Sandwich composite beams described in Section 3.2.2, 50-mm-wide and 300-mm-long, were chosen so that the stress field could be approximated as uniform through the width. The beams were simply supported with a span of 228.6 mm (9”) with a symmetrically distributed load 150 mm wide about the center line applied using a 50-mm-thick rubber impactor, Figure 3.23. The samples were prepared with an initial

coating of Krylon 1602 ultra-flat black spray paint providing a uniform high emissivity base followed by a low emissivity speckle pattern. The emissivity contrast provided an inherent temperature contrast necessary for a DIC analysis.

A high sensitivity IR camera (FLIR SC6000) was positioned directly above the samples on a tripod such that the camera axis was normal to the foam surface. Additionally, a 350 Ω EA series strain gauge from Micro-Measurements was mounted to the sandwich composite face sheet opposite the loading and aligned along the beam length axis. The applied force during the each loading cycle was measured using a factory calibrated 33.3 kN (7.5 kip) force transducer from Transducers, Inc. Both the strain gauge and force transducer signals were recorded via a LabView program that also controlled the pneumatic cylinder in the MMS.

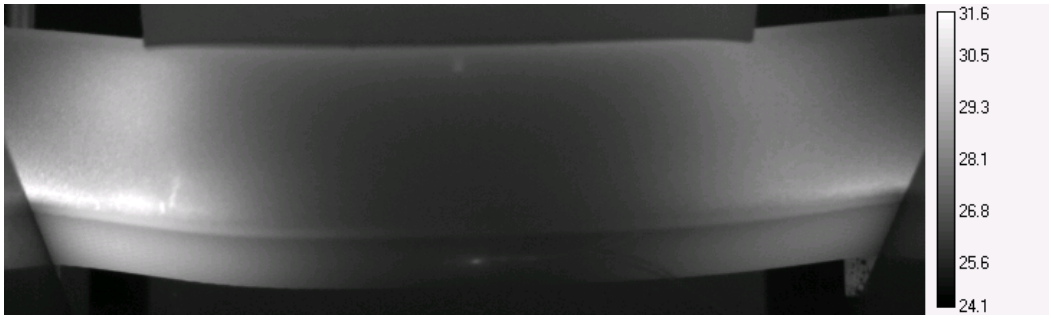

Figure 3.23: Temperature [^{o}C], in a sandwich composite under slamming loading as visualized using thermal IR imaging

The prepared beam samples were mounted in the MMS and the desired peak force was set via the high flow regulators. A cyclic mechanical load at 2 Hz was applied by the solenoid valve on the pneumatic cylinder. The samples were continually loaded at this frequency for the durations indicated in Table 3.3 and the temperature was recorded every 5 minutes with the IR camera at 20 frames per second for 10 seconds. The stress

variation was assumed to be constant during each of the durations of IR recording. Thus, evaluating stress in the foam core was determined via thermoelastic stress analysis averaging over 20 loading cycles. The strain and force transducer signals were continuously recorded during the entire testing cycle. The ambient temperature was recorded over a 7-day period and found to have a mean of 296 Kelvin and vary less than $1^{o}C$ leading to possible TSA errors less than $1/296\ ^{o}C$.

3.3.1 Results from Combined TSA-DIC

The composite sandwich beams were loaded at various loading amplitudes for a number of cycles, as enumerated in Table 3.3 for a set of loading conditions. During each case, a thermal recording was taken every five minutes. An example raw temperature field is shown in Figure 3.24 with the impactor visible in the top center of frame. Each thermal recording was analyzed to determine the stress state of the beam at that loading amplitude and current damage progression. The combined TSA-DIC method was applied to each thermal recording correcting for distortion due to loading and producing a full field in situ state of stress image. The measured temperature variation in the foam core was then converted into stress, utilizing the thermoelastic calibration for H100 foam from Section 3.2.3.1.

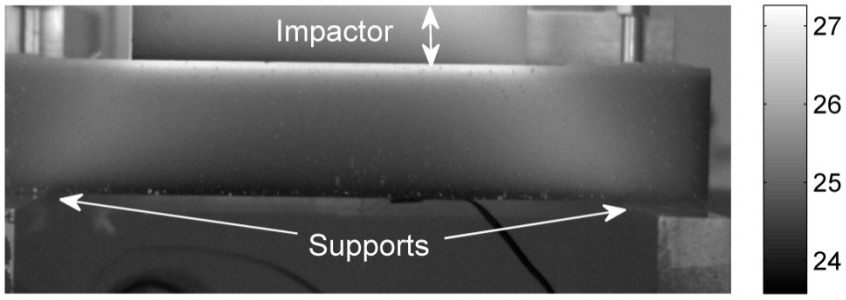

Figure 3.24: Example of raw temperature field [^{o}C] during a slamming test

Table 3.3: Mechanical slamming simulator test case parameters

Case	Peak Force [N]	Average Force [N]	Average Pressure [kPa]	Impulse Per Cycle [N-S]	μstrain Variation	Loading Frequency	Number of Cycles
1	2741	1039	134	520	630	2Hz	260
2	2784	1098	142	549	632	2Hz	340
3	2851	1144	148	572	658	2Hz	380
4	3672	1524	197	762	856	2Hz	680
5	3906	1661	215	830	901	2Hz	620
6	4185	1771	229	885	965	2Hz	2540
7	4106	1647	213	824	945	2Hz	18000
8	4692	1712	221	856	1122	2Hz	80000

Following the procedure presented in the Section 3.2.1 on slamming pulse replication using the MSS, comparable slamming conditions for the cases listed in Table 3.3 were determined. The corresponding wedge slamming conditions for the various cases are presented in Table 3.4, for an assumed wedge angle of 10^{o} which has a coefficient of residual pressure of 20.

Table 3.4: Comparable wedge slamming conditions

Case	Average Pressure [kPa]	Wedge Angle	Wedge Velocity (m/s)
1	134	10	3.66
2	142	10	3.77
3	148	10	3.85
4	197	10	4.44
5	215	10	4.63
6	229	10	4.79
7	213	10	4.62
8	221	10	4.70

3.3.1.1 DIC correction under slamming load

For each recording during the various loading conditions, the raw thermal images were filtered and converted into 16-bit TIFF images which were then analyzed with a commercial DIC code VIC-2D by Correlated Solutions. The output displacements from VIC-2D were then imported into Matlab where a custom script corrected each raw thermal image pixel by pixel for the measured displacement. The final result was an image sequence where each pixel represented the temperature at a single material point. An example of the DIC correction effect is shown in Figure 3.25, where the temperature variation with and without motion correction is demonstrated for thermal variation maps of the right half of the sandwich composite beam during Case #8 in Table 3.3. In Figure 3.25a, the temperature variation with deformation correction shows stress concentrated near the support on the bottom right and distributed under the impactor in the top center. In Figure 3.25b, the temperature variation without correction captures the stress concentration near the support but includes a spurious variation in the center region indicated by the arrow. In regions with little motion, as near the support, the difference in thermal variation with DIC correction was minimal but was quite significant on the order of 0.1^{o}C, in regions with deformation on the order of several pixels.

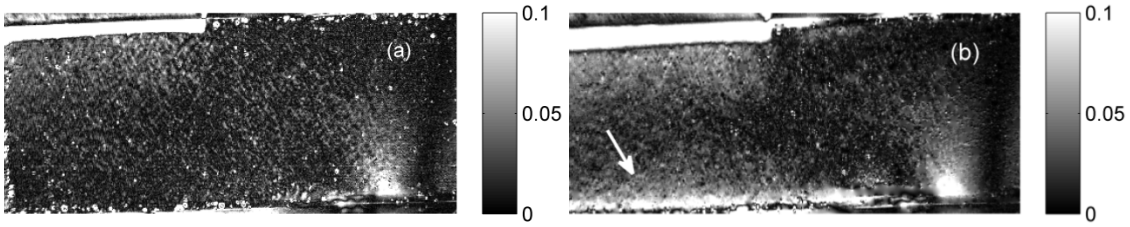

Figure 3.25: TSA thermal variation (^{o}C) near delamination crack in sandwich composite under slamming loading (a) with DIC correction, (b) without DIC correction, arrow indicating key difference

3.3.1.2 FEA slamming simulator model

A finite element model was developed in the ABAQUS FEA software simulating the mechanical slamming geometry and was used to predict the stress and displacement fields under various static loads. Since the slamming events of interest were much longer than the natural period of the beams, the slamming event can be considered to be quasi-static and the static analysis is justified. The material models were assumed to be linear elastic as the deformations were small. The predicted stress field can be compared against the measured TSA stress field for both magnitude and distribution. The predicted displacement field can also be compared to the measured displacement from DIC. In Figure 3.26, the sum of principal stresses, which is the parameter measured via TSA, is presented for the simulated case were the top of the soft rubber impactor is displaced 3.5 mm. Comparing the amplitude of the stress field to the temperature variation field in Figure 3.25, one can see similar stress distributions within the foam core near the supports. The stress field in the center span has some discrepancy likely due to the more complicated nature of the foam than the simple homogeneous, isotropic, and linear elastic idealization used to describe its material behavior. The TSA result does capture the compression-tension transition near the center of the core and some of the tensile stress near the bottom face sheet, but at a smaller magnitude than the finite element model would predict.

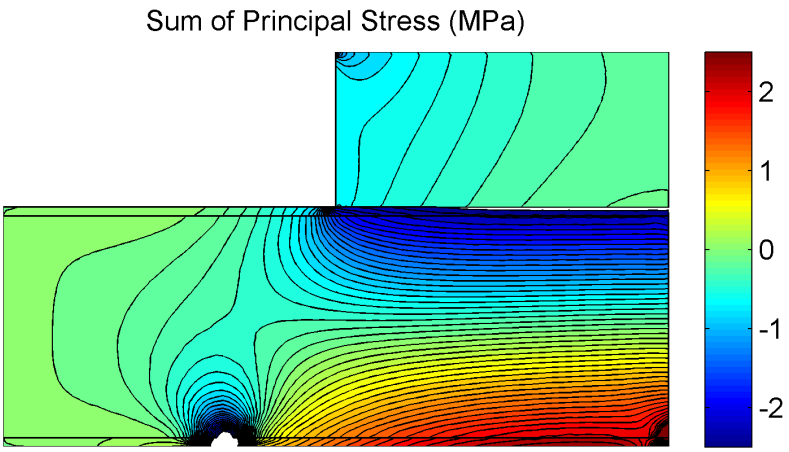

Figure 3.26: Sum of principal stresses [MPa] in sandwich composite under 3.5 mm prescribed top displacement on a rubber impactor. The composite beam is composed of a 50 mm H100 foam core and two 2 mm CFRP faceplates

The FEA simulated displacement field, Figure 3.27, can be compared against the measured DIC field, Figure 3.28. The uniform displacement under the impactor is captured, as well as the transition to zero displacement at the supports. The displacement resolution of DIC is not as high as the stress field from TSA. The resolution of the TSA stress field is higher since the data is not subject to a smoothing function and the inherent complexity of the foam core structure can be captured.

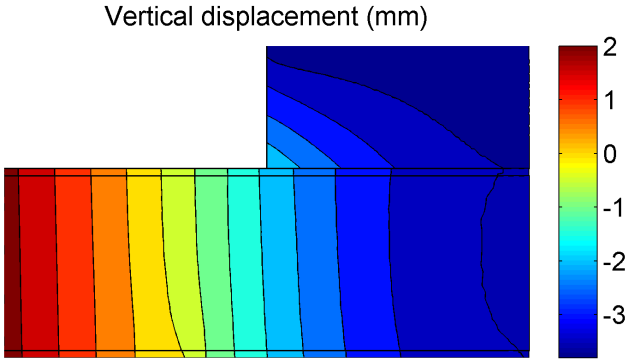

Figure 3.27: Vertical displacement (mm) plotted on reference geometry from FEA analysis with prescribed 3.5 mm top displacement of the impactor

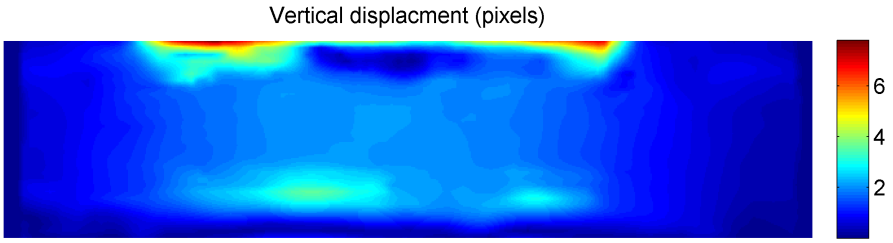

Figure 3.28: Measured vertical displacement variation (pixels) under slamming loads via DIC of the entire span. 1 mm = 2.6 pixels

3.3.2 Damage Detection, Initiation, and Growth

As discussed in Section 1.3.2 there are various methods for detecting and measuring damage in sandwich composite materials. For example, internal damage can be determined nondestructively utilizing X-ray radiography, where an appropriate liquid penetrant is applied to the surface of the laminate and can expose the extent of damage within the laminate where the penetrant could reach [124]. The composite could also be destructively analyzed by sectioning at various locations after an impact to visually determine the interior damage. Less invasive methods such as residual strength are qualitative in nature as the exact location of damage remains unknown. Nondestructive testing is required when the sample would be continually loaded and analyzed for damage progression. Ultrasonic and thermal imaging methods are good examples of non-destructive testing [100, 124]. Flash thermal heating or pulse thermography can locate surface or subsurface damage. The location of damage is revealed as a hot region where the pulsed heat wave due to thermal propagation was impeded and is presented as unit less scaled contrast. A benefit of TSA over ultrasonic testing is that the amplitude of stress field is determined in addition to the damage location. TSA provides a method to

both locate damage [91, 93, 125] and determine the severity by measuring the actual stress state.

3.3.2.1 Damage modes in sandwich composite under slamming load

Mechanical loading of sandwich composites can result in a number of damage and failure modes. One common failure mode is delamination between the soft core and stiff face sheet. The measured stress field in a sandwich composite beam under mechanically simulated slamming with a growing delamination crack is shown in Figure 3.29. The resulting thermal variation after various numbers of cycles, for loading state Case #8 from Table 3.3, demonstrates the delamination crack is growing and altering the stress field within the foam core. After the indicated number of cycles, a thermal recording was taken and the raw temperature fields were corrected for motion using DIC as described in Section 3.3.1.1. The variation in temperature at the loading frequency for each pixel was determined via TSA analysis. After motion correction, the speckle pattern produces spots with temperature variations that differ from the surrounding material. To provide a more accurate temperature map, the speckles were located and a mask was created to remove the measured temperature variation at those pixel locations. The newly formed ‘holes’ in the TSA image data were filled by interpolation from the valid temperature variation boundary of each hole.

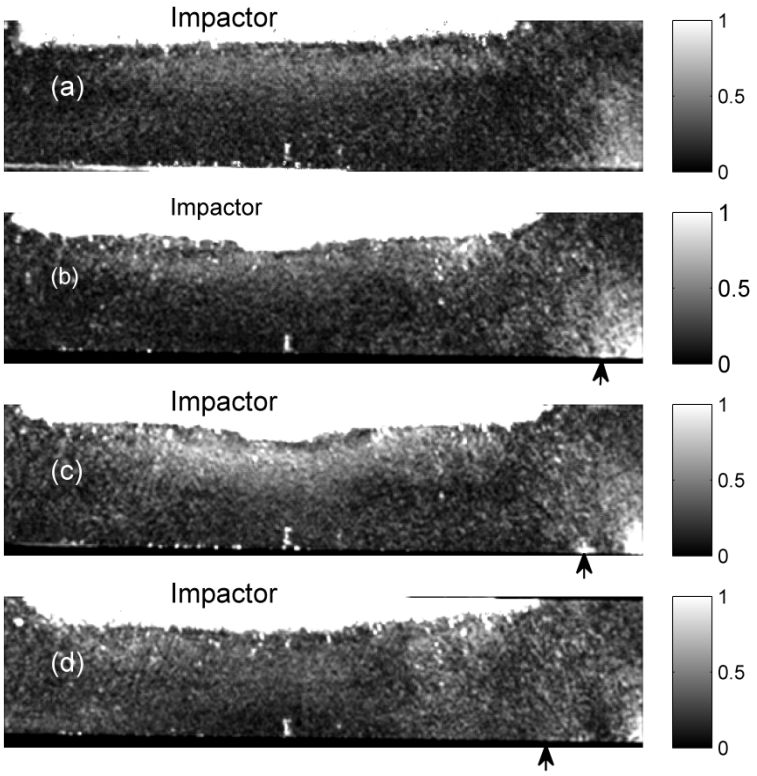

Figure 3.29: Stress variation [MPa] in foam core during Case #8 from Table 3.3 at (a) 24000, (b) 48000, (c) 60000, (d) 72000 cycles. Sample supported at bottom corners of image and loaded at top center; arrows indicate delamination extent

The temperature variation in the foam core after the given number of cycles in Figure 3.29, demonstrates the ability to observe the evolving stress field. The stress field can be determined utilizing the appropriate linear calibration factor from Section 3.2.3.1. As each recording covers 10 seconds duration, it is assumed the stress field does not change during each thermal recording and any changes occur over a longer time scale. The average temperature in the foam core during each of these recordings, Figure 3.30, shows only a 0.6^{o}C rise over the testing sequence and the mean temperature does not change during each recording. This slow evolution is demonstrated in Figure 3.29, as the delamination crack near the bottom right support first appears as a separate stress concentration after 48,000 cycles. This secondary stress concentration continues to

separate from primary support stress concentration in the 60,000 cycle image. A stress free region above the delamination crack is visible in the 72,000 cycle temperature variation image. The large temperature variation at the top and center of each frame was due to the impactor coming in and out of view and should be disregarded.

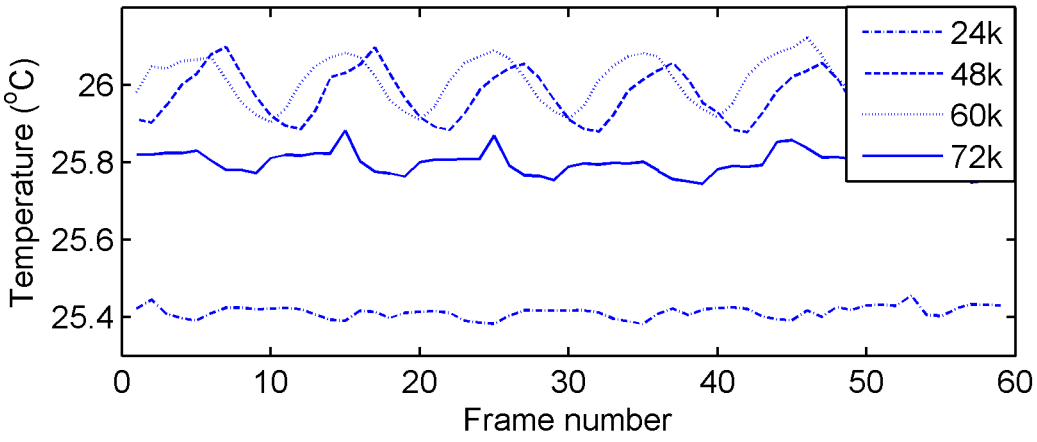

Figure 3.30: Average temperature during thermal recordings at various numbers of loading cycles

The effect of DIC correction on this delamination crack was shown in Figure 3.25 showing the right half of the beam from Case #8 in Table 3.3. The measured deformation field via DIC for this case, Figure 3.31, shows the center span was subject to vertical motion of up to 6 pixels. In regions with little motion as near the support, the difference in thermal variation after distortion correction was minimal, while regions with deformation on the order of several pixels.

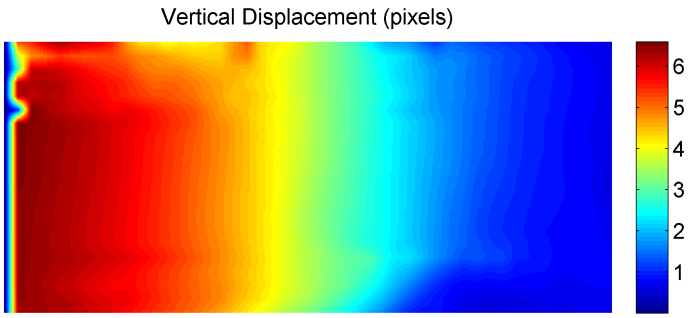

Figure 3.31: Vertical displacement variation (pixels) during slamming loading for Case #8 in Table 3.3 with a delamination crack

3.3.2.2 Damage initiation and growth

A series of long duration mechanical slamming cases were performed with the MMS. The aim of the series was to probe for evidence of damage growth and a failure threshold for the chosen sandwich composite beams described in Section 3.2.2. During each case, a 10 second thermal recording was taken every 5 minutes to observe evolution of the thermal field and thermal fluctuations. A strain gage mounted on the side opposite loading gave a measure of the deformation of the sample. The force variation for each case was set with the pressure regulators in the MMS device and cycled once a second. The resulting force variation, mean applied force, impulse per cycle, and strain variation are also presented in Table 3.5. Case #1 and 2 were performed for 3 hours resulting in 10800 cycles each, but the cyclic loads of 2146 and 4416 N, respectively, were not large enough to sustain obvious damage. In Case #3, the 3 hour test with cyclic loading of 6605 N was cut short when the beam failed completely after 4440 cycles. Another indicator of damage for Case #3, was that the strain variation per cycle gradually increased by 27% up until failure. In Case #4, a larger cyclic load of 6823 N was applied and sustained for 50 minutes or 3000 cycles. The beam sustained initial delamination damage and a gradual

increase in strain variation per cycle of 15%. The results indicate the failure threshold for this sandwich composite beam begins when the force variation is larger than a force between 4416 (Case #2) and 6605 N (Case #3). Utilizing the average force for Case #2 and #3 as the representative slamming measure, the average pressure applied was 193 kPa and 394 kPa, respectively. The corresponding hull slamming velocity for these cases can be determined as function of residual coefficient of pressure (see Figure 3.13). For an assumed deadrise angle of 10^{o}, the coefficient of pressure for the long duration residual pulse is 20 (see Figure 3.14). The required panel velocities for these cases with a 10^{o}deadrise angle would be 4.4 m/s and 6.28 m/s, respectively.

Table 3.5: Slamming loading conditions determining failure threshold

Case #	Force variation [N]	Average force [N]	Impulse per cycle [Ns]	μStrain variation Initial	Load duration [s]	Load [Hz]	Number of impacts	Damage
1	2146	798	403	872	1	1	10800	No
2	4416	1453	1456	1122	1	1	10800	No
3	6605	2961	2963	2543	1	1	4440	Yes
4	6823	3678	3683	910	1	1	3000	Yes

An example of damage growth can be seen in the TSA results in Figure 3.29 during a long term slamming event for Case #8 in Table 3.3. The most apparent effect was the initiation and growth of a delamination crack near the right support. The evolving stress state is more clearly visible by comparing the difference in stress at the various number of cycles to a reference stress state arbitrarily chosen to be at 24000 cycles and is presented in Figure 3.32, with the extent of the delamination crack indicated by an arrow. Positive regions indicate the stress increased while negative regions indicate the stress reduced after the indicated cyclic loading duration. The top center region should be ignored as the impactor came into and out of view resulting in poor DIC tracking and an

overly high temperature variation. Interesting changes in stress occurred near the delamination crack and in the center span. As the delamination crack initiated, the stress field was observed to increase near the support as apparent in Figure 3.32a. With continued delamination crack growth, a reduction in stress above the delamination crack was observed Figure 3.32b indicating the foam was no longer loaded there. An increase in center span stress occurred as the unloaded region above the delamination crack initialized but, as the crack continued to grow, the stress in the center span region reduced as the foam near the two supports began to carry more stress Figure 3.32c.

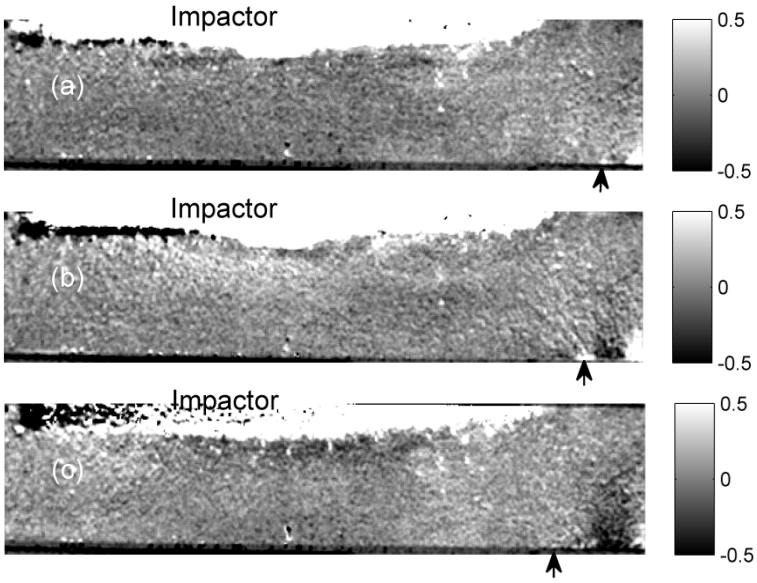

Figure 3.32: Difference in stress [MPa] between states at loading cycles (a) 48 k–24 k, (b) 60 k–24 k, (c) 72 k–24 k during Case #8 in Table 3.3. Sample supported at bottom corners of image and loaded at top center; arrows indicate delamination extent

3.4 Conclusions

In order to study damage mechanics in sandwich composites subject to hull slamming loads and to ensure repeatable slamming events, a mechanical slamming simulator (MSS) device was designed and constructed. Water impact pressure pulses from slamming

events were utilized in the design process so that the MSS could replicate the magnitude and duration of these pulses. The MSS offers several benefits over water tank investigations, including easy access to the sample during the slamming event for diagnostic equipment and an unobstructed optical path. The rate of loading with the MSS is on the order of Hertz, which is several orders of magnitude faster than water tank impacts, and facilitates damage progression studies within a reasonable time period. Several failure modes for the sandwich composite studied were predicted and found to vary depending on loading conditions. For the studied sandwich composite, delamination and core shear were expected failure modes based on pervious theoretical work [81] and experimental studies [76] of similar materials under three-point bending.

It was confirmed that the slamming event itself could be utilized as the thermoelastic source for TSA. A detailed calibration on the thermoelastic response of H100 PVC foam core was performed, including effects of permanent strain. This calibration was applied to a sandwich composite beam under three-point bending to determine the resulting stress field while simultaneously demonstrating the effectiveness of the DIC deformation correction routine. The relatively large displacements associated with bending loads resulted in spurious temperature or, equivalently, stress variations when DIC correction was not implemented. An additional aspect of the combined TSA-DIC method was demonstrated in the ability to report the full field strain field within the foam core. Comparing the stress field from the resulting DIC strain analysis to the TSA stress field revealed comparable magnitudes and distributions, but the resolution of TSA was much higher, as no differentiation or spatial averaging is required in the TSA method.

A series of long duration simulated slamming cases were performed at various intensities. Conditions that would initiate damage were investigated and the threshold surface pressure for damage was found to lie between 200 and 400 kPa. A finite element analysis (FEA) simulating a MSS loading was compared to the stress field found via TSA. Several key features were captured in two methods including the tension-compression transition within the stress field of the foam core, as well as the general displacement field. Deviations in the stress field indicate the foam model used for the FEA was too simplistic and a more accurate foam model would need to be implemented. The stress and displacement field within the foam core around a slowly growing delamination crack was measured during a long duration slamming test.

The combined TSA-DIC method was demonstrated on a polymeric foam core material under in situ simulated slamming loading conditions. The benefit of the DIC correction is evident in cases with large deflections such as bending. The novel combination of TSA and DIC adds additional analysis capability to damage studies especially under complex loading conditions. With future refinement and application of combined TSA-DIC, this method can shed insight on the damage process in sandwich composites under hull slamming loads. This method can also easily be extending into other damage scenarios such as growing fatigue cracks in metals.

References

10. Dobrovol'skaya, Z.N., *On Some Problems of Similarity Flow of Fluid with a Free Surface.* Journal of Fluid Mechanics, 1969. **36**: p. 805–829.
11. Zhao, R. and Faltinsen, O., *Water Entry of 2-Dimensional Bodies.* Journal of Fluid Mechanics, 1993. **246**: p. 593–612.
16. Stenius, I., *Hydroelasticity in Marine Hull Bottom Panels — Modeling and Characterization*, in *KTH Engineering Sciences*. 2009, KTH Centre for Naval Architecture: Stockholm, Sweden.
76. Kulkarni, N., Mahfuz, H., Jeelani, S., and Carlsson, L.A., *Fatigue crack growth and life prediction of foam core sandwich composites under flexural loading.* Composite Structures, 2003. **59**(4): p. 499–505.
81. Steeves, C.A. and Fleck, N.A., *Collapse mechanisms of sandwich beams with composite faces and a foam core, loaded in three-point bending. Part 1: analytical models and minimum weight design.* International Journal of Mechanical Sciences, 2004. **46**(4): p. 561–583.
82. DIAB. *Divinycell H Technical Data Sheet*. Available from: http://www.diabgroup.com/americas/u_literature/u_pdf_files/u_ds_pdf/H_DS_US.pdf.
91. Dulieu-Barton, J.M., Fulton, M.C., and Stanley, P., *The analysis of thermoelastic isopachic data from crack tip stress fields.* Fatigue & Fracture of Engineering Materials & Structures, 2000. **23**(4): p. 301–313.
93. Dulieu-Barton, J.M., Emery, T.R., Quinn, S., and Cunningham, P.R., *A temperature correction methodology for quantitative thermoelastic stress analysis and damage assessment.* Measurement Science & Technology, 2006. **17**(6): p. 1627–1637.
100. Maldague, X., *Theory and practice of infrared technology for nondestructive testing*. Wiley series in microwave and optical engineering. 2001, New York;: Wiley. xix, 684 p.
118. USNavy, *Shock Tests. H.I. (High-Impact) Shipboard Machinery, Equipment, and Systems, Requirements for MIL-S-901D*. 1989.

119. Rosen, A., *Loads and Responses for Planing Craft in Waves*, in *Aeronautical and Vehicle Engineering Division of Naval Systems*. 2004, KTH: Stockholm, Sweden.

120. Soden, P.D., Kaddour, A.S., and Hinton, M.J., *Recommendations for designers and researchers resulting from the world-wide failure exercise.* Composites Science and Technology, 2004. **64**(3–4): p. 589–604.

121. Cytec. *Thornel T300 PAN-Based Fiber Properties*. Available from: http://www.cytec.com/engineered-materials/products/Datasheets/T300%20RevA7-12-06.pdf.

122. Derakane. *DERAKANE 8084 Epoxy Vinyl Ester Resin Properties*. Available from: http://www.derakane.com/derakaneControllerAction.do?method=goToProductDetailPage&actionForwardName=derakane8084&productCode=536004.

123. Soden, P.D., Hinton, M.J., and Kaddour, A.S., *Biaxial test results for strength and deformation of a range of E-glass and carbon fibre reinforced composite laminates: failure exercise benchmark data.* Composites Science and Technology, 2002. **62**(12–13): p. 1489–1514.

124. Stinchcomb, W., *Nondestructive evaluation of damage accumulation processes in composite laminates.* Composites Science and Technology, 1986. **25**(2): p. 103–118.

125. Emery, T.R. and Dulieu-Barton, J.M., *Damage monitoring of composite materials using pulsed phase thermography and thermoelastic stress analysis.* Damage Assessment of Structures VII, 2007. **347**: p. 621–626.

Chapter 4: Conclusions and Future Work

4.1 Conclusions

This thesis is concerned with investigating damage evolution in sandwich structures under repeated transient loading conditions associated with impulse loading due to hull slamming of high speed marine craft. A novel experimental technique to aid in the study of damage progression that combines thermoelastic stress analysis (TSA) and digital image correlation (DIC) simultaneously utilizing a single infrared camera is described. Application of this testing method to ship structures would provide an efficient resource to validate new components before full scale construction. This would help ensure a safe craft before in-service operation. The TSA analysis based on full field measurement of temperature and thermoelasticity provides a full field measure of the sum of principal stresses on the observed surface. The DIC analysis provides the corresponding deformation field, which improves the TSA analysis by distortion correction due to rigid body motion and the strain field. This distortion correction ability is particularly necessary in cases with relatively large motion, as in bending of sandwich composites beans, to produce accurate thermal variation analyses.

A technique to reliably perform DIC with an infrared camera needed was developed. This technique involved creating a speckle pattern paint mixture that provides thermal contrast by creating an emissivity differential to the background. The combined TSA-DIC method was demonstrated on several benchmark problems under cyclic loading including plate structures with holes and cracks, and bimaterials. The validated technique was applied to foam core sandwich composite beams under repeated simulated wave

slamming loading. There are numerous failure modes in sandwich composite materials and the full field stress and strain from TSA and DIC, respectively, allow for improved failure analysis and prediction. Understanding damage in sandwich structures under impulse loading is a complex open area of research and the combined TSA-DIC method provides further insight into the failure process.

A device to mechanically load samples cyclically for long durations with adjustable loading was designed, constructed, and utilized to simulate hull and wave slamming loads on foam core sandwich composites. Wave slamming loads are large, destructive, pressure pulses on a ship's hull resulting from water impact. Hull slamming involves repeated impact of the hull structure of high speed marine craft and generates periodic impulsive loads resulting in fatigue damage. The mechanical device known as the slamming simulator was designed to impart similar magnitude pulses at a frequency of several Hertz which allows significant time savings in long duration testing over impact testing in a water tank. Additionally, the mechanical slamming simulator (MSS) has the benefit that the impacting head does not heat up, like the grips in a servohydraulic testing machine, during long duration cyclic testing due to the contact of the hydraulic fluid with the piston. This additional heat may influence material properties and degrade a TSA analysis. As the driving force in the MSS utilized compressed air, this heating issue was bypassed. The MSS enables monitoring progression of damage through non-contact techniques which would not be feasible in water tank testing.

Long duration simulated slamming tests were performed on sandwich composites representative of modern high speed marine craft hulls and several failure modes were detected via application of the combined TSA-DIC method on the PVC foam core. In

particular, a growing delamination crack was observed, along with the evolving stress field within the foam core. The TSA-DIC method was shown to improve the accuracy and resolution of the stress field determined by the thermoelastic effect. Under cyclic loading, the temperature variation from the thermoelastic effect can be directly related to the variation in the sum of principal stresses. The deformation field determined via DIC provides the distortion correction capability and is especially apparent in areas with large motion or thermal gradients. The motion resulting from loading may introduce spurious amounts of thermal variation at the loading frequency that degrade the accuracy of the reported stress field. By combining the TSA and DIC method with a single infrared (IR) camera, the resulting experimental setup was straight forward and without the need to correct for geometric effects of two spatially separate cameras. TSA itself is a robust method for obtaining the full field stress, as there is no need for the precise alignment of multiple lenses, wave plates, or polarizers found in other full field methods. Additionally, there is no need for external lighting in TSA or DIC in IR, as the measured electromagnetic radiation is emitted by the samples' thermal fields. Example applications of the TSA-DIC method were demonstrated for the benchmark cases of a plate with a hole under uniaxial tension and a Mode I crack. The resulting measured stress fields were compared to theoretical and simulated solutions and the effect of DIC distortion correction was enumerated. The temperature variation field around a cyclically compressed bimaterial crack was found to have a discontinuity but when the thermoelastic sensitivities of each material were accounted for, a nearly continuous stress field emerged. The ability of the TSA-DIC method to measure the stress field in the foam

core of a sandwich composite under bending was demonstrated, while also improving the accuracy of the stress field by accounting for the large deflection.

In order to apply the TSA method, several calibration studies were performed to relate temperature variation to stress variation. Direct thermal measurements for extruded acrylic, cast Nylon 6 and Divinycell H100 PVC foam at known stresses levels were used to determine their respective thermoelastic sensitivities. The materials were milled to precise dimensions and cyclically loaded uniaxially at known stress levels then correlated to measured temperature variations. The resulting calibration was precise enough to correctly account for the temperature variation discontinuity across the bimaterial interface of nylon and acrylic. In addition to the thermoelastic calibration, the Poisson's ratio and elastic modulus were determined by tracking the motion of several applied speckle spots within the infrared images. The thermoelastic sensitivity of H100 PVC foam was also investigated as a function of permanent compressive strain. A model accounting for the changing density as well as elastic modulus change for H100 foam due to permanent strain was proposed, but found to overestimate the thermoelastic sensitivity. The trend of decreasing sensitivity with permanent compressive strain was captured and the effect of changing elastic modulus was found to be negligible. To improve the TSA model for H100 foam with damage, an accurate measurement of the initial linear thermal expansion coefficient should be made, as well as confirming any variation as a function of permanent strain.

4.2 Future Work

The TSA-DIC method combines two optical diagnostic techniques that give a measure of the full field state of stress within a sample. It was demonstrated that both

analyses could be simultaneously performed utilizing a single infrared camera and that under certain conditions the deformation correction is required to produce valid results. Future research on this method should improve the DIC portion such that higher-resolution strain measurements could be obtained to aid in separating individual components of stress field from the TSA analysis. The physical application of the infrared contrasting speckle pattern could also be optimized for DIC while still retaining an accurate thermal variation field from the TSA analysis. A correction factor based on the emissivity of the speckles could be applied to the thermal variations measured at the speckles so that the temperature variation field would be continuous. The TSA-DIC method could also be utilized to measure the linear thermal expansion coefficient by tracking the distortion caused by a known temperature change. The combined TSA-DIC method can also be extended to crack growth and initiation studies for composite sandwich materials by observing the complex stress fields and how they influence the crack behavior. Also, some unique aspects of the method could be exploited, such as the lack of need for external lighting, which could be utilized to characterize a photosensitive material. Investigations on influence of temperature on material properties could also be readily performed. The DIC method in conjunction with a high speed infrared camera could determine both the strain field and any heat output simultaneously in a rapidly deforming material.

This thesis demonstrated a novel diagnostic technique that provides a full field measurement of the stress within a sandwich composite under hull slamming loads. Additional studies should be performed to better understand the damage evolution and failure modes in sandwich composites under hull slamming conditions. High cycle

fatigue tests should be performed for various geometries to elucidate both damage initiation threshold and expected failure modes. Life prediction under hull slamming loads could be based on the expected failure mode for the geometry and the intensity of repeated impacts. Geometric factors of the sandwich composite, such as face-sheet-to-core-thickness ratio and loading span also influence the failure modes. One such mode known as core shear failure could be initiated in a number of ways, possibly by coalescing micro cracks or by a growing kink crack. By observing the various failure processes, indicators of progressive damage may become apparent before failure and act as life prediction measures. Detailed observations of a delamination crack using the TSA-DIC method could help produce an improved model for failure prediction by finding what factors influence the delamination process. Also, changing surface strains measured by bonded strain gages could be correlated to internal damage observed via TSA-DIC giving a predicted damage state within the sandwich composite when the infrared camera is not present. The surface strains could also be correlated to experimental or numerical hull slamming events of various impact angles and velocities as verification that the applied loads match a particular slamming condition.

The mechanical slamming simulator (MSS) could be improved by adding computer controlled pressure adjustments by either feedback control of the piston valve or a controlled variable pressure regulator. The addition of a valve that operates without a large pressure differential would extend the operating range of the MSS by allowing low force ability. The impactor shape could be optimized to more closely match a characteristic hull slamming pressure pulse. In order to capture the traveling pulse aspect of a slamming event, an impactor head that adjusts the impact angle as the force increases

would be necessary. The robust nature of combined TSA-DIC to simultaneously measure stress and deformation with a single IR camera warrants additional studies exploiting this unique ability, particularly in large deformation cases.

Appendix A: Thermoelastic Calibration of H100 Foam

A.1 Background on Polymeric Foams

Polymeric foams can be separated into three broad categories based on the cell structure. These categories are open-cell foams, reticulated foams, and closed-cell foams. Open cell foams are porous in nature, having both open and closed cell membranes, thus allowing the fluid to penetrate easily. The resulting foam is soft and flexible and has many uses in energy absorbing applications such as automobile seats, furniture, sporting goods, and packaging. Reticulated foams have completely open cell structures where the membranes or windows between adjacent cells are removed in a post process of either carefully controlled burning or chemical erosion, leaving a skeletal network of the linear boundaries between cells. The large surface area of the membranes versus the linear boundaries between cells allows the chemical reaction to selectively remove these elements [126]. The resulting reticulated or netlike structure is extremely open and has application where high porosity and large surface area are needed, such as in filtering and sound absorption. Closed cell foams have completely sealed cell structure where the membrane walls enclose air pockets resulting in a structure that does not absorb fluids or moisture, making them ideal for marine applications. The increased rigidity from the closed cell walls allows the foam to retain its structure under load and thus may be suitable for many structural applications. The focus of this work on foams dealt with a closed cell PVC foam Divinycell H100 [82]. Foamed plastics or polymeric foams can be produced by several methods, including injection molding, open cast molding, or continuous foam production, where the sheets are cut to desired shape after curing. There

are numerous foaming processes where bubbles can be introduced into the liquid polymer. A common method is by the addition of chemical substances known as ‘blowing agents’ where a reaction causes a release of gas either by increased temperature or reduced pressure [127]. These gas bubbles increase in size and with the proper chemical mixture and processing either open or closed cell foams can be produced.

When analyzing properties of foams, the observed scale plays a key role, as they appear to behave as homogenous material on a scale much larger than the cell size but become heterogeneous when the scale approaches the cell size. On the scale of the cell, the microstructure becomes relevant as individual cell walls deform and buckle under loading with properties of the bulk material. At the large scale, enough randomly oriented cells produce an averaged quasi-isotropic composite substance of bulk material such as PVC as the cell walls and air or other gas are used in the foaming process. This composite structure may have a slight anisotropy in the rise direction as the bubbles will tend to rise against gravity during the cure process. Properties such as elastic modulus, Poisson ratio, and yield stress can be determined using standard testing methods. The multi-axial yield behavior of the PVC H100 foam was thoroughly investigated by Deshpande and Fleck [80] and they ensured their specimens had at least 50 cells in the testing dimension to ensure macroscopically representative properties. Under uniaxial tension and compression, they found the tensile and compressive yield stresses approximately 20% higher in the rise direction. The tensile yield stress for H100 was found to be about 1.8 MPa, while the compressive yield stress was about 1.2 MPa in the direction perpendicular to the rise direction. This discrepancy was attributed to the differing failure modes within the cell structure. Under tensile loading, the deformation of

the foam is dominated by bending of the cell walls and the formation of plastic hinges at the nodes, while under compressive loading the deformation is dominated by buckling of the cell walls.

A.2 Thermoelastic Analysis of Damaged H100 PVC Foam

In order to determine the full field sum of principal stresses by applying the thermoelastic relation (A.6) on H100 PVC foam, certain criteria must be met. The sample must be loaded elastically so that any temperature change can be related to elastic deformations alone and cyclically at a rate that satisfies the adiabatic assumption. Additionally, the material properties may vary with damage or temperature and should be accounted for in any model for the thermoelastic response. Recent work by Dulieu-Barton [128], has shown that the elastic modulus of H100 decreases by about 5% at 310 K over the stiffness at 293 K, and is shown in Figure A.1. The foam surface must also be prepared with a high emissivity coating so that a correct temperature variation measurement can be determined via thermoelastic stress analysis (TSA).

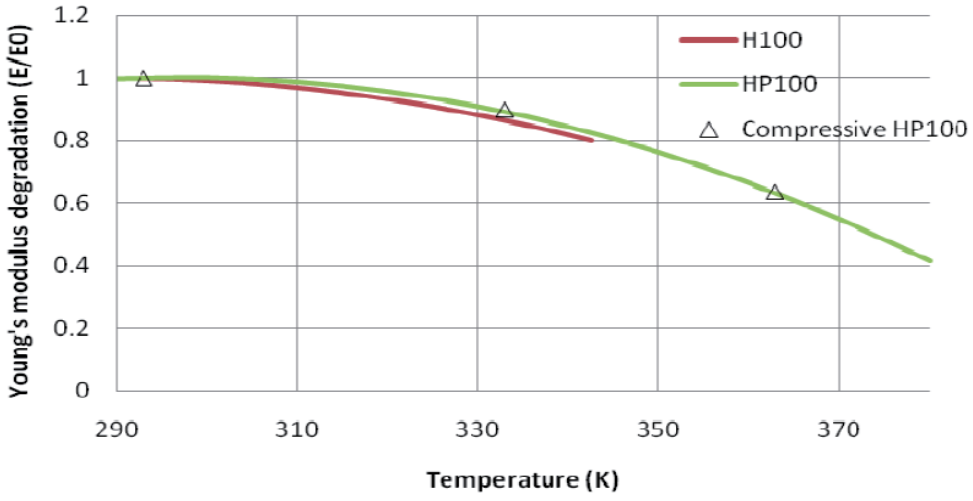

Figure A.1: Normalized temperature-dependent elastic modulus of Divinycell H100 and HP100 foam [128]

A.2.1 Thermoelastic properties of H100 PVC foam

The basic TSA relation (A.6) shows the thermoelastic sensitivity dependent on density, specific heat capacity, linear thermal expansion coefficient, and absolute temperature. When the foam material is compressed beyond the yield point it is considered damaged, as some amount of permanent strain remains and other properties are affected. The density is dependent on the strains in the x, y, and z directions, as shown in (A.1). This relation can be specialized for uniaxial loading assuming the volume change to be zero (plastic incompressibility, zero plastic Poisson's ratio) above the yield strain, ε_c, as in (A.2). This implies the foam does not expand by the Poisson effect when compressed beyond the yield stress, as observed in [80] at, ε_c = 0.035.

$$\rho_{new} = \rho_o / \left[(1+\varepsilon_x)(1+\varepsilon_y)(1+\varepsilon_z)\right] \tag{A.1}$$

$$\rho_{new} = \begin{cases} \rho_o / \left[(1+\varepsilon_x)(1-\nu\,\varepsilon_x)^2\right] & ;\ for\ \varepsilon_x \le \varepsilon_c \\ \frac{\rho_o}{\left[(1+\varepsilon_c)(1-\nu\,\varepsilon_c)^2\right]} / \left[1+(\varepsilon_x-\varepsilon_c)\right] & ;\ for\ \varepsilon_x > \varepsilon_c \end{cases} \tag{A.2}$$

The effect of various assumptions of the Poisson effect on the density of H100 foam as a function of strain is presented in Figure A.2. When the initial Poisson's ratio is applied for all strain levels the density is greatly underestimated. The density is slightly overestimated when the Poisson effect is ignored, compared to when the Poisson effect is applied until the foam yields.

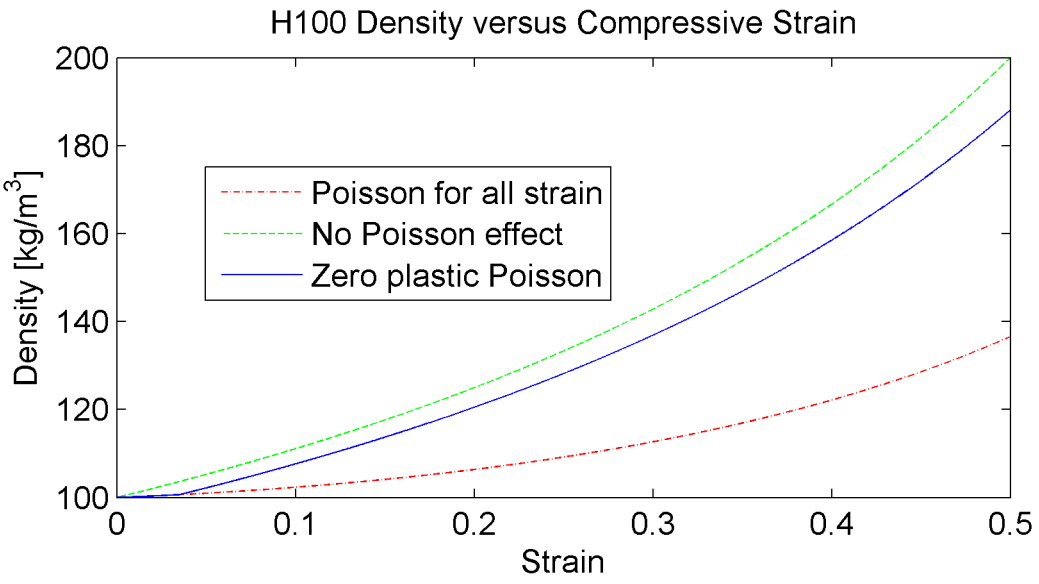

Figure A.2: Density of H100 versus strain for various assumptions on Poisson effect

The elastic modulus for several densities of Divinycell H series foams and the effect of strain level on modulus has been determined by Kidd [129]. Kidd utilized ultrasonic waves to determine the elastic modulus and Poisson ratio in situ by measuring the longitudinal (c_d) and shear (c_s) wave speeds during compression testing. The relations between wave speeds, elastic modulus (E), and Poisson's ratio (v) are shown in relations (A.3) and (A.4).

$$E = \rho c_s^2 \frac{4c_s^2 - 3c_d^2}{c_s^2 - c_d^2} \tag{A.3}$$

$$v = \frac{c_d^2 - 2c_s^2}{2(c_d^2 - c_s^2)} \tag{A.4}$$

The apparent modulus for Divinycell H130 foam measured by Kidd versus strain under uniaxial compression is shown in Figure A.3. The elastic modulus suffers a sudden decrease of 35 MPa at a strain of approximately 0.08 but otherwise has a steady decrease of about 0.60 MPa/(% strain) as described by (A.5). Kidd also determined the Poisson's

ratio during the compression test, which is shown in Figure A.4, and found that the Poisson's ratio remains fairly constant at about 0.42. As an approximation for H100 foam, these results for H130 foam will be utilized to estimate the effect of elastic modulus change in the thermoelastic model of H100 PVC foam.

$$E' = \begin{cases} E_0 - 60\varepsilon & for\ \varepsilon \leq 0.08 \\ (E_0 - 35) - 60\varepsilon & for\ \varepsilon > 0.08 \end{cases} \quad \text{(A.5)}$$

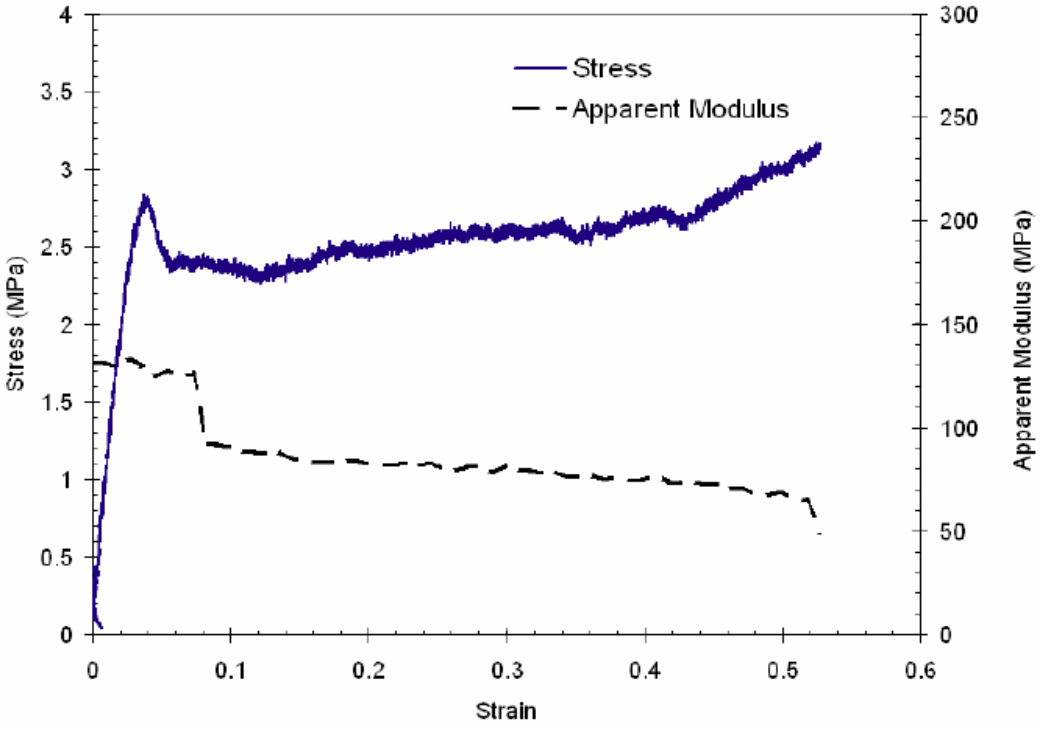

Figure A.3: Apparent modulus of H130 foam from [129] during uniaxial compression test

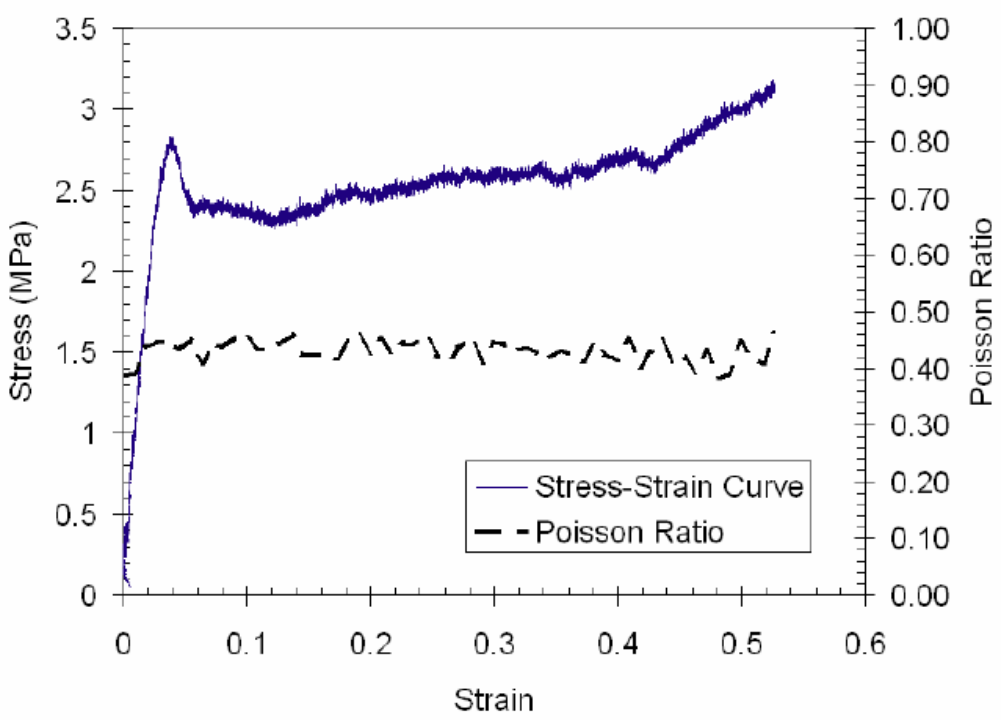

Figure A.4: Poisson's ratio for H130 foam under uniaxial compression [129]

A.2.2 Thermoelastic model of H100 PVC foam

The basic thermoelastic relation for an isotropic homogenous body is given in (A.6). A more general form is given in (A.7) that utilizes an alternative form of the specific heat that includes the elastic modulus, Poisson's ratio, and density. The properties for undamaged H100 foam are presented in Table A.1.

Table A.1: Properties of H100 PVC foam

	Nominal Density (kg/m^3)	Elastic Modulus (MPa)	Poisson's ratio	Coefficient of linear expansion	Specific heat capacity (J/(kg-K))
H100 PVC foam	100[a]	130[a]	0.42	$35x10^{-6}/^oC$[b]	1790[b]

[a][82], [b][130]

$$\Delta\sigma_{kk} = -\Delta T \frac{\rho}{\alpha T_0} c_p \tag{A.6}$$

$$\Delta\sigma_{kk} = -\Delta T \frac{\rho}{\alpha T_0}\left[c_\varepsilon + \frac{3E\alpha^2 T_0}{\rho(1-2\nu)}\right] \tag{A.7}$$

A modified form of the thermoelastic relation, using the relation for density (A.2) as a function of strain modified for uniaxial loading, ε_x , and the approximate relation for elastic modulus change (A.5), is given in relation (A.8). The specific heat at constant volume, c_ε, in (A.9) is assumed to remain unchanged and was determined by comparing (A.7) and (A.6) using initial properties of the elastic modulus and density. The model of thermoelastic sensitivity for H100 PVC foam allowing for density and elastic modulus change due to compressive strain is shown in Figure A.5 and compared to measured values. The effect of changing the elastic modulus due to permanent strain was found have a negligible effect on the thermoelastic sensitivity.

$$\Delta\sigma_{kk} = -\Delta T \frac{\rho_{new}}{\alpha T_0}\left[c_\varepsilon + \frac{3E'\alpha^2 T_0}{\rho_{new}(1-2\nu)}\right] \; with$$

$$\rho_{new} = \begin{cases} \frac{\rho_o}{[(1+\varepsilon_x)(1-\nu\,\varepsilon_x)^2]} & ;\; for\ \varepsilon_x \le \varepsilon_c \\ \frac{\rho_o}{[(1+\varepsilon_c)(1-\nu\,\varepsilon_c)^2]} \Big/ [1+(\varepsilon_x-\varepsilon_c)] & ;\; for\ \varepsilon_x > \varepsilon_c \end{cases} \tag{A.8}$$

$$c_\varepsilon = c_{po} - \frac{3E_0\alpha^2 T_0}{\rho_0(1-2\nu)} \tag{A.9}$$

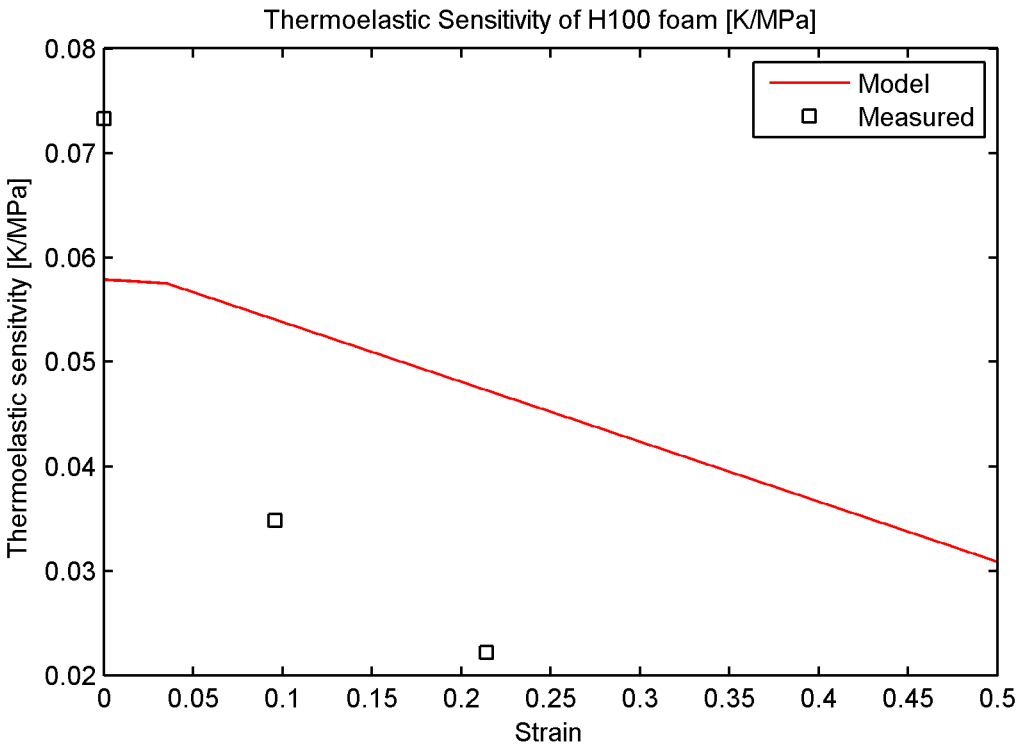

Figure A.5: Model prediction for thermoelastic sensitivity of H100 foam with evolving density and elastic modulus with strain

A.2.3 Comparison and discussion of model

The thermoelastic sensitivity for H100 was determined for several levels of permanent strain. The samples were milled to the specified initial dimensions such that the opposing faces were highly parallel. The samples were then compressed in a servohydraulic testing machine to the specified permanent strain. The sample surface was then coated with a high emissivity spray paint Krylon 1602 and cyclically loaded at various stress levels staying below the yield stress. The measured thermoelastic sensitivities and corresponding sensitivities predicted by the model where evolution of density and elastic modulus were accounted for are presented in Table A.2. The discrepancy between experimental and model values may come from the assumption that

the coefficient of linear thermal expansion remains constant or of the nominal value specified by the manufacturer for H100 foam may be not applicable. To match the sensitivity at zero permanent strain, the thermal expansion coefficient would have to be $42x10^{-6}$ /K, which is $7x10^{-6}$ higher than the reported value. Assuming the specific heat at constant volume does not change with permanent strain, the required thermal expansion coefficient at 9.6% and 21% strain would be 22x10-6/K and $16x10^{-6}$ /K, respectively. In order to improve the thermoelastic model for H100 foam, the effect of permanent strain on the coefficient of linear thermal expansion should be determined.

Table A.2: H100 calibration properties and measured thermoelastic sensitivity

Sample	Initial Dimensions (mm)	Tested Dimensions (mm)	Tested Density (kg/m^3)	Permanent Uniaxial Strain	Measured Thermoelastic Sensitivity ($^oC/MPa$)	Model Sensitivity at given strain
S5	29.7 x 40.9 x 52.9	29.7 x 40.2 x 52.9	102	0	0.0733	0.0579
S7	38.5 x 45.7 x 48.3	39.3 x 45.6 x 43.6	104	-0.096	0.0348	0.0541
S9	46.6 x 50.3 x 40.7	47.3 x 51.1 x 32.0	117	-0.214	0.0222	0.0473

References

80. Deshpande, V.S. and Fleck, N.A., *Multi-axial yield behaviour of polymer foams.* Acta Materialia, 2001. **49**(10): p. 1859–1866.

82. DIAB. *Divinycell H Technical Data Sheet*. Available from: http://www.diabgroup.com/americas/u_literature/u_pdf_files/u_ds_pdf/H_DS_US.pdf.

126. UnitedFoam. *Recticulted foam*. Available from: http://steplaw.com/reticulatedfoam.html.

127. Klempner, D., Sendijarevic, V., and Aseeva, R.M., *Handbook of polymeric foams and foam technology*. 2nd ed. 2004, Munich: Hanser Publishers 584 pp.

128. Dulieu-Barton, J.M., Boyenval Langlois, C., Thomsen, O.T., Zhang, S., and Fruehmann, R.K., *Derivation of temperature dependent mechanical properties of polymer foam core materials using optical extensometry.* EPJ Web of Conferences, 2010. **6**: p. 38004.

129. Kidd, T.H., *Mechanical characterization of damage and failure in polymeric foams and glass/epoxy composites*. PhD Dissertation 2006, California Institute of Technology: Pasadena, CA.

130. DIAB. *DIAB Divinycell® H 100 Semi-rigid PVC Foam Core Material* Available from: http://www.matweb.com/search/datasheet.aspx?matguid=0872e8bd246246aaa7e3c5f6edd892d9.

Bibliography

1. Mouritz, A.P., Gellert, E., Burchill, P., and Challis, K., *Review of advanced composite structures for naval ships and submarines.* Composite Structures, 2001. **53**(1): p. 21–41.
2. Faltinsen, O.M., *Hydrodynamics of high-speed marine vehicles*. 2005, Cambridge; New York: Cambridge University Press. xix, 454 p.
3. Faltinsen, O.M., *The effect of hydroelasticity on ship slamming.* Philosophical Transactions of the Royal Society of London Series A—Mathematical Physical and Engineering Sciences, 1997. **355**(1724): p. 575–591.
4. White, B.S. and Fornberg, B., *On the chance of freak waves at sea.* Journal of Fluid Mechanics, 1998. **355**: p. 113–138.
5. Kharif, C. and Pelinovsky, E., *Physical mechanisms of the rogue wave phenomenon.* European Journal of Mechanics B—Fluids, 2003. **22**(6): p. 603–634.
6. Faltinsen, O.M., *Water entry of a wedge with finite deadrise angle.* Journal of Ship Research, 2002. **46**(1): p. 39-51.
7. Greenhow, M. and Lin, W.M., *Non linear free surface effects: experiments and theory, Report Number 83-19*. 1983, Department of Ocean Engineering, MIT: Cambridge, MA.
8. Karman, T.V., *The impact of seaplance floats during landing* 1929, NACA, TN 321: Washington.
9. Wagner, V.H., *Phenomena associated with impact and sliding on liquid surfaces*. 1932, NACA, Transaction 1366, translated from ZAMM. 12: 193–215.
10. Dobrovol'skaya, Z.N., *On Some Problems of Similarity Flow of Fluid with a Free Surface.* Journal of Fluid Mechanics, 1969. **36**: p. 805–829.
11. Zhao, R. and Faltinsen, O., *Water Entry of 2-Dimensional Bodies.* Journal of Fluid Mechanics, 1993. **246**: p. 593–612.
12. Zhao, R. and Faltinsen, O.M. *Water entry of arbitrary two-dimensional sections with and without flow separation*. in *Symp. on Naval Hydrod.* 1997. Trondheim: National Academy Press.

13. Faltinsen, O.M., Landrini, M., and Greco, M., *Slamming in marine applications.* Journal of Engineering Mathematics, 2004. **48**(3–4): p. 187–217.
14. Faltinsen, O.M., *Hydroelastic slamming.* Journal of Marine Science and Technology, 2000. **5**(2): p. 49–65.
15. Haymen, B., Haug, T., and Valsgard, S. *Slamming drop tests on a GRP sandwich hull model*. in *ICSC2*. 1992. Florida.
16. Stenius, I., *Hydroelasticity in Marine Hull Bottom Panels — Modeling and Characterization*, in *KTH Engineering Sciences*. 2009, KTH Centre for Naval Architecture: Stockholm, Sweden.
17. Battley, M., Allen, T., Schierlink, J., Lake, S., and Pehrson, P. *Hydroelastic Behaviour of Slam Loaded Composite Hull Panels*. in *3rd High Performance Yacht Design Conference*. 2008. Auckland.
18. Battley, M. and Lake, S., *Dynamic performance of sandwich core materials.* 16th International Conference on Composite Materials, 2007.
19. Stenius, I., Rosen, A., and Kuttenkeuler, J., *Explicit FE-modeling of fluid-strucutre interaction in hull-water impacts.* International Shipbuilding Progress, 2006. **53**(2): p. 103–121.
20. Stenius, I., Rosen, A., and Kuttenkeuler, J., *Explicit FE-modelling of hydroelasticity in panel-water impacts.* International Shipbuilding Progress, 2007. **54**(2–3): p. 111–127.
21. Qin, Z. and Batra, R.C., *Local slamming impact of sandwich composite hulls.* International Journal of Solids and Structures, 2009. **46**(10): p. 2011–2035.
22. Vinson, J.R. and Sierakowski, R.L., *The behavior of structures composed of composite materials*. 2nd ed. Solid mechanics and its applications. 2002, Dordrecht; Boston: Kluwer Academic Publishers. xiv, 435 p.
23. Record, S.J., *The Mechancial Properties of Wood Including a Discussion of the Factors Affecting the Mechanical Properites , and Methods of Tiber Testing*. 1914, New York: John Wiley and Sons, Inc.
24. *Biomedical materials*. 2009, New York: Springer.

25. Laraia, V.J. and Heuer, A.H., *Novel Composite Microstructure and Mechanical Behavior of Mollusk Shell.* Journal of the American Ceramic Society, 1989. **72**(11): p. 2177–2179.
26. Agarwal, B.D., Broutman, L.J., and Chandrashekhara, K., *Analysis and performance of fiber composites*. 3rd ed. 2006, Hoboken, N.J.: John Wiley. xiv, 562 p.
27. Vinson, J.R. and Chou, T.-W., *Composite materials and their use in structures*. 1975, New York: Wiley. xii, 438 p.
28. Bishop, E., *The Mosquito: the wooden wonder*. 1990, Washington, D.C.: Smithsonian Institution Press. 170 p.
29. Agarwal, B.D. and Broutman, L.J., *Analysis and performance of fiber composites*. SPE monographs. 1980, New York: Wiley. ix, 355 p.
30. DIAB. *DIAB — Sandwich Composite Cores*. Available from: http://www.railway-technology.com/contractors/passenger/diab/.
31. DIAB. *DIvinycell P foam Low FST, Thermoplastic Core*. Available from: http://www.diabgroup.com/americas/u_products/u_divinycell_p.html.
32. Ko, W., Gong, L., and Quinn, R., *Reentry Thermal Analysis of a Generic Crew Exploration Vehicle Structure.* NASA TM-214607, 2007.
33. Crane, R., Gillespie, J., Heider, D., Yarlagadda, S., and Advani, S., *Intelligent Processing and Inspection of Naval Composites.* AMPTIAC Quarterly, 2003. **7**(3): p. 41–48.
34. Sun, C.T. and Zhou, S.G., *Failure of Quasi-Isotropic Composite Laminates with Free Edges.* Journal of Reinforced Plastics and Composites, 1988. **7**(6): p. 515–557.
35. Sun, C.T. and Kelly, S.R., *Failure in Composite Angle Structures .1. Initial Failure.* Journal of Reinforced Plastics and Composites, 1988. **7**(3): p. 220-232.
36. Sun, C.T. and Kelly, S.R., *Failure in Composite Angle Structures .2. Onset of Delamination.* Journal of Reinforced Plastics and Composites, 1988. **7**(3): p. 233–244.
37. Zhou, S.G. and Sun, C.T., *Failure Analysis of Composite Laminates with Free Edge.* Journal of Composites Technology & Research, 1990. **12**(2): p. 91–97.
38. Waas, A.M., Babcock, C.D., and Knauss, W.G., *An Experimental-Study of the Initiation and Progression of Damage in Compressively Loaded Composite*

Laminates in the Presence of a Circular Cutout. AIAA/ASME/ASCE/AHS/ASC 30th Structures, Structural Dynamics and Materials Conference, Pts 1–4, 1989: p. 1000–1011.

39. Waas, A.M., Babcock, C.D., and Knauss, W.G., *Damage Progression in Compressively Loaded Laminates Containing a Circular Cutout.* Aiaa Journal, 1991. **29**(3): p. 436-443.
40. Comiez, J.M., Waas, A.M., and Shahwan, K.W., *Delamination Buckling — Experiment and Analysis.* International Journal of Solids and Structures, 1995. **32**(6–7): p. 767–782.
41. Schultheisz, C.R. and Waas, A.M., *Compressive failure of composites .1. Testing and micromechanical theories.* Progress in Aerospace Sciences, 1996. **32**(1): p. 1-42.
42. Waas, A.M. and Schultheisz, C.R., *Compressive failure of composites .2. Experimental studies.* Progress in Aerospace Sciences, 1996. **32**(1): p. 43–78.
43. Carlsson, L.A., Gillespie, J.W., and Pipes, R.B., *On the Analysis and Design of the End Notched Flexure (Enf) Specimen for Mode-II Testing.* Journal of Composite Materials, 1986. **20**(6): p. 594–604.
44. Trethewey, B.R., Gillespie, J.W., and Carlsson, L.A., *Mode-II Cyclic Delamination Growth.* Journal of Composite Materials, 1988. **22**(5): p. 459–483.
45. Ozdil, F. and Carlsson, L.A., *Mode-I Interlaminar Fracture of Interleaved Graphite Epoxy.* Journal of Composite Materials, 1992. **26**(3): p. 432–459.
46. Whitcomb, J.D., *Finite Element Analysis of Instability Related Delamination Growth.* Journal of Composite Materials, 1981. **15**(5): p. 403–426.
47. Shivakumar, K.N. and Whitcomb, J.D., *Buckling of a Sublaminate in a Quasi-Isotropic Composite Laminate.* Journal of Composite Materials, 1985. **19**(1): p. 2–18.
48. Whitcomb, J.D. and Woo, K., *Analysis of Debond Growth in Tubular Joints Subjected to Tension and Flexural Loads.* Computers & Structures, 1993. **46**(2): p. 323–329.
49. Daniel, I.M., *Experimentation and modeling of composite materials.* Experimental Mechanics, 1999. **39**(1): p. 1–19.

50. Hinton, M.J. and Soden, P.D., *Predicting failure in composite laminates: The background to the exercise.* Composites Science and Technology, 1998. **58**(7): p. 1001–1010.
51. Hinton, M.J., Kaddour, A.S., and Soden, P.D., *Evaluation of failure prediction in composite laminates: background to 'part C' of the exercise.* Composites Science and Technology, 2004. **64**(3–4): p. 321–327.
52. Daniel, I.M., *Failure of composite materials.* Strain, 2007. **43**(1): p. 4–12.
53. Hill, R., *A theory of the yielding and plastic flow of anisotropic metals.* Proceedings of the Royal Society of London. Series A—Mathematical and Physical Sciences, 1948. **193**(1033): p. 281–297.
54. Christensen, R.M., *Stress based yield/failure criteria for fiber composites.* International Journal of Solids and Structures, 1997. **34**(5): p. 529–543.
55. Oguni, K. and Ravichandran, G., *A micromechanical failure model for unidirectional fiber reinforced composites.* International Journal of Solids and Structures, 2001. **38**(40–41): p. 7215–7233.
56. Daniel, I.M. and Ishai, O., *Engineering mechanics of composite materials*. 2nd ed. 2006, New York: Oxford University Press. xviii, 411 p.
57. Chow, W.T. and Atluri, S.N., *Stress intensity factors as the fracture parameters for delamination crack growth in composite laminates.* Computational Mechanics, 1998. **21**(1): p. 1–10.
58. Ikeda, T. and Sun, C.T., *Stress intensity factor analysis for an interface crack between dissimilar isotropic materials under thermal stress.* International Journal of Fracture, 2001. **111**(3): p. 229–249.
59. Erdogan, F., *Stress Distribution in Bonded Dissimilar Materials with Cracks.* Journal of Applied Mechanics, 1965. **32**(2): p. 403.
60. Ghahremani, F. and Shih, C.F., *Corner Singularities of 3-Dimensional Planar Interface Cracks.* Journal of Applied Mechanics—Transactions of the ASME, 1992. **59**(1): p. 61–68.
61. Shih, C.F., *Elastic Plastic Analysis of a Collinear Array of Cracks on a Bimaterial Interface.* Materials Science and Engineering A—Structural Materials Properties Microstructure and Processing, 1989. **107**: p. 145–157.

62. Shih, C.F. and Asaro, R.J., *Elastic Plastic and Asymptotic Fields of Interface Cracks.* International Journal of Fracture, 1990. **42**(2): p. 101–116.
63. Hutchinson, J.W., Mear, M.E., and Rice, J.R., *Crack Paralleling an Interface between Dissimilar Materials.* Journal of Applied Mechanics—Transactions of the ASME, 1987. **54**(4): p. 828–832.
64. Hutchinson, J.W. and Suo, Z., *Mixed-Mode Cracking in Layered Materials.* Advances in Applied Mechanics, Vol 29, 1992. **29**: p. 63–191.
65. Vadakke, V. and Carlsson, L.A., *Experimental investigation of compression failure mechanisms of composite faced foam core sandwich specimens.* Journal of Sandwich Structures & Materials, 2004. **6**(4): p. 327–342.
66. Xu, L.R. and Rosakis, A.J., *Impact failure characteristics in sandwich structures Part I: Basic failure mode selection.* International Journal of Solids and Structures, 2002. **39**(16): p. 4215–4235.
67. Carlsson, L.A., Sendlein, L.S., and Merry, S.L., *Characterization of Face Sheet Core Shear Fracture of Composite Sandwich Beams.* Journal of Composite Materials, 1991. **25**(1): p. 101–116.
68. Zenkert, D. and Vikstrom, M., *Shear Cracks in Foam Core Sandwich Panels — Nondestructive Testing and Damage Assessment.* Journal of Composites Technology & Research, 1992. **14**(2): p. 95–103.
69. Shipsha, A. and Zenkert, D., *Compression-after-impact strength of sandwich panels with core crushing damage.* Applied Composite Materials, 2005. **12**(3–4): p. 149–164.
70. Zenkert, D., Shipsha, A., Bull, P., and Hayman, B., *Damage tolerance assessment of composite sandwich panels with localised damage.* Composites Science and Technology, 2005. **65**(15–16): p. 2597–2611.
71. Shipsha, A., Hallstrom, S., and Zenkert, D., *Failure mechanisms and modelling of impact damage in sandwich beams — A 2D approach: Part I — Experimental investigation.* Journal of Sandwich Structures & Materials, 2003. **5**(1): p. 7–31.
72. Shipsha, A., Hallstrom, S., and Zenkert, D., *Failure mechanisms and modelling of impact damage in sandwich beams — A 2D approach: Part II — Analysis and modelling.* Journal of Sandwich Structures & Materials, 2003. **5**(1): p. 33–51.

73. Li, R.F. and Kardomateas, G.A., *Nonlinear High-Order Core Theory for Sandwich Plates with Orthotropic Phases.* AIAA Journal, 2008. **46**(11): p. 2926–2934.
74. Li, R., Frostig, Y., and Kardomateas, G.A., *Nonlinear high-order response of imperfect sandwich beams with delaminated faces.* AIAA Journal, 2001. **39**(9): p. 1782–1787.
75. Quispitupa, A., Berggreen, C., and Carlsson, L.A., *On the analysis of a mixed mode bending sandwich specimen for debond fracture characterization.* Engineering Fracture Mechanics, 2009. **76**(4): p. 594–613.
76. Kulkarni, N., Mahfuz, H., Jeelani, S., and Carlsson, L.A., *Fatigue crack growth and life prediction of foam core sandwich composites under flexural loading.* Composite Structures, 2003. **59**(4): p. 499–505.
77. Zenkert, D. and Burman, M., *Tension, compression and shear fatigue of a closed cell polymer foam.* Composites Science and Technology, 2009. **69**(6): p. 785–792.
78. Thomsen, O.T., Bozhevolnaya, E., Lyckegaard, A., and Mortensen, F., *Characterisation and assessment of load response, failure and fatigue phenomena in sandwich structures induced by localised effects: A review.* Strain, 2008. **44**(1): p. 85–101.
79. Brocca, M., Bazant, Z.P., and Daniel, I.M., *Microplane model for stiff foams and finite element analysis of sandwich failure by core indentation.* International Journal of Solids and Structures, 2001. **38**(44–45): p. 8111–8132.
80. Deshpande, V.S. and Fleck, N.A., *Multi-axial yield behaviour of polymer foams.* Acta Materialia, 2001. **49**(10): p. 1859–1866.
81. Steeves, C.A. and Fleck, N.A., *Collapse mechanisms of sandwich beams with composite faces and a foam core, loaded in three-point bending. Part 1: analytical models and minimum weight design.* International Journal of Mechanical Sciences, 2004. **46**(4): p. 561–583.
82. DIAB. *Divinycell H Technical Data Sheet*. Available from: http://www.diabgroup.com/americas/u_literature/u_pdf_files/u_ds_pdf/H_DS_US.pdf.
83. Sierakowski, R.L. and Chaturvedi, S.K., *Dynamic loading and characterization of fiber-reinforced composites*. 1997, New York: Wiley. xiii, 252 p.

84. Bruck, H.A., Mcneill, S.R., Sutton, M.A., and Peters, W.H., *Digital Image Correlation Using Newton-Raphson Method of Partial-Differential Correction.* Experimental Mechanics, 1989. **29**(3): p. 261–267.
85. Busse, G., *Imaging with Optically Generated Thermal Waves.* IEEE Transactions on Sonics and Ultrasonics, 1985. **32**(2): p. 355–364.
86. Busse, G., Wu, D., and Karpen, W., *Thermal Wave Imaging with Phase Sensitive Modulated Thermography.* Journal of Applied Physics, 1992. **71**(8): p. 3962–3965.
87. Busse, G., *Optoacoustic Phase-Angle Measurement for Probing a Metal.* Applied Physics Letters, 1979. **35**(10): p. 759–760.
88. Dulieu-Barton, J.M. and Stanley, P., *Development and applications of thermoelastic stress analysis.* Journal of Strain Analysis for Engineering Design, 1998. **33**(2): p. 93–104.
89. Pitarresi, G. and Patterson, E.A., *A review of the general theory of thermoelastic stress analysis.* Journal of Strain Analysis for Engineering Design, 2003. **38**(5): p. 405–417.
90. Lesniak, J.R., Bazile, D. J., B.R., Zickel, M.J.,Cramer, K. E., and Welch, C. S., *Stress Intensity Measurement via Infrared Focal Plane Array*, in *Nontraditional Methods of Sensing Stress, Strain, and Damage in Materials and Structures*, D.A. Stubbs, Editor. 1996, American Society for Testing and Materials: Philadelphia.
91. Dulieu-Barton, J.M., Fulton, M.C., and Stanley, P., *The analysis of thermoelastic isopachic data from crack tip stress fields.* Fatigue & Fracture of Engineering Materials & Structures, 2000. **23**(4): p. 301–313.
92. Paynter, R.J.H. and Dutton, A.G., *The use of a second harmonic correlation to detect damage in composite structures using thermoelastic stress measurements.* Strain, 2003. **39**(2): p. 73–78.
93. Dulieu-Barton, J.M., Emery, T.R., Quinn, S., and Cunningham, P.R., *A temperature correction methodology for quantitative thermoelastic stress analysis and damage assessment.* Measurement Science & Technology, 2006. **17**(6): p. 1627–1637.
94. Dulieu-Barton, J.M. and Quinn, S., *Thermoelastic stress analysis of oblique holes in flat plates.* International Journal of Mechanical Sciences, 1999. **41**(4-5): p. 527–546.

95. Chu, T.C., Ranson, W.F., Sutton, M.A., and Peters, W.H., *Applications of Digital-Image-Correlation Techniques to Experimental Mechanics.* Experimental Mechanics, 1985. **25**(3): p. 232–244.

96. Sutton, M.A., Cheng, M.Q., Peters, W.H., Chao, Y.J., and McNeill, S.R., *Application of an Optimized Digital Correlation Method to Planar Deformation Analysis.* Image and Vision Computing, 1986. **4**(3): p. 143–150.

97. Sutton, M.A., McNeill, S.R., Jang, J.S., and Babai, M., *Effects of Subpixel Image-Restoration on Digital Correlation Error-Estimates.* Optical Engineering, 1988. **27**(10): p. 870–877.

98. Sutton, M.A. and Chao, Y.J., *Measurement of Strains in a Paper Tensile Specimen Using Computer Vision and Digital Image Correlation .1. Data Acquisition and Image-Analysis System.* Tappi Journal, 1988. **71**(3): p. 173–175.

99. Sutton, M.A., *Image correlation for shape, motion and deformation measurements: basic concepts, theory and applications*. 2009, New York: Springer.

100. Maldague, X., *Theory and practice of infrared technology for nondestructive testing*. Wiley series in microwave and optical engineering. 2001, New York;: Wiley. xix, 684 p.

101. FLIR. *SC 6000 Datasheet* Available from: http://www.flir.com/WorkArea/linkit.aspx?LinkIdentifier=id&ItemID=19966.

102. Patterson, E.A., Ji, W., and Wang, Z.F., *On image analysis for birefringence measurements in photoelasticity.* Optics and Lasers in Engineering, 1997. **28**(1): p. 17–36.

103. Siegmann, R., Backman, D., and Patterson, E.A., *A robust approach to demodulating and unwrapping phase-stepped photoelastic data.* Experimental Mechanics, 2005. **45**(3): p. 278–289.

104. Tippur, H.V., Krishnaswamy, S., and Rosakis, A.J., *A Coherent Gradient Sensor for Crack Tip Deformation Measurements — Analysis and Experimental Results.* International Journal of Fracture, 1991. **48**(3): p. 193–204.

105. Rosakis, A., *Two Optical Techniques Sensitive to Gradients of Optical Path Difference: the Method of Caustics and the Coherent Gradient Sensor (CGS).* VCH Publishers, Inc., Experimental Techniques in Fracture (USA), 1993: p. 327–425.

106. Gough, J., *A description of a property of caoutchouc or Indian rubber; with some reflections on the cause of the elasticity of this substance in a letter to Dr. Holme.* Manchester Phil. Mem, 1805. **Second Series**(1): p. 288–295.

107. Weber, W., *Ueber die specifische Wärme fester Körper, insbesondere der Metalle.* Annalen der Physik und Chemie, 1830. **Band XX**: p. 177–213.

108. Thomson, W.L.K., *On the dynamical theory of heat.* Trans. R. Soc. Edin., 1853. **20:**(2610–283).

109. Thomson, W.L.K., *On the thermoelastic and thermomagnetic properties of matter.* Q. J. Math., 1857. **1**: p. 57–77.

110. Thomson, W.L.K., *On the thermoelastic, thermomagnetic and pyro-electric properties of matters.* Phil. Mag., 1878. **5**: p. 4–27.

111. Biot, M.A., *Thermoelasticity and Irreversible Thermodynamics.* Journal of Applied Physics, 1956. **27**(3): p. 240–253.

112. Matweb.com. *Aluminum 2024-T6* 2010; Available from: http://www.matweb.com/search/DataSheet.aspx?MatGUID=ecf8530875cb4ded9675b827f77bfac5.

113. Matweb.com. *Overview of materials for Nylon 6, Cast* 2010; Available from: http://www.matweb.com/search/DataSheet.aspx?MatGUID=8d78f3cfcb6f49d595896ce6ce6a2ef1&ckck=1.

114. Matweb.com. *Overview of materials for Acrylic, Extruded* 2010; Available from: http://www.matweb.com/search/DataSheet.aspx?MatGUID=632572aeef2a4224b5ac8fbd4f1b6f77.

115. Wan, Z.M., Zhang, Y.L., Ma, X.L., King, M.D., Myers, J.S., and Li, X.W., *Vicarious Calibration of the Moderate-Resolution Imaging Spectroradiometer Airborne Simulator Thermal-Infrared Channels.* Applied Optics, 1999. **38**(30): p. 6294–6306.

116. Solutions, C. *Vic-2D 2009*. Available from: http://www.correlatedsolutions.com/index.php/products/vic-2d-2009.

117. Anderson, T.L., *Fracture mechanics : fundamentals and applications*. 3rd ed. 2005, Boca Raton, FL: Taylor & Francis. 621 p.

118. USNavy, *Shock Tests. H.I. (High-Impact) Shipboard Machinery, Equipment, and Systems, Requirements for MIL-S-901D*. 1989.

119. Rosen, A., *Loads and Responses for Planing Craft in Waves*, in *Aeronautical and Vehicle Engineering Division of Naval Systems*. 2004, KTH: Stockholm, Sweden.

120. Soden, P.D., Kaddour, A.S., and Hinton, M.J., *Recommendations for designers and researchers resulting from the world-wide failure exercise.* Composites Science and Technology, 2004. **64**(3–4): p. 589–604.

121. Cytec. *Thornel T300 PAN-Based Fiber Properties*. Available from: http://www.cytec.com/engineered-materials/products/Datasheets/T300%20RevA7-12-06.pdf.

122. Derakane. *DERAKANE 8084 Epoxy Vinyl Ester Resin Properties*. Available from: http://www.derakane.com/derakaneControllerAction.do?method=goToProductDetailPage&actionForwardName=derakane8084&productCode=536004.

123. Soden, P.D., Hinton, M.J., and Kaddour, A.S., *Biaxial test results for strength and deformation of a range of E-glass and carbon fibre reinforced composite laminates: failure exercise benchmark data.* Composites Science and Technology, 2002. **62**(12–13): p. 1489–1514.

124. Stinchcomb, W., *Nondestructive evaluation of damage accumulation processes in composite laminates.* Composites Science and Technology, 1986. **25**(2): p. 103–118.

125. Emery, T.R. and Dulieu-Barton, J.M., *Damage monitoring of composite materials using pulsed phase thermography and thermoelastic stress analysis.* Damage Assessment of Structures VII, 2007. **347**: p. 621–626.

126. UnitedFoam. *Recticulted foam*. Available from: http://steplaw.com/reticulatedfoam.html.

127. Klempner, D., Sendijarevic, V., and Aseeva, R.M., *Handbook of polymeric foams and foam technology*. 2nd ed. 2004, Munich: Hanser Publishers 584 pp.

128. Dulieu-Barton, J.M., Boyenval Langlois, C., Thomsen, O.T., Zhang, S., and Fruehmann, R.K., *Derivation of temperature dependent mechanical properties of polymer foam core materials using optical extensometry.* EPJ Web of Conferences, 2010. **6**: p. 38004.

129. Kidd, T.H., *Mechanical characterization of damage and failure in polymeric foams and glass/epoxy composites*. PhD Dissertation 2006, California Institute of Technology: Pasadena, CA.

130. DIAB. *DIAB Divinycell® H 100 Semi-rigid PVC Foam Core Material* Available from: http://www.matweb.com/search/datasheet.aspx?matguid=0872e8bd246246aaa7e3c5f6edd892d9.